© Copyright by Han Wang 2012
All Rights Reserved

# Advanced Modeling and Applications of Smart Materials and Structures on Passive Vibration Suppression

A Dissertation

Presented to

the Faculty of the Department of Mechanical Engineering

University of Houston

In Partial Fulfillment

of the Requirements for the Degree

Doctor of Philosophy

in

Mechanical Engineering

by

Han Wang

August 2012

**Advanced Modeling and Applications of Smart Materials and Structures on Passive Vibration Suppression**

Han Wang

Approved by:

Chair of the Committee
Dr. Gangbing Song, Professor
Mechanical Engineering

Committee Members:

Dr. Yi-Lung Mo, Professor
Civil Engineering

Dr. Lewis T. Wheeler, Professor
Mechanical Engineering

Dr. Matthew A. Franchek, Professor
Mechanical Engineering

Dr. Karolos M. Grigoriadis, Professor
Mechanical Engineering

Dr. Suresh K. Khator, Associate Dean
Cullen College of Engineering

Dr. Pradeep Sharma, Chair
Mechanical Engineering

## Acknowledgements

This dissertation is the result of my studies and research projects at the University of Houston. Most importantly, I am truly thankful to my advisor, Dr. Gangbing Song, who has been continuously advising and supporting my research with in-depth knowledge. I am extremely grateful to this diligent pioneer, especially in the area of smart materials and structures for providing me with this precious opportunity to work in his research group and providing me with countless valuable suggestions, without which this dissertation would not have been even possible. It is my enormous pleasure and honor to work with him.

I want to acknowledge all my of committee members, Dr. Matthew Franchek, Dr. Karolos Grigoriadis, Dr. Lewis Wheeler and Dr. Yi-lung Mo for giving me tremendous suggestions on my research and this dissertation, which have significantly improved the quality of this work.

I want to thank all of my wonderful colleagues Dr. Haichang Gu, Dr. Claudio Olmi, Dr. Luyu Li, Dr. Peng Li, Dr. Liang Ren, Dr. Bing Xu, Dr. Tiejun Liu, Michael Ho, Christina Chang, Mithun Singla, Devendre Patil, Yue Yu, Bo Cao, Qingzhao Kong, Jiabiao Ruan, Larry Vuong, Quang Do, Michelle Ho, Pole Liu and Jeremy Evans. I have understood that endless research could also delight my life because of them.

Last but not the least, I want to thank my dear parents and friends. I would not have achieved this without their consistent support. Finally, I want to thank you for reading this dissertation.

**Advanced Modeling and Applications of Smart Materials and Structures on Passive Vibration Suppression**

An Abstract

of a

Dissertation

Presented to

the Faculty of the Department of Mechanical Engineering

University of Houston

In Partial Fulfillment

of the Requirements for the Degree

Doctor of Philosophy

in

Mechanical Engineering

by

Han Wang

August 2012

# Abstract

In the past two decades, smart materials and structures have been increasingly used in active and passive structural vibration suppression, since such materials or structures can convert kinetic energy of vibrations into other forms. A useful property in smart materials and structures is their hysteretic behavior, which has an energy dissipating effect during vibration suppression. However, the nonlinearity of the hysteresis poses a challenge for structural modeling. This Ph.D. dissertation focuses on advanced modeling of smart materials and structures and their potential applications on passive structural vibration suppression.

This dissertation develops several advanced modeling approaches including a nonlinear autoregressive exogenous (NARX) model based on a recurrent neural network (RNN) for smart materials with hysteretic behaviors, a phenomenological model for superelastic shape memory alloy (SMA) helical springs, and a mathematical model using quasi-static electromagnetic theories for a prototype passive electromagnetic (EM) damper. In addition to forward modeling approaches to estimate responses, an inverse NARX RNN model is developed for reference control purposes. The implementation of smart materials and structures with their advanced modeling are applied to two types of applications, a base isolation system and a subsea jumper system. Both numerical simulation and experimental results have proven the advanced modeling methods perform accordingly, and the implementations can dramatically reduce structural vibration and improve structure safety.

# Table of Contents

# List of Figures

# List of Tables

# Chapter 1. Introduction

Smart materials or functional materials are certain types of materials which properties can undergo purposeful and reversible changes. These changes can significantly vary the original materials' properties in a controlled manner. In the recent years, many types of smart materials, including piezoelectric materials, shape memory alloys (SMAs), magnetorheological (MR) materials and so on, have been frequently studied and applied. Applications of various types of smart sensors and actuators have been utilizing smart materials due to their special properties. In this dissertation, smart structures are defined as such structures whose properties can be actively controlled or adjusted in the aim of specific functionalities such as vibration suppression. Popular smart structures include MR dampers, electromagnetic (EM) dampers, SMA braces, and systems utilizing them.

This dissertation concentrates on advanced modeling methods and innovative applications of smart materials and structures, especially in the area of passive structural vibration suppression.

## 1.1 Objectives and Motivations

In structural design, passive vibration suppression has been favored to mitigate the impact of earthquakes and wind loads in the past several decades (Soong and Dargush, 1997). Most current energy dissipation systems and devices were built by either transferring energy between different vibration modes, or by converting the kinetic energy into other forms of energy such as thermal energy. Smart materials and structures are excellent candidates for formulating energy dissipation devices, since their special properties can achieve such a conversion of energy. Furthermore, smart

materials and structures normally carry hysteretic behaviors, which can be utilized to dissipate energies and further reduce vibrations. On the other hand, hysteretic behaviors as one type of highly nonlinear behaviors can cause great difficulty in modeling of smart materials and numerical simulations. This dissertation aims at advanced modeling of hysteretic behaviors in smart materials and structures with potential applications especially in the area of structural vibration suppression.

In this dissertation, advanced modeling for smart materials including ultra-thin SMA wires, helical superelastic SMA springs are developed. A mathematical model for prototype EM dampers as an innovative type of smart structure is derived. Applications of smart materials and structures are investigated to passively suppress structural vibration and reduce damages. A two-story experimental base isolation structural model and a numerical subsea jumper model are chosen as exemplary applications of smart materials and structures in passive vibration suppression.

## 1.2 Research Contributions

**The first contribution of this research is an innovative modeling approach based on recurrent neural networks for hysteretic smart materials, such as SMAs, piezoceramics, MR fluids.** We create a new type of recurrent neural network structure and its corresponding training approach. The model after training is validated experimentally by using an ultra-thin SMA wire. Furthermore, the idea of this innovative modeling method is applied to inversed neural network models that, as a feedforward controller without feedback signals, can predict and control the strain or position of the ultra-thin SMA wire.

**The second contribution is an innovative phenomenological modeling of superelastic SMA helical springs. The phenomenological model considers the shape of the hysteresis and calculates the corresponding force based on the relative displacement.** To validate the modeling approach, two superelastic SMA springs were trained in-house and experimentally tested. Furthermore, the trained SMA springs were used in an experimental base isolation structure to function as both energy dissipation and position restoring device.

**The third contribution lies in the advanced modeling of a prototype EM damper.** A mathematical model, which shows the force-velocity relation of the EM damper, is developed based on quasi-static electromagnetic theories. Geometric, magnetic and electric properties determine the damping coefficients of the prototype EM dampers. This advanced modeling has dramatically improved research in this area by reducing the error between numerical and experimental results. Potential applications of the prototype EM dampers include base isolation systems, subsea jumper systems and other structures in need of passive vibration suppression.

**The fourth contribution is the application of the smart materials and structures on base isolation structures.** The superelastic SMA helical springs and the prototype EM damper were implemented in a two-story base isolation building as energy dissipation and passive damping devices. Numerical and experimental data indicate that the structural vibration can be significantly reduced by utilizing the smart materials and structures.

**The fifth contribution is the application of smart materials and structures on subsea jumper systems.** A hybrid EM damper was designed consisting of a

structure similar to the prototype EM damper and four identical superelastic SMA springs. The numerical results indicate that by utilizing the hybrid EM damper, the stress at the bottom of the subsea jumper system as well as the relative displacement in the middle node of the jumper can be dramatically reduced under various earthquakes excitations.

Finally, this research provides a basis for future studies using smart materials and structures for passive vibration suppression. With further modeling and experimentation, the results of this dissertation will find wide application in many other fields of engineering.

## 1.3 Organization

This dissertation is organized into eight chapters. The outline of this dissertation is as follows:

Chapter 1 presents the motivations, objectives and the major contributions of this dissertation.

Chapter 2 presents the literature review of related topics: 1) shape memory alloys, 2) electromagnetic dampers, 3) artificial neural networks, 4) base isolation systems and 5) subsea jumper systems.

Chapter 3 develops an innovative modeling approach based on recurrent neural networks for smart materials and structures with hysteretic behaviors. A new type of network structure and the corresponding advanced training procedure is developed. The proposed modeling approach was tested given an ultra-thin shape memory alloy wire.

Chapter 4 presents a success utilization of the innovative recurrent neural network structure, in the area of active prediction and control. The network structure

was modified to be an inverse model as an off-line feedforward controller. Similarly, the inverse model was applied to actively control the position of the ultra-thin shape memory alloy wire.

Chapter 5 derives an innovative phenomenological modeling approach for superelastic shape memory alloys with a shape of helical spring. Various sets of experiments with a trained-in-house shape memory alloy spring were performed to validate the proposed modeling. To investigate a potential application of superelastic SMA springs, an experimental base isolation system was built and properly modeled. The superelastic SMA springs could dramatically suppress the experimental structural vibration in the base isolation system with disturbances of various earthquakes.

Chapter 6 introduces the design of a prototype electromagnetic damper and develops the corresponding mathematical model based on quasi-static electromagnetic theories. The mathematical model was validated by comparing the theoretical data with the experimental data of a commercial moving magnet motor that can be utilized as a prototype electromagnetic damper. In addition, this chapter presents the potential application of prototype electromagnetic dampers in base isolation systems. Based on a mathematical model of an experimental base-isolated structure setup, a numerical simulation of the structural performance under various earthquakes is given and analyzed for the performance of the electromagnetic damper.

Chapter 7 develops a hybrid electromagnetic damper considering the effective superelastic shape memory alloy spring in structural vibration suppression. Furthermore, a configured prototype hybrid electromagnetic damper was designed and numerically simulated with a subsea jumper system.

Lastly, Chapter 8 presents the conclusions of the research and recommendations for future work.

# Chapter 2. Literature Review

In the past several decades, smart materials and structures have been widely used in many areas and applications. This chapter includes reviews of shape memory alloys as a popular type of smart materials, and reviews of electromagnetic dampers as an avant-garde type of smart structures. Since artificial neural networks and recurrent neural networks are utilized as modeling structures, they are also reviewed. Besides, we cover the literature review of base isolation systems and subsea jumper systems, which are implemented with the technique of smart materials and structures in this dissertation.

## 2.1 Shape Memory Alloys

Shape memory alloys (SMAs), such as NiTi-based alloys, have been used as one of the most promising smart devices in many engineering applications including civil (Torra *et al*., 2007), mechanical (de Araujo *et al*., 2011), biomedical (Kuribayashi *et al*., 2006), aerospace (Chau *et al*., 2006) among others. The shape memory effect and the superelasticity are the two major properties leading to the popularity of SMAs.

### 2.1.1 Shape Memory Effect

The shape memory effect was first observed and recorded in 1932 (Chang and Read, 1951) by finding the reversibility of the transformation in Au-Cd through metallographic observations and resistivity changes. This effect is defined as the capability of deformation to a memorized shape upon application of external stimulus. SMAs have the property of thermally induced shape memory effect, which causes a change in shape due to a change in temperature. The shape memory effect is based on the nonlinear phase transformation between two solid phases: the martensite phase, and the austenite phase. The martensitic transformation yields a thermoelastic martensite

and develops from a high-temperature austenite phase. This property can be utilized to generate force or motion by heating the material. Also, the transformation exhibits hysteretic behaviors in that of phase composition on heating and on cooling does not overlap. For instance, a hysteretic curve of displacement versus voltage by electrical heating the SMA is shown in Figure 2-1 (Song, 2008).

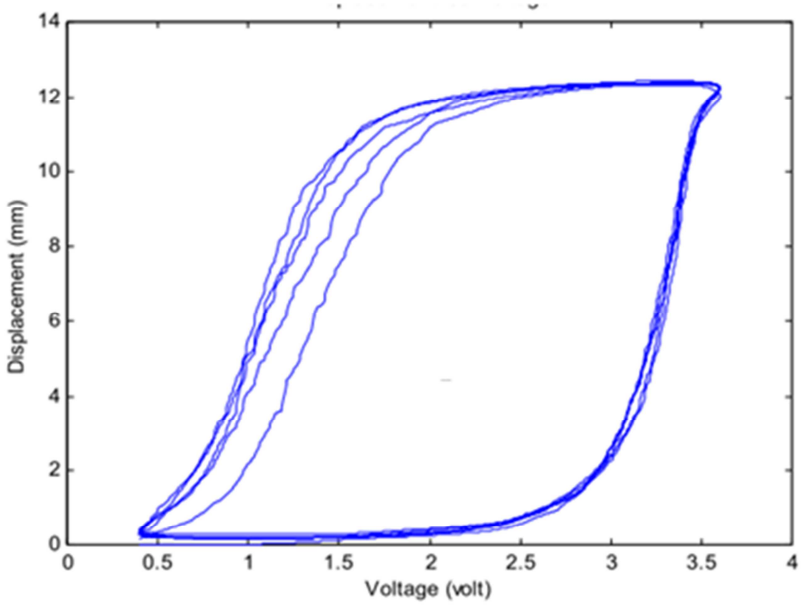


**Figure 2-1: Hysteresis curve example of SMAs (Song 2008).**

SMAs in wire form are widely used in many applications as actuators utilizing the property of the shape memory effect. Comparing to other forms, SMA wires are generally the least expensive and the most readily available forms that can provide relatively linear or straight line movement (Meier and Oelschlaeger, 2004; Shaw, 2002). The dynamic behavior of SMA wires has been of considerable interest. The development of constitutive models for SMA wires has been hampered for many years due to the complexity of the material behavior and the limited experimental basis. Although researchers have studied the constitutive models for the characterization of

the SMA (see, e.g., Tanaka *et al*., 1986; Siredey *et al*., 1999; Potapov and da Silva, 2000), these methods are mostly simplified in order to enable their solvability and applicability. Nevertheless, those constitutive models require plenty of detailed information of the material to achieve an acceptable estimation.

Preisach model based methods have been proposed for hysteresis modeling and tracking control of shape memory alloys (Hughes, 1995). The parameters of Preisach models need to be carefully chosen to achieve an accurate result, and may vary dramatically for different applications. These parameters can be identified by special parameter identification methods in some specified applications (Majima *et al*., 2001). Alternatively, artificial neural networks (ANNs) with special transfer functions can be appropriately trained to estimate the SMAs' hysteretic behaviors (An, 2010). This method could be applicable to limited situations (e.g., at only certain frequency or amplitude) due to the simple structure of feedforward ANNs. Fuzzy algorithms in addition to the neural network are feasible approaches to approximate hysteresis.

Recently, an adaptive neuro-fuzzy inference system has been developed to model an ultra-thin SMA wire (Kilicarslan *et al*., 2011). Normally designing the neuro-fuzzy systems requires excessive experience especially for the fuzzy rule bases and surface. Those limitations can be resolved by introducing new types of neural network structures, such as recurrent neural networks (RNNs).

SMA wires have traditionally been used as "on-off" electromechanical actuators, due to the intrinsic difficulty in accurately controlling the martensite-austenite proportion. This is due to the highly complex and nonlinear rearrangements in the molecular structure of the SMAs. Hysteretic behavior also causes great difficulty of

accurately controlling SMA wires. Controllers without memory or special configurations are insufficient to compensate the hysteresis. Researchers have developed a few advanced control methods by using inverse models of SMAs based on the corresponding mathematical model for the thermo-mechanical behavior covering hysteresis (Mayergoyz, 2003), as it has been done for some other hysteretic materials (Smith, 2005).

However, similar to the constitutive models of SMA wires, accurate inverse models are difficult to obtain, unless adequate information of the material is given. Hence, experimental modeling approaches, such as ANNs, can be utilized to train an inverse hysteresis model for SMA wires (Asua *et al*., 2008). To account for the hysteresis effects, this trained inverse hysteresis model requires proportional-integral with anti-windup control loops, and accurate real-time feedback signals. Thus, a new control method is needed such that it can function as a feedforward controller to micro-position control SMA wires, and the performances can be improved by adding a simple feedback controller. A RNN based inverse model is an achievable solution.

### 2.1.2 Superelasticity

Superelasticity (or pseudoelasticity) is defined as the apparent ability of the material to reversibly sustain up to 8% strain without plastic deformation (Lagoudas, 2008). Similar to the shape memory effect, hysteresis is observed in the stress-strain relationship of superelasticity. Modeling of superelastic behaviors depends on the form or shape of the SMAs. For example, a thermomechanical constitutive model, with strain-rate dependence to predict superelastic behaviors, was developed for SMA wires (Zhu and Zhang, 2007), and a tapered SMA bar has been mathematically modeled to

predict the hysteretic superelastic behavior (Shariat *et al*., 2012). In this dissertation, we focus on modeling the superelastic behaviors of SMAs in the shape of helical springs.

In the past two decades, SMAs in spring shape have been utilized as dampers and actuators in the area of vibration suppression. Oftentimes, applications of SMA springs utilized the property of the shape memory effect. For those applications, SMA springs should be martensitic at room temperature, and act as an actuator while heating up. Researchers have been actively studying the deformation of SMA helical springs based on relationship between stress, strain and temperature since 1990s (Tobushi and Tanaka, 1991). The design and the constitutive model of SMA springs for vibration suppression were introduced and discussed (Liang and Rogers, 1993).

On the other hand, research on the superelastic SMA springs has been increasingly popular in recent years. The mechanical behavior of superelastic SMA helical springs has been investigated to evaluate the response with main concerns being material and geometrical response nonlinearity (Attanasi and Urbano, 2011). In the meantime, the superelasticity of SMA helical springs has been recently numerically analyzed and experimentally tested with a simplified and approximated model (Mirzaeifar *et al*., 2011). Besides the fact that the superelastic behaviors of SMAs in simple geometries (e.g., wire or bar) are considerably difficult to achieve an accurate model, the initial material properties may change due to the complicated thermal and mechanical treatments involved in shape setting the SMAs from wires or bars to helical springs. For this concern, utilizing phenomenological models, by which only the properties of the SMAs after the treatments will be considered, can be better candidates for modeling superelastic behaviors of SMAs in helical spring geometry.

Furthermore, besides the superelasticity, the superelastic SMA springs have the advantages of anti-corrosion, energy dissipation and simple fabrication. Utilizing these advantages in the area of passive structural vibration suppression has not been addressed in the literature.

## 2.2 Electromagnetic Damper

Electromagnetic (EM) devices have been studied and used mainly as either force actuators or generators of electrical energy. The studies of EM devices were limited to applications in regenerative damping systems and for educational purpose (Podrzaj *et al.*, 2005). The term "regenerative damper" refers to devices that can extract energy and provide considerable damping in the system. Regenerative dampers are typically force actuators in controls systems for a dual purpose: 1) they can counteract the disturbances using energy from a power source or storage device, or 2) they can convert the energy of the disturbances into a type of energy which can be utilized or stored.

As part of regenerative damping systems, EM devices have been utilized mostly in vehicular applications (Fodor and Redfield, 1992). Meanwhile some researchers have discovered their possible utilizations in structural vibration suppression (Scruggs, 1999). A structural EM damper has been proposed by Auge (Auge, 2003) to dampen mechanical vibrations in buildings subjected to strong dynamic excitations. In Auge's structural EM damper, permanent magnets were attached to a moving mass, and the movement of the coils attached to the building structure can induce the damping force.

Such a complex EM damping system cannot be easily made, or experimentally validated due to many uncertainties introduced by the huge structure. Passive EM dampers with simple structures should be helpful for vibration suppression in multiple

varieties of applications. Thus, a couple of years later, a prototype passive EM damping device as well as its mathematical model was designed and experimentally tested (Palomera, 2005). However, Palomera's model can be further improved by using equations with more precision. In addition, as a novel type of damper, preliminary studies in implementing passive EM dampers in structural vibration suppression have not been addressed in the literature.

A conceptual hybrid passive EM damper with a hydraulic damping part and an EM damping part was recently designed for vehicle suspension systems (Ebrahimi, 2009). In Ebrahimi's research, the EM part comprises a linear permanent magnet mover with a coil based stator. The movement of the magnet mover pressurizes fluid inside the chamber of the damper, and results in a drag force. However, the hydraulic part of Ebrahimi's hybrid EM damper, with an adequate amount of movement, can cause a temperature change of the fluid in the chamber, and thus influence on the generated damping force. These issues can be resolved by applying an innovative design of an innovative hybrid EM damper combining a prototype EM damper and helical superelastic SMA springs. The EM damping part is less dependent on the change of the operating temperature, and regarding the helical springs, the superelastic SMAs can be manufactured with an elemental composition (e.g. nickel-titanium) that has an operating temperature range suitable for desired applications. A minor change in temperature will not influence on the performance of the damping.

Energy harvesting is another advantage of implementing EM dampers in vibration suppression such that energy from vibrations or kinetic energy can be easily converted to electrical energy which can be stored or used. Researchers have been

studying and modeling the energy harvesting of EM dampers during vibration for several years (Bomarita, 2009). The utilization of the energy harvesting will be a future direction for this research area.

## 2.3 Artificial Neural Networks and Recurrent Neural Networks

The history of artificial neural networks (ANNs) started with the earliest mathematical model of biological neurons in 1943 (McCulloch and Pitts, 1943). In 1959, this model was utilized to develop the first ANN based on a unit called perceptron, which produces an output scaled as either 1 or -1 (Rosenblatt, 1959). Later, researchers found that the perceptron networks are incapable of representing simple functions which were linearly inseparable (Minsky and Papert, 1969), and this finding had dampened the research on ANNs since then. However, this limitation was resolved in the early 1980s, which popularized the study of ANNs. There were at least two reasons for the rapid growth of interest in this field. One reason was the development of both neural network theory and experimental neurobiology, which helped to overcome the limitation of perceptron networks. Another reason was the increasing complexity of technical problems found in various industrial applications insolvable by traditional artificial intelligence (Levine, 2000).

Since a multilayer feedforward ANN with at least one hidden layer has been proved to universally approximate arbitrary bounded non-constant functions (Hornik *et al.*, 1989), it has been successfully applied to many applications such as predicting and modeling in the area of financial (Thawornwong and Enke, 2004), biomedical (Lisboa and Taktak, 2006), engineering (Ye *et al*., 1998), communication (Karras and Zorkadis, 2003), and other disciplines. Some nonlinear behaviors, especially non-mapping

behaviors, such as hysteresis, normally cause great difficulty in building an accurate model. By using ANNs with special structures or algorithms, researchers have developed approaches to model hysteretic behaviors for smart materials, such as modeling hysteretic behaviors of piezoelectric by implementing ANNs built with a Preisach model (Zhang *et al*., 2009). However, the disadvantage of Preisach model is the difficulty in employing physical measurements to construct the hysteresis model directly. Thus, a new modeling approach, which can be applied based on physical measurements regardless the nature of the material, is helpful in practical applications. Modifying the ANN structures is one of the achievable options.

Since multilayer feedforward ANNs have difficulty in storing their past internal states while treating each input as an independent variable, the network structures need modifying such that these drawbacks can be resolved. Hence, various types of recurrent neural networks (RNNs) have been introduced, e.g., the Rumelhart network (Rumelhart *et al*., 1986), the Elman network (Elman, 1988) and the Jordan network (Jordan, 1990), to name a few. RNNs with sufficient number of neurons in the hidden layer have been proven to be universal approximators in state space model form (Schafer and Zimmermann, 2007).

One advantage of RNNs is that they preserve their past activities of neurons, and use these activities as inputs to calculate a current output state. However, the disadvantage of RNNs is that since they are relatively more complicated network structures than ANNs, they will consequently suffer from a significantly heavier calculation burden and longer time cost for training. Regarding this issue, various learning algorithm used for efficiently training RNNs have been proposed in late 1980s

and early 1990s. The backpropagation (BP) learning algorithm for RNNs is among the popular learning algorithms (Pineda, 1989). In the meantime, the real-time recurrent learning algorithm is also presented where the gradient of errors is propagated forward in time instead of backward in time (Williams and Zipser, 1989). In this dissertation, the BP learning algorithm is employed, since it is relatively more balanced in the calculation efficiency and performance.

For modeling of dynamic systems, RNNs can be categorized into two major types: Jordan networks and Elman networks. The Jordan networks have information from the output layer, whereas the Elman networks use feedback from the neurons in the hidden layer. Their network structures make it suitable for representing various types of nonlinear dynamic systems. With the rapid growth of computing ability, RNNs have been recently utilized in various applications. For example, the Jordan network based nonlinear autoregressive exogenous (NARX) neural network model was implemented to capture unknown dynamics of brain activities (Luo and Puthusserypady, 2006). Puscasu has proposed an innovative approach to model nonlinear complex system based on internal RNNs and its modified backpropagation algorithm (Puscasu *et al*., 2009). Regarding the area of hysteresis modeling, Lien introduced a RNN structure with hysteretic transfer functions to model piezoelectric actuators (Lien *et al*., 2010). The tradeoff for Lien's modeling approach is the significantly increased time cost for training. For this concern, modifying RNN structures with special training approach for hysteresis modeling of smart materials is needed.

## 2.4 Base Isolation System

Earthquakes are destructive natural calamities and also huge threats to human lives. A major earthquake can easily destroy a metropolis including housing, traffic, communications, power and water supply systems. Base isolation systems have been regarded as one of the most effective approaches in preventing earthquake related destructions.

The concept of the base isolation systems has a long history starting from 1909 (Kelly, 1986). The base isolation technique has the ability to decouple the base of the structure from the ground during a seismic event. This technique can reduce the seismic energy that effects on the superstructure by partially reflecting the energy and dissipating it at the foundation level (Martelli, 2007). However, this design concept has not received serious attention until early 1980s. From then, researchers have applied this technology to a number of buildings, bridge, nuclear power plants and other structures especially located in frequent-earthquake-areas (Skinner *et al.*, 1993). Despite the suppression of structural vibrations of the superstructure by the base isolation system, base displacements (or base drifts) can most likely be increased. Excessive base movements may lead to further damage to superstructures. Thus, supplemental damping devices are required for safety concerns. Most of damping devices in base isolation systems can be categorized into three types: passive, semi-active and active damping systems.

Various types of passive damping devices, such as friction dampers, have been studied and utilized in base isolation structures (Kareem, 1997). Smart devices have also drawn great attentions due to their ability in energy dissipation (Choi *et al.*, 2008).

For example, researchers have implemented a superelastic SMA bar damper in an elevated highway bridge for seismic energy dissipations (Wilde *et al.*, 2000). An obvious advantage of passive damping devices is that no external power is needed to provide damping forces. However, in the area of base isolation systems, researchers have been debating on passive damping devices which are often uncontrollable and may not be adaptable for earthquakes with various types or strength.

To resolve this adaptability issue, active damping systems have been developed to surpass the limitations of passive damping devices. A number of civil structures have already been practically implemented with active dampers (Housner *et al.*, 1997). However, active damping systems, unlike passive dampers, do require external power sources, typically from the power grids which may fail during destructive seismic motions. Besides, without proper designed control algorithms, active damping systems can inject energy to the superstructure and destabilize it. Thus, semi-active damping devices were introduced to address these concerns.

Research on semi-active damping devices has rapidly drawn great interest in the past two decades, since such devices are easily controllable with fast response (Ramallo *et al.*, 1999). Magneto-rheological (MR) dampers, as one of the most popular semi-active damping devices, have been implemented in base-isolated systems (Kori and Jangid, 2008). Recently, researchers have experimentally implemented advanced semi-active control algorithms such as fuzzy control (Wang *et al.*, 2009) and fuzzy fault tolerant control (Wang and Song, 2011) to MR dampers in base isolation structures.

Due to the complexity of active and semi-active damping systems, the cost for constructions and maintenance are significantly higher than passive damping systems.

Hence, passive damping systems are still good candidates among all for regular structures without strict requirements on minimizing the structural vibrations at all cost. Although research in the area of base isolation systems with passive damping systems has been of great interest, utilizations of EM damper and helical superelastic SMA springs in base isolation systems have not been studied.

## 2.5 Subsea Jumper System

As an important component of offshore oil and gas storage and transportation systems, submarine pipelines are playing a significant role in offshore exploitations. These pipelines are called the lifeline of offshore oil and gas fields. Consistent production in the offshore oil and gas fields depends largely on the safe operation of the submarine pipelines. Vortex induced vibrations (VIV) and fluid structure interaction (FSI) of the free-span submarine pipelines can occur when pipelines are exposed to ocean currents, due to the pipelines' structural style. Thus, supplemental systems are needed to secure the safety of daily operations by minimizing the structural damage from the above effects. Subsea jumper systems are among these important systems.

Subsea jumpers are typically used as an interface between two substantial subsea structures (e.g., risers or flow-lines), and are required to accommodate significant static and dynamic loads. Based on various locations of installation or customer requirements, subsea jumper systems can vary in size and shape, but mostly share a similar basic geometry (Yook, 2008). Figure 2-2 shows a typical M shape jumper, and Figure 2-3 shows a typical subsea jumper installation in offshore oil industry. A typical jumper will have 6 bends and an unsupported pipe with length from fifty to several hundred feet.

**Figure 2-2: Typical Jumper Geometry (Carruth and Cerkovnik, 2007).**

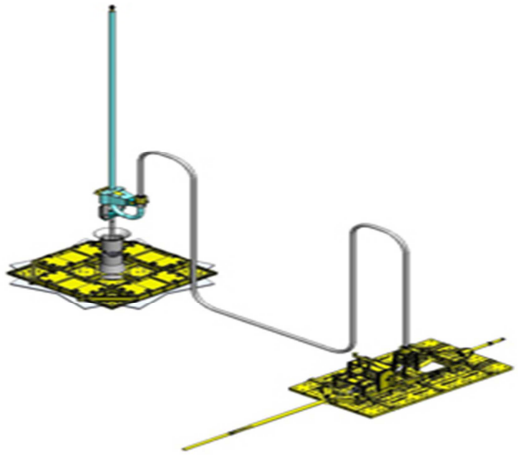

**Figure 2-3: Typical subsea jumper system installation between a riser and a manifold (Patil, 2010).**

The geometry of subsea jumpers, along with the unsupported middle section, results in subsea jumpers with low natural frequencies and low structural damping, and makes the structure susceptible to vortex induced vibration (VIV) in areas of significant current, leading to excessive vibrations (Carruth and Cerkovnik, 2007). These excessive vibrations can cause machinery downtime, oil leaks, fatigue failures or even explosions on offshore platforms. In addition, recurrent operational start-ups and shutdowns in the oil extraction procedure propagate internal shock waves in subsea jumpers, resulting in finite and irreversible longitudinal extension of the middle section over time. This longitudinal extension, accompanied by pipe buckling, relocates the system from its

initial location, which is known as a ratcheting effect (Olunloyo *et al*., 2007). Although the design and the working situations vary for subsea jumpers, VIV can still trigger fatigue and catastrophic fracture on all types of subsea jumpers. Thus, a passive damping system can be helpful to improve the structural safety by dramatically reducing the structural vibration.

# Chapter 3. NARX Recurrent Neural Network for Hysteresis Modeling of Smart Materials

As discussed in the literature review, a modified recurrent neural network (RNN) model with special training method can be helpful to develop a hysteresis model of smart materials. In this chapter, an innovative nonlinear autoregressive exogenous (NARX) model based recurrent neural network (RNN) structure (Jordan-Elman NARX networks) is developed for hysteresis modeling of smart materials, and compared with two existing NARX RNN models: series-parallel mode Jordan NARX networks and parallel mode Jordan NARX networks. The nonlinear autoregressive exogenous model is a commonly used discrete nonlinear system that employs past inputs and outputs to predict a current output. This nature can be utilized to model hysteretic behaviors, since different hysteresis curves with same inputs distinct in past output values or output trajectories that can be applied to identify hysteresis. An ultra-thin SMA wire experimental setup is used to show the effectiveness of the modeling approaches. The experimental results demonstrate that this proposed NARX RNN model can be implemented to model hysteretic behaviors of smart materials.

## 3.1 Series-Parallel Mode Jordan NARX Network (Jordan-SP)

The Nonlinear Autoregressive model with Exogenous inputs (NARX) is a commonly used discrete nonlinear system that can be mathematically represented as

$$y(k) = f\{u(k-1), u(k-2), \ldots, u(k-l), y(k-1), y(k-2), \ldots, y(k-m)\}, \quad \textbf{(Eqn. 3-1)}$$

where $u(k) \in \mathbb{R}$ and $y(k) \in \mathbb{R}$ denote the inputs and the outputs of the NARX model at the discrete time step $k$, respectively. The input memory and the output memory are

$l \geq 0$ and $m \geq 0$ in the NARX model. The unknown function $f(\cdot)$ is generally nonlinear and can be approximated, for instance, by a regular multilayer feedforward network. The resulting model architecture is called a NARX network or Jordan NARX network. A powerful class of dynamical models has been shown to be computationally equivalent to Turing machines (Siegelmann *et al*., 1997). Two modes are introduced that concerns training of the Jordan NARX network, the series-parallel mode and the parallel mode, due to its complex structure.

The network structure of the series-parallel mode Jordan NARX network (Jordan-SP) is presented. In Figure 3-1, $v_1, v_2, \ldots, v_n$ are the neurons in the hidden layer, $W^{(i)}$ is the weight matrix from the input layer to the hidden layer, and $W^{(o)}$ is the weight vector from the hidden layer to the output layer.

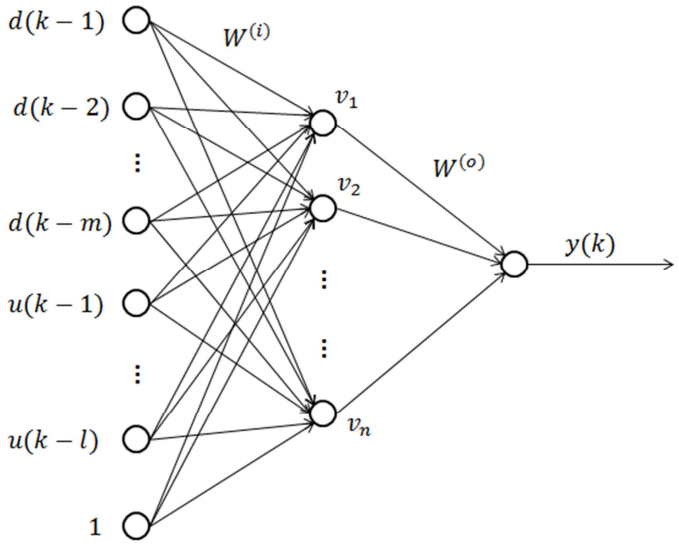


**Figure 3-1: Network structure of series-parallel mode Jordan NARX network.**

The structure is a regular feedforward neural network (FNN) structure, in which the output's regressor is formed only by the actual data of the system's output:

$$\hat{y}(k) = f\{u(k-1), u(k-2), \ldots u(k-l), d(k-1), d(k-2), \ldots d(k-m)\}, \quad \textbf{(Eqn. 3-2)}$$

where $d(k)$ is the desired or actual output data, and $\hat{y}(k)$ is the network's estimated output at the time step $k$. The state of the $p-th$ neuron and its output are defined as:

$$x_p(k) = \sum_{q=1}^{l+m+1} W_{pq}^{(i)} u_q(k), \quad \textbf{(Eqn. 3-3)}$$

$$v_p(k) = f(x_p(k)), \quad \textbf{(Eqn. 3-4)}$$

where the subscripts stand for the index of the element in a vector or a matrix, $W_{pq}^{(i)}$ is the weight connecting the $q-th$ input and the $p-th$ neuron in the hidden layer. Then the output of the network is

$$y(k) = \sum_{p=1}^{n} W_p^{(o)} v_p(k). \quad \textbf{(Eqn. 3-5)}$$

In this chapter, the hyperbolic tangent sigmoid function as shown in (Eqn. 3-6) is applied for the hidden layer, and the linear function is applied for the output layer.

$$f(x) = \frac{2}{1+e^{-2x}} - 1. \quad \textbf{(Eqn. 3-6)}$$

Since the motivation is to let the neural network model track the desired outputs, the cost function should be minimized between the desired outputs and the network's estimated output, which the mean square error (MSE) method is utilized in this chapter. Thus, the cost function for $N$ steps is

$$J = \frac{1}{N} \sum_{k=1}^{N} (\hat{y}(k) - d(k))^2, \quad \textbf{(Eqn. 3-7)}$$

which is a function of $W^{(i)}$ and $W^{(o)}$.

In the training process, by using the Levenberg-Marquardt backpropagation algorithm (Levenberg, 1944; Marquardt, 1963), error functions in each time step can be calculated parallelly in one epoch as a regular FNN. Normally, a accurate training result

is fast to achieve based on this network. However, since this type of networks is generally only one-step-forward-predictor, it cannot be utilized in pure numerial simulations or as a reference model, which involve in long term time prediction. Manually feedback the output signal to the regressor without additional training may accumulate errors in every single steps, and finally cause instability. To improve this shortcoming, the parallel mode Jordan NARX network is built.

## 3.2 Parallel Mode Jordan NARX Network (Jordan-P)

The parallel mode Jordan NARX network (Jordan-P), as shown in Figure 3-2, is a modified network based on the Jordan-SP network by feedback the estimated memory outputs to the input regressor. The network is a type of recurrent neural network, in which the output can be calculated as:

$$\hat{y}(k) = f\{u(k-1), u(k-2), \ldots u(k-l), \hat{y}(k-1), \hat{y}(k-2), \ldots \hat{y}(k-m)\}, \quad \textbf{(Eqn. 3-8)}$$

where $\hat{y}(k)$ is the estimated output of the network at time step $k$.

In each training epoch, the network need to estimate the output in every single time step subsequently, and after all time steps, the cost functions, as mentioned in (Eqn. 3-7), can be calculated and summarized. The training time usually is considerably longer. With a proper training, this type of network can estimate long term time response (multiple steps), or behave as a reference model.

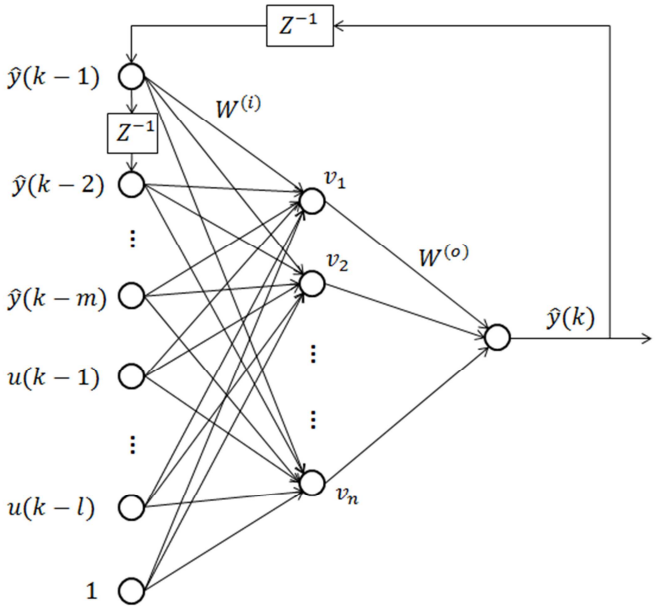


**Figure 3-2: Network structure of parallel mode Jordan NARX network.**

In this chapter, the training approach for the Jordan-P network model is presented as follows:

1) Define the number of neurons $n$ in the hidden layer, the maximum memory order $l$ of the input and the maximum memory order $m$ of the output.
2) Build a FNN (pre-Jordan-SP) with transfer functions of hyperbolic tangent sigmoid function in the hidden layer and of linear function in the output layer. Connect only the tapped delay line (TDL) of the inputs $u(k-1), u(k-2), \ldots, u(k-l)$ to the input layer.
3) Initialize the weights of the pre-Jordan-SP network, and train it by minimizing the cost function in (Eqn. 3-7). Stop the training if a small value of MSE is achieved. If a desired result cannot be found in this step, go back to step 1, and increase the value of $n$, $l$ and $m$.

4) Modify the pre-Jordan-SP network to connect the TDL of the desired outputs $d(k-1), d(k-2), \ldots, d(k-m)$ to the input layer. Initialize the newly introduced input-to-layer weights with the corresponding trained pre-Jordan-SP network in step 3, and then train the Jordan-SP network in consideration of the cost function by using the same training algorithm in step 3. Normally, an improved performance result to step 3 should be found, or return to step 1 and increase the value of $n$, $l$ and $m$ without a desired result.

5) Modify the Jordan-SP network to the Jordan-P network by feedback the estimated output to the input regressor replacing $d(k-1), d(k-2), \ldots, d(k-m)$. Train the Jordan-P network to the desired accuracy, otherwise return to step 1 to increase the value of $n$, $l$ and $m$. It is expected that the local minimum problem might be solved.

The advantage of this proposed training approach includes that (1) the estimated outputs will be predicted based on the memory inputs with more importance than the memory outputs, (2) the training time can be dramatically reduced, because it is much faster to achieve a high accuracy FNN, and (3) fast and concrete convergence is more likely to be observed since the initial values come from a high accurate FNN.

## 3.3 Jordan-Elman NARX Network (Jordan-Elman)

In addition to the Jordan-P network, the Jordan-Elman NARX network (Jordan-Elman) includes feedbacks from its recurrent hidden layer to its input layer, as shown in Figure 3-3. Since the feedbacks can store useful state information about data points far in the past, the Jordan-Elman network can improve the Jordan-P network dramatically.

The output of the Jordan-Elman network is calculated as:

$$\hat{y}(k) = f\{u(k-1), u(k-2), \ldots, u(k-l), \hat{y}(k-1), \hat{y}(k-2), \ldots, \hat{y}(k-m), v_1(k-1), v_2(k-1), \ldots, v_n(k-1)\} \quad \textbf{(Eqn. 3-9)}$$

where $v_p(k)$ are the output of the $p-th$ neuron in the hidden layer at time step $k$.

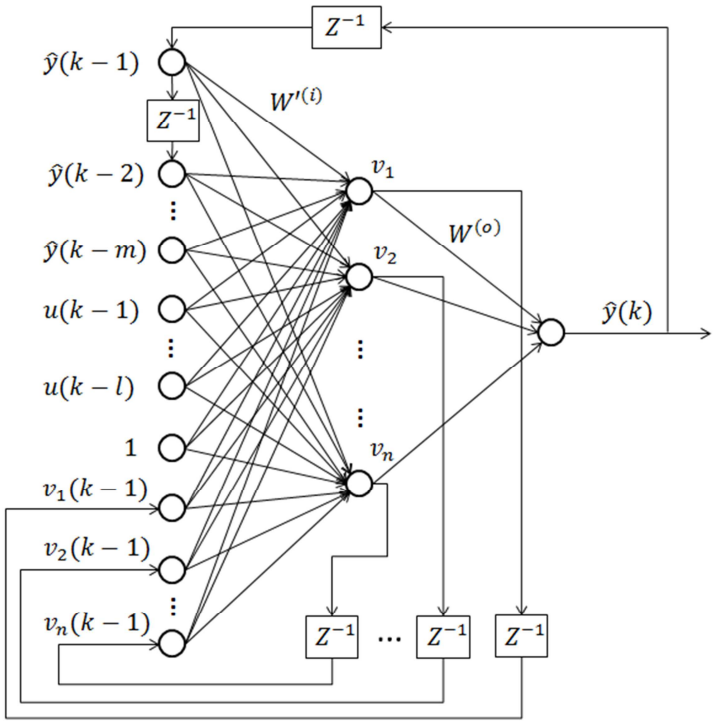


**Figure 3-3: Network structure of Jordan-Elman NARX network.**

Since the Jordan-Elman network not only has to make the prediction, but has to figure out what information is necessary to keep about past data points in order to make a prediction, more neurons are preferred in the hidden layer. Furthermore, the internal state produced by the hidden layer is largely dependent on its initial weights. Therefore, without a special training the Jordan-Elman network is difficult to converge to a good result with an accurate approximation. Thus, the training approach, in addition to the training method for Jordan-P network, is presented as follows:

6) Based on the trained network in step 5, modify the Jordan-P network to connect the hidden layer to the input layer. Simulate this untrained Jordan-Elman

network using the same data, proceed to step 7 if the same performance (MSE) with Jordan-P network is achieved.

7) Initialize the weights connecting between the recurrent hidden layer inputs and the hidden layer within a relatively limited range $\varepsilon$ such that

$$\left|W_{pq}\right| \le \varepsilon,\ p = l+m+2, l+m+3, \ldots, l+m+n+1, q = 1, 2, \ldots, n. \quad \textbf{(Eqn. 3-10)}$$

A purely random initialization may result in the instability of the training. Decrease $\varepsilon$ if the training is divergent. Normally, with a proper value of $\varepsilon$, a reduced MSE than step 5 should be expected in this step. Return to step 1 if no desired result is achieved.

In the following chapter, the above modeling approach will be applied to estimate and predict the nonlinear behavior of the SMA wire. Also, the modeling results of the Jordan-P network and the Jordan-Elman network will be compared and discussed in the Experimental Results chapter.

## 3.4 Experimental Setup of a Ultra-Thin SMA Wire

In this chapter, as shown in Figure 3-4, a Nitinol SMA wire with a diameter of 0.001 inch was used as a micro-positioning actuator. An electric current was applied through the wire to heat, and thus induce the phase transition and the consequent contraction/displacement. When the wire was not activated and heated, the material cooled down to the ambient temperature, and the wire stretched again, provided that a sufficient tensile strain was applied. A bias spring was connected to the top the SMA wire to apply restore force, and a disc was attached the spring as a moving platform. A laser displacement sensor was mounted 40 mm over the platform (disc) to measure the

displacement of the platform (disc). To avoid damage to the SMA wire, he voltage input was limited from 0 volt to 16 volts.

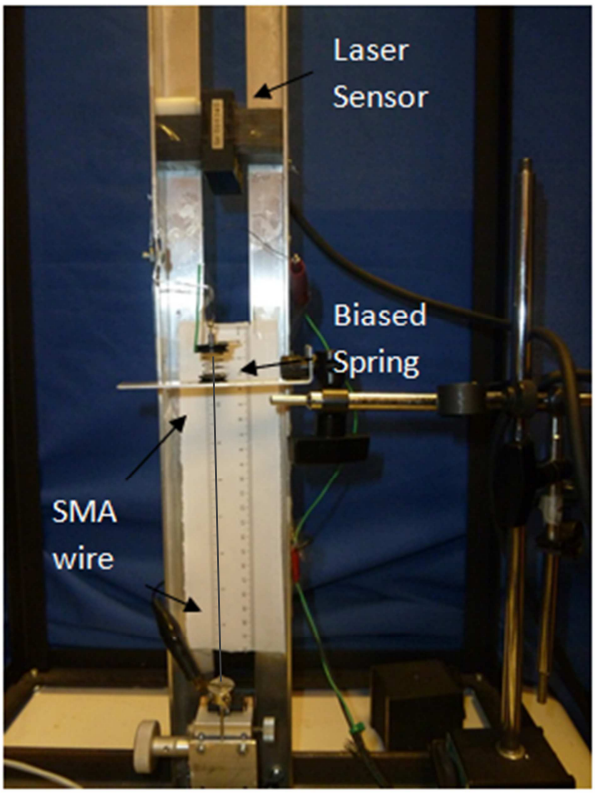


**Figure 3-4: Picture of experimental setup of the 0.001 inch SMA wire.**

The diagram of the experimental system is shown in Figure 3-5. A dSPACE 1104 data acquisition board was used to collect the displacement signal from the laser sensor via an A/D converter, and provide programmable electric current to the power amplifier via a D/A converter, and then to the SMA wire. To send input and monitor the real-time displacement, the software called Controldesk was implemented on the computer connecting to the dSPACE board.

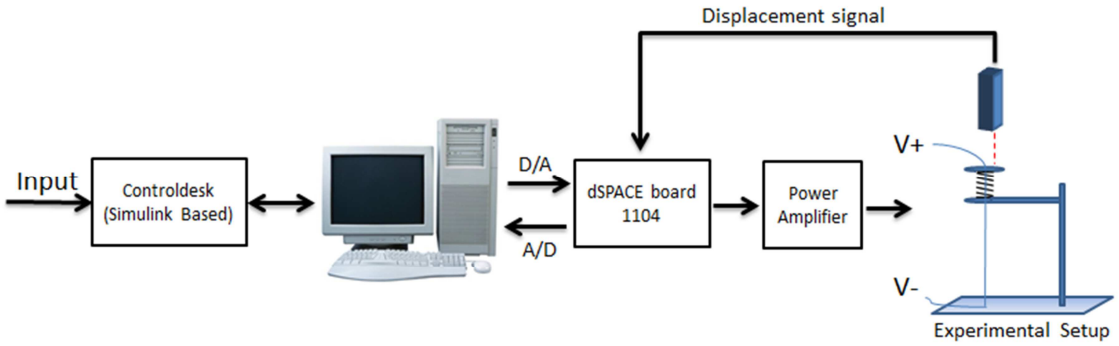


**Figure 3-5: Diagram of the SMA wire experiment system.**

## 3.5 Experimental Results

In this chapter, both Jordan-P network and Jordan-Elman network were trained based on the training approach in 3.2 and 3.3. Both networks were utilized to estimate displacement of the SMA wire based on experimental inputs and the estimated feedback from the hidden layer and the output layer.

In order to justify the improvement of the Jordan-Elman network, both networks have 20 neurons in the hidden layer ( $n = 20$ ), $l = 3$ as the input memory order, $m = 3$ for the output memory order. The Levenberg-Marquardt backpropagation method was applied as the training function, and mean square errors were used to determine and compare the modeling performance. The experimental data of a chirp signal voltage input with a frequency from 0.01 Hz to 1 Hz and its corresponding displacement output was utilized to train both networks. For the Jordan-Elman network, $\varepsilon$ was set at 0.01. Both networks were trained offline and simulated by using MATLAB/Simulink. After the complete training procedure, a Jordan-P network was achieved with an MSE of $11.9\times10^{-4}$ comparing to a Jordan-Elman network with an MSE of $5.83\times10^{-4}$. Figure 3-6 shows the time response comparison between the Jordan-P network and the Jordan-Elman network for the chirp signal used for training, and Figure 3-7 shows the MSE

comparison. As shown in Figure 3-6 and Figure 3-7, for the training data, both networks can successfully estimate and track the experimental data, and the Jordan-P network has a relatively larger MSE than the Jordan-Elman network.

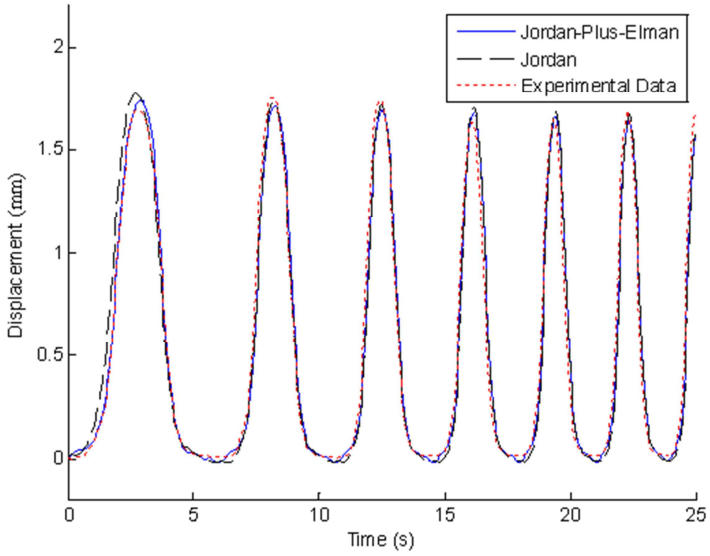


**Figure 3-6: Time response comparison between Jordan-P network and Jordan-Elman network for a chirp signal.**

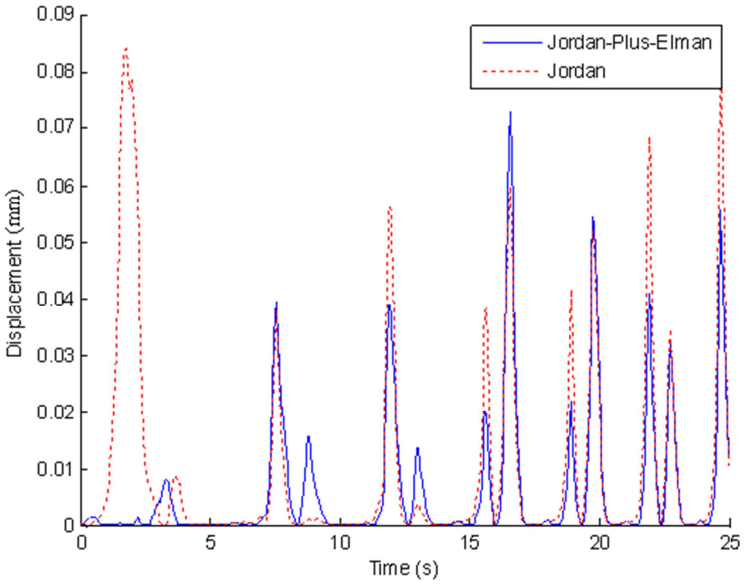


**Figure 3-7: MSE comparison between Jordan-P network and Jordan-Elman network for a chirp signal.**

Furthermore, due to the advanced structure of the Jordan-Elman network, a better generalization is expected. Thus, the time response and the MSE comparison between the Jordan network and the Jordan-Elman network for a sine wave input with a frequency of 0.1 Hz and amplitude of 14 volts is shown in Figure 3-8 (zoomed in) and Figure 3-9, respectively. Clearly from the figure, the Jordan-Elman network has a much better performance in experimental data other than the training data. The MSEs are calculated as 0.0032 for the Jordan-P network and 0.00018 for the Jordan-Elman network. Therefore, the Jordan-Elman network should be used for modeling the SMA wire.

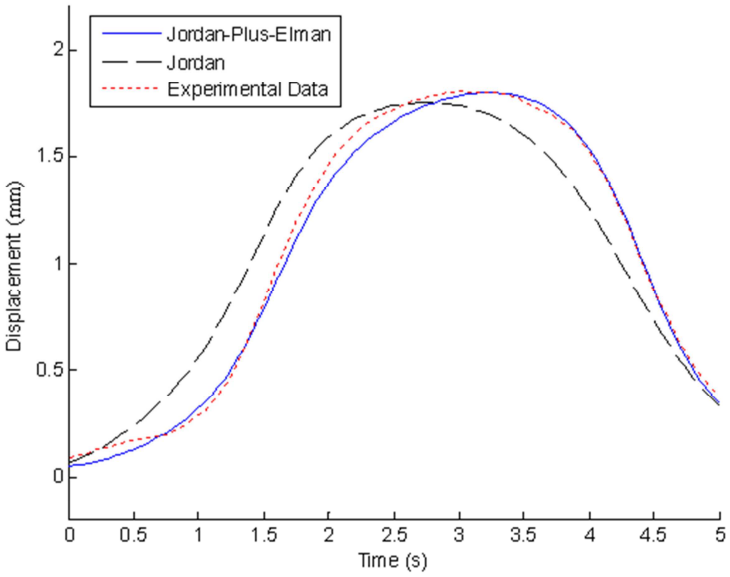


**Figure 3-8: Time response comparison between Jordan-P network and Jordan-Elman network for a 0.1 Hz sinewave (zoom in picture).**

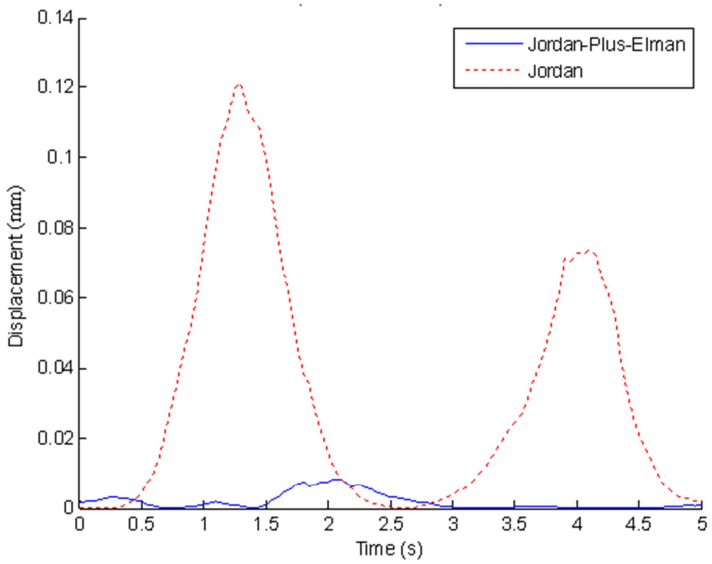


**Figure 3-9: MSE comparison between Jordan-P network and Jordan-Elman network for a 0.1 Hz sinewave (zoom in picture).**

As a major goal of modeling the SMA wire is to identify and estimate its nonlinear hysteretic behavior, Figure 3-10 and Figure 3-11 present the comparison of major loops with inputs of 14 volts 0.1 Hz and 0.5 Hz sine waves between the estimated hysteresis behavior by using the Jordan-Elman network and the experimental hysteresis. Figure 3-12 and Figure 3-13 show the result for a minor loop with inputs of 12 volt 0.1 Hz and 0.5 Hz sine waves. As shown in the figures, both major loops and minor loops have been successfully predicted and estimated with limited errors.

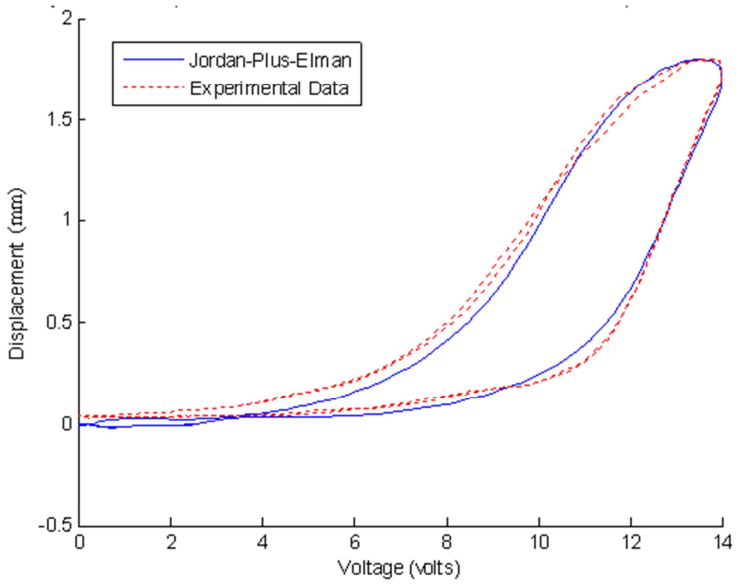


**Figure 3-10: Major loop hysteresis comparison between Jordan-Elman network and experimental data (14 volts 0.1 Hz sinewave).**

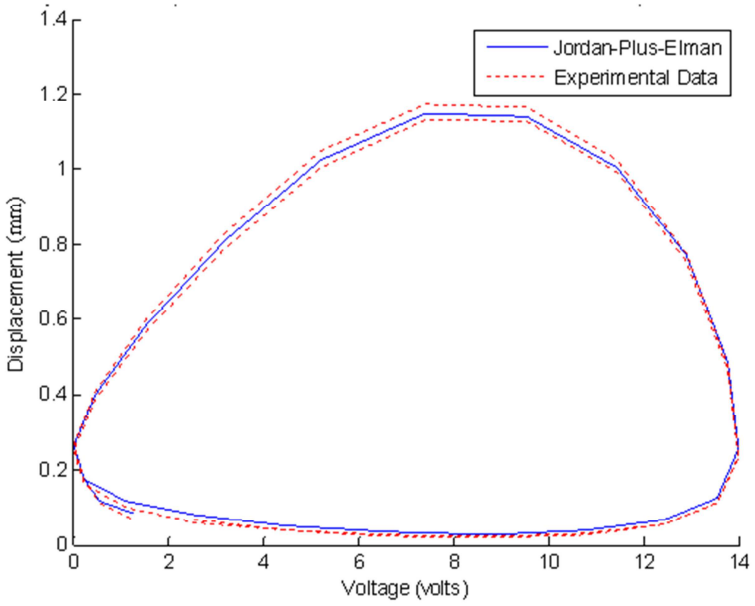


**Figure 3-11: Major loop hysteresis comparison between Jordan-Elman network and experimental data (14 volts 0.5 Hz sinewave).**

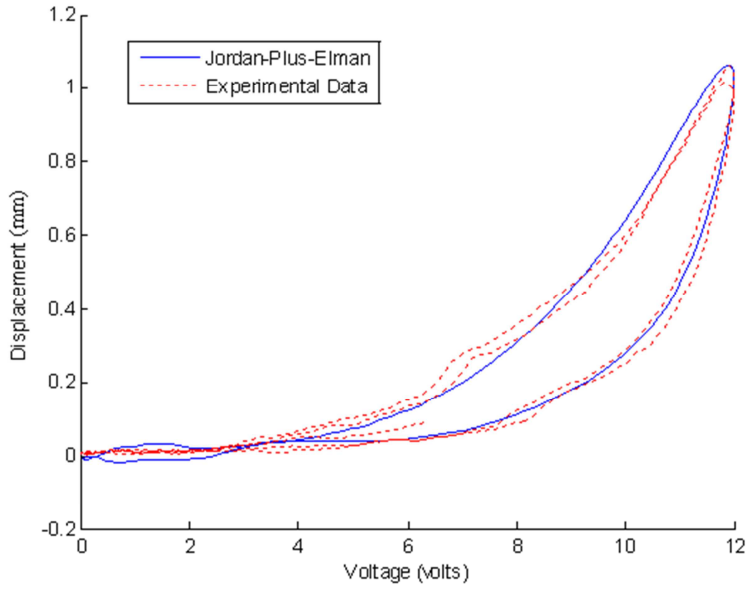


**Figure 3-12: Minor loop hysteresis comparison between Jordan-Elman network and experimental data (12 volts 0.1 Hz sine wave).**

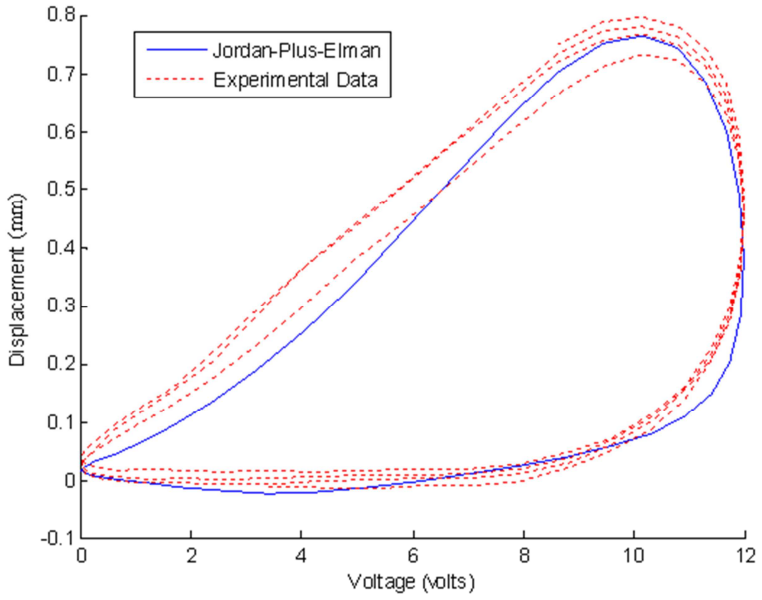


**Figure 3-13: Minor loop hysteresis comparison between Jordan-Elman network and experimental data (12 volts 0.5 Hz sine wave).**

For both major loops and minor loops, although the voltage inputs were pure periodic sine waves, it is obvious that the experimental data in each cycle varied in a considerably small range. Because the good performance of the trained Jordan-Elman network in generalization, the estimated output can successfully track the experimental data in all cycles with limited errors. As the excellent results shown above, a model reference controller can be developed based on a trained Jordan-Elman network.

The experimental results of the hysteresis modeling based on the Jordan-Elman network are summarized in Table 3-1. From the table, it is clear that the trained Jordan-Elman network model can estimate the hysteretic behavior of the ultra-thin SMA wire for various frequencies and amplitudes with remarkably limited errors.

**Table 3-1: Summary of experimental results to Jordan-Elman network (abs.: absolute)**

| Experiment | Figure | Mean Abs. Error (mm) | Max Abs. Error (mm) |
|---|---|---|---|
| 0.1 Hz 14 volts | Figure 3-9 | 0.0715 mm | 0.0424 mm |
| 0.5 Hz 14volts | Figure 3-10 | 0.0267 mm | 0.0103 mm |
| 0.1 Hz 12 volts | Figure 3-11 | 0.0823 mm | 0.0516 mm |
| 0.5 Hz 12 volts | Figure 3-12 | 0.1059 mm | 0.0741 mm |

## 3.6 Summary

In this chapter, an ultra-thin SMA wire with hysteretic nonlinearity was modeled by using NARX recurrent neural network methods. A training approach for the Jordan-P network was proposed. In addition, an innovative Jordan-Elman network with its training procedure was presented and compared to the Jordan-P network for various experimental data. Both networks have been properly trained based on an experimental chirp signal input and its corresponding output. The comparison results have shown that the trained Jordan-Elman network has less mean square error and better generalization than the trained Jordan-P network. Most importantly, the Jordan-Elman network can successfully identify and estimate the hysteretic behavior of the SMA wire for major and minor loops. This contribution will result in an advanced position controlling SMA wires or similar experimental devices by a reference controller or similar control algorithms based on a reference model with an example in the following chapter.

# Chapter 4. Inverse NARX Recurrent Neural Network Model for Controlling Hysteresis

In this chapter, an innovative inverse NARX recurrent neural network is developed to control the response of smart materials as a feedforward controller. The training of the proposed inverse model follows the special training method for RNN networks as shown in Chapter 3. With a proper modeling and training, this inverse model method should be able to predict a future input based on past inputs in order to follow a reference output with limited errors. The aforementioned ultra-thin SMA wire experimental setup is utilized to test the effectiveness of the inverse model method. Furthermore, to improve the control performance in the experiments, a hybrid control scheme is designed by adding a simple feedback controller to the inverse model.

## 4.1 Inverse NARX Jordan-Elman Network Model

Compared with the inverse hysteresis model based on ANNs (Asua *et al*., 2008), we seek an inverse hysteresis model based on RNN structure that shall be sufficient to compensate the hysteretic behaviors without requiring adequate real-time feedback signals. Thus, an innovative Jordan-Elman RNN is developed in this chapter. Besides, if real-time feedback is achievable, a simple feedback controller added to the inverse Jordan-Elman network model could further improve the controlling performance.

The Jordan-Elman inverse NARX network structure is shown in Figure 4-1. As shown in the figure, the output $\hat{u}$ of the inverse network is the predicted input to the control object to follow a reference output. This network structure is similar to the forward Jordan-Elman NARX network except the inverse model considers the tapped delay line (TDL) of the desired outputs (or the reference outputs) and the past

predictions. Also, the inverse network takes all the output from the hidden layers as additional inputs. Thus,

$$\hat{y}(k) = f\{d(k), d(k-1), \ldots, d(k-l), u(k-l), \hat{u}(k-1), \hat{u}(k-2), \ldots, \hat{u}(k-m), v_1(k-1), v_2(k-1), \ldots, v_n(k-1)\} \quad \text{, (Eqn. 4-1)}$$

where $d(k)$ is the desired output at the time step $k$, $\hat{u}(k)$ is the predicted input to the control object, and $v_p(k)$ are the output of the $p-th$ neuron in the hidden layer.

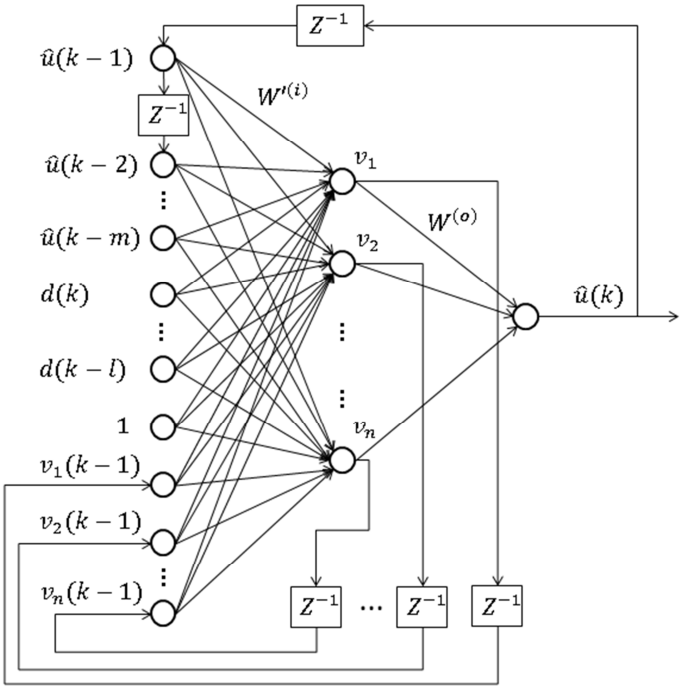


**Figure 4-1: Network structure of inverse NARX Jordan-Elman network.**

Since this inverse network will be utilized as a feedforward, after a proper training, it is expected to learn the dynamics of the control object as well as an effective prediction of inputs given the reference outputs for various frequencies. Thus, the selection of experimental data for network training is critical to achieve a convergent inverse model with limited errors. The training procedure used in this chapter is the same procedure for Jordan-Elman NARX network as mentioned in Chapter 5. The

initialization process of training the inverse NARX Jordan-Elman network should be limited within a relatively smaller range than the regular NARX Jordan-Elman network to avoid divergence. This proposed network structure may need modifications in applications with significant time delays. Future reference inputs can be included in the input layer.

In the following sections, the above approach to inverse modeling will be applied to the displacement tracking control of the ultra-thin SMA wire. Also, a feedback controller will be added to the inverse model to improve the control performance.

## 4.2 Tracking Control of Ultra-thin SMA Wire using Inverse NARX Jordan-Elman Model

The experimental setup as mentioned in 3.4 is utilized to demonstrate the effectiveness of the inverse NARX Jordan-Elman network model to smart materials and structures. Based on a reference input, the proposed inverse model is used to predict and track the position of the ultra-thin SMA wire as a feedforward controller. In this chapter, we only investigate the time response to inputs within a low frequency range including sinusoid waves and chirp signals.

In this section, the input memory $m$ and the output memory $l$ are chosen at $l = m = 4$ with a time step of 0.1 second. The amount of neurons in the hidden layer is chosen as $n = 20$. The experimental data used to train the inverse NARX Jordan-Elman network is shown in Figure 4-2 and Figure 4-3. The input for training, as shown in Figure 4-2, is the displacement of the ultra-thin SMA wire under the voltage with a crisp signal from 0.001 Hz to 0.5 Hz that is also the target output as shown in Figure 4-3.

Note that the input for training is not purely sinusoid waves, thus, in order to track a sinusoid wave at various frequencies, the inverse NARX Jordan-Elman network is expected to learn the dynamic of the feedforward control strategy.

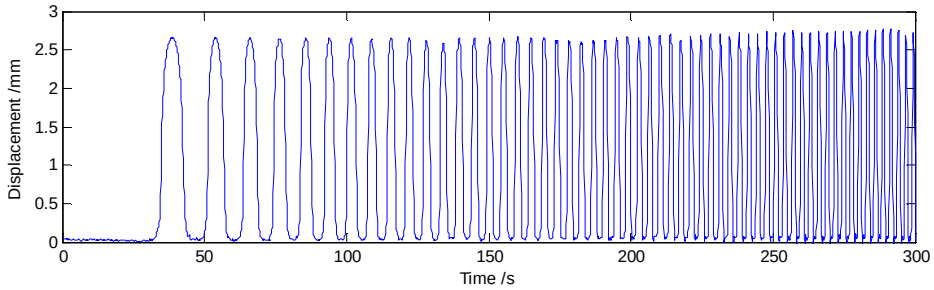


**Figure 4-2: Experimental input for training inverse NARX Jordan-Elman network.**

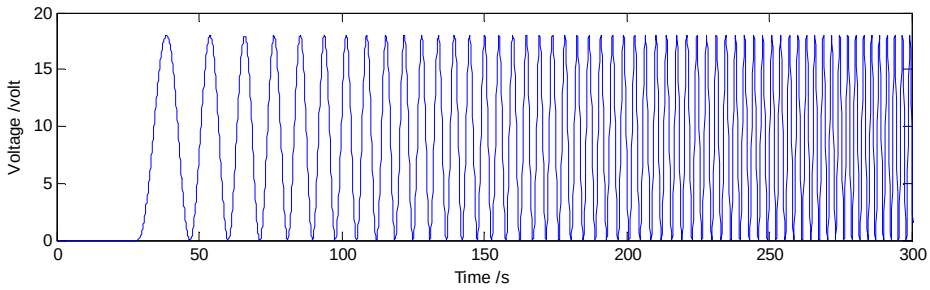


**Figure 4-3: Experimental target output for training inverse NARX Jordan-Elman network.**

In the numerical simulation, the forward NARX Jordan-Elman network model is implemented to simulate the time response of the ultra-thin SMA wire.

### 4.2.1 Numerical Results

As discussed in Chapter 3, since the forward NARX Jordan-Elman network can successfully estimate the time response of the ultra-thin SMA wire with hysteresis for various frequencies, it is used in this numerical simulation. Note that, in this subsection,

only the inverse NARX Jordan-Elman network model is applied as a feedforward controller and no feedback control algorithm will be considered.

Figure 4-4 through Figure 4-7 show that, with the inverse NARX Jordan-Elman network model as the feedforward controller, the ultra-thin SMA wire are tracking sinusoid waves at various frequencies of 0.05 Hz, 0.1 Hz, 0.3 Hz and 0.5 Hz, respectively in numerical simulation. From the numerical results, it is shown that the displacement of the ultra-thin SMA wire controlling by the trained inverse model can properly track the reference inputs at all the frequencies presented with considerably small error.

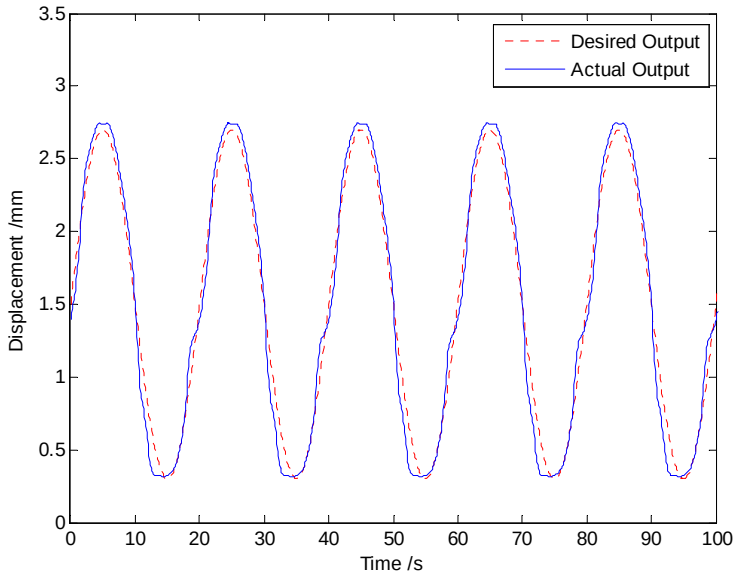


**Figure 4-4: Numerical simulation of inverse NARX Jordan-Elman network model with 0.05 Hz sine wave.**

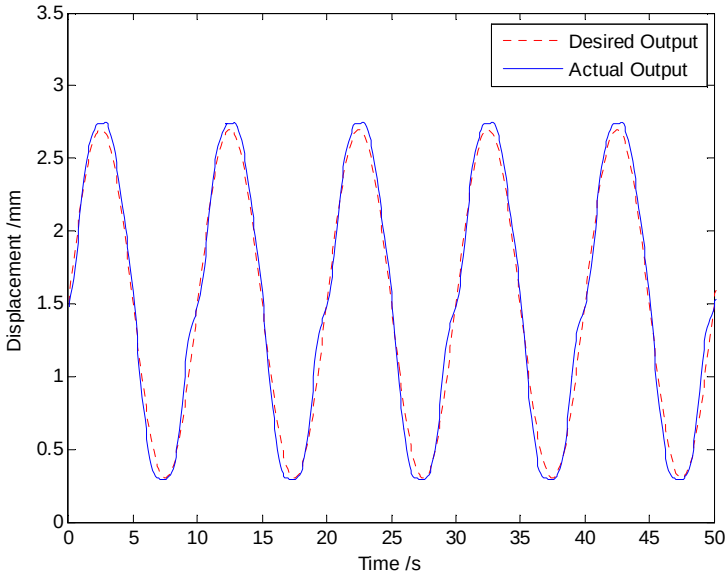


**Figure 4-5: Numerical simulation of inverse NARX Jordan-Elman network model with 0.1 Hz sine wave.**

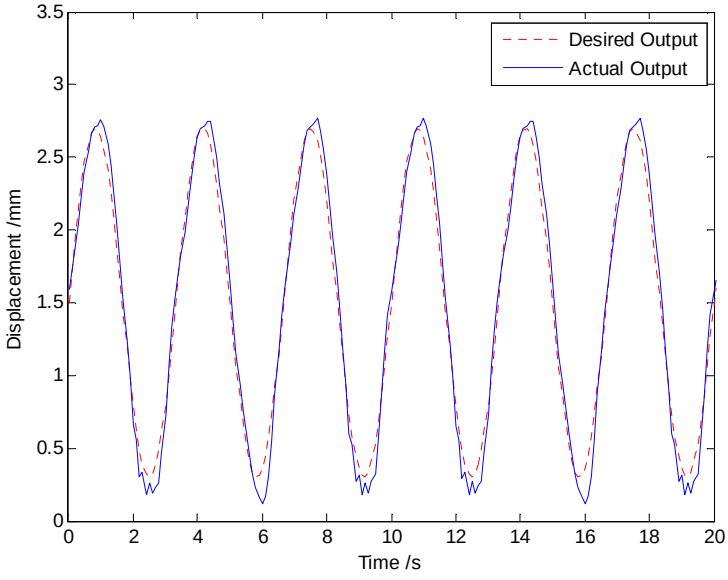


**Figure 4-6: Numerical simulation of inverse NARX Jordan-Elman network model with 0.3 Hz sine wave.**

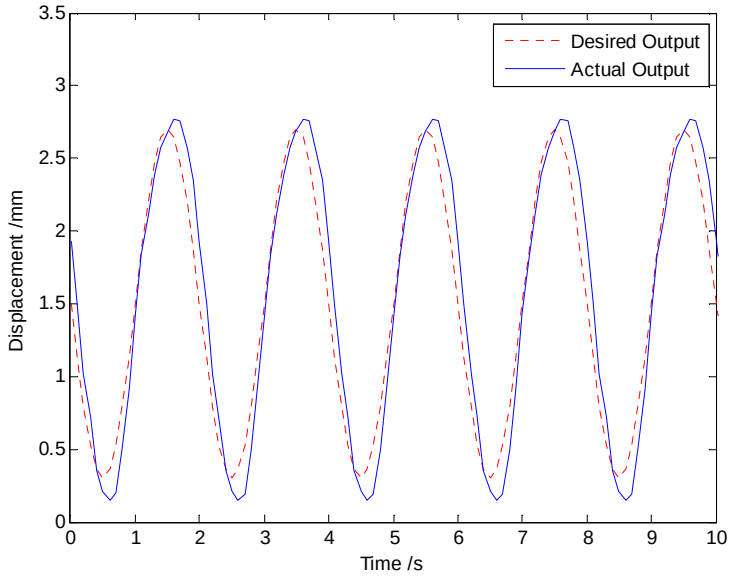


**Figure 4-7: Numerical simulation of inverse NARX Jordan-Elman network model with 0.5 Hz sine wave.**

Table 4-1 shows the summary of the numerical simulation results in the above figures. The performance of the mean absolute errors and the maximum absolute errors are calculated for each frequency.

**Table 4-1: Summary of numerical simulation results to inverse NARX Jordan-Elman network model (Abs.: absolute)**

| Experiment | Figure | Mean Abs. Error (mm) | Max Abs. Error (mm) |
|---|---|---|---|
| 0.05 Hz sine | Figure 4-4 | 0.1027 mm | 0.2883 mm |
| 0.1 Hz sine | Figure 4-5 | 0.0870 mm | 0.2595 mm |
| 0.3 Hz sine | Figure 4-6 | 0.1024 mm | 0.2815 mm |
| 0.5 Hz sine | Figure 4-7 | 0.2003 mm | 0.4734 mm |

From Table 3-1, it is obvious that the inverse NARX Jordan-Elman network mode can track sinusoid waves at various frequencies with limited errors. Since the frequency at 0.5 Hz is the high limit of the data for training, the performance drop at that frequency is predictable.

### 4.2.2 Experimental Results

**1) Inverse NARX RNN model as feedforward controller only**

The same inverse NARX Jordan-Elman network model as a feedforward controller is also applied to the experimental setup as presented in 3.4. Similar to the numerical simulation, reference inputs at frequency of 0.05 Hz, 0.1 Hz, 0.3 Hz and 0.5 Hz are used to test the performance of the feedforward controller. The experimental results are shown in Figure 4-8 through Figure 4-11.

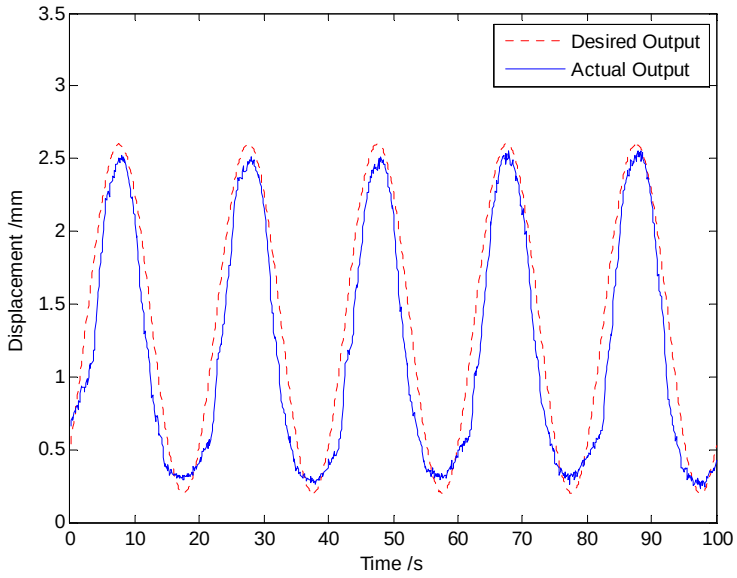


**Figure 4-8: Experimental result of inverse NARX Jordan-Elman network only with 0.05 Hz sine wave.**

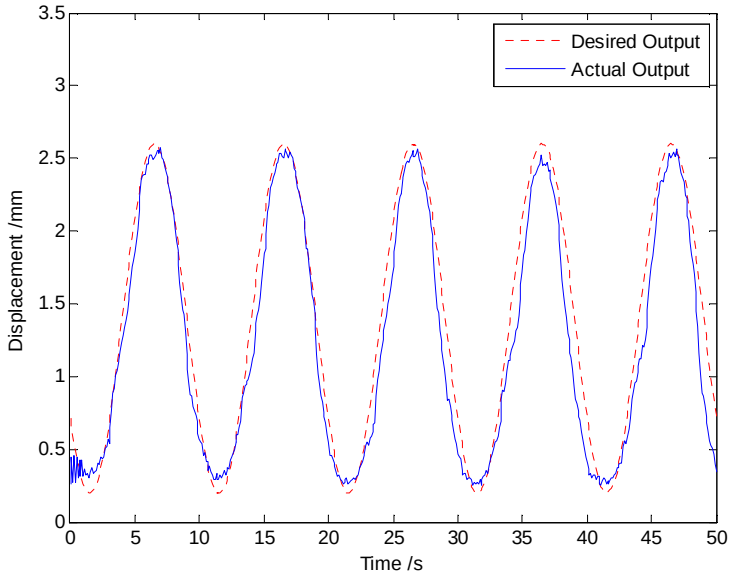


**Figure 4-9: Experimental result of inverse NARX Jordan-Elman network only with 0.1Hz sine wave.**

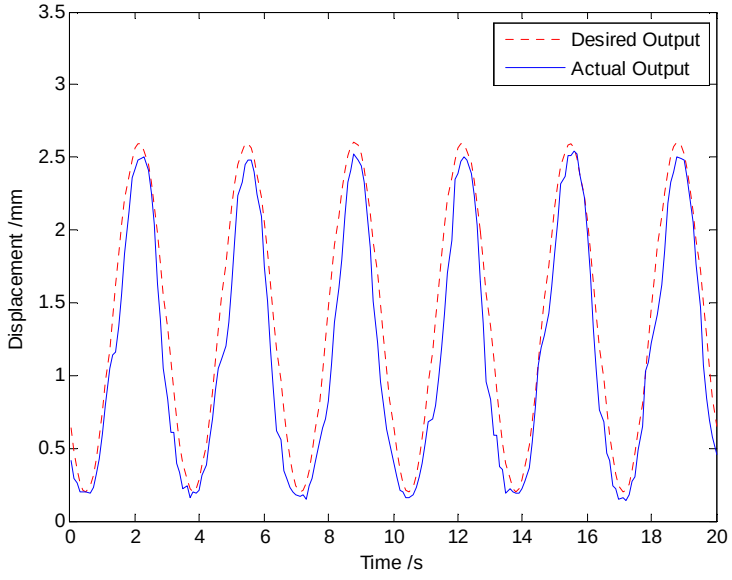


**Figure 4-10: Experimental result of inverse NARX Jordan-Elman network only with 0.3 Hz sine wave.**

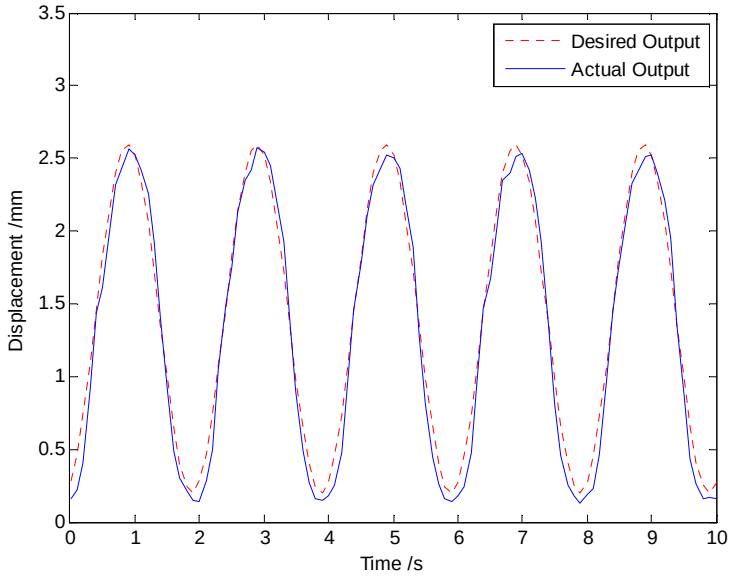


**Figure 4-11: Experimental result of inverse NARX Jordan-Elman network only with 0.5 Hz sine wave.**

As shown in Figure 4-8 through Figure 4-11, the actual outputs (displacement in blue solid curve) are tracking the reference outputs (in red dash curve) with reasonable errors. Since the only feedforward control scheme is applied, the errors are acceptable. Furthermore, the experimental results are found comparable with the numerical results, which again proves that the effectiveness of the forward NARX Jordan-Elman network model. Finally, the experimental results are summarized in Table 4-2 at the end of Section 4.2.2.

**2) Hybrid controller using inverse NARX RNN model**

The control schemes with only feedforward controllers are helpful to situations difficult or even inaccessible to real-time feedback signals or sensor signals. On the other hand, if feedback responses are easy to achieve, a simple feedback controller can dramatically reduce the errors of the tracking controls. As shown in Figure 4-12, a

hybrid controller, consisting of a feedforward controller and a feedback controller, is designed in this subsection.

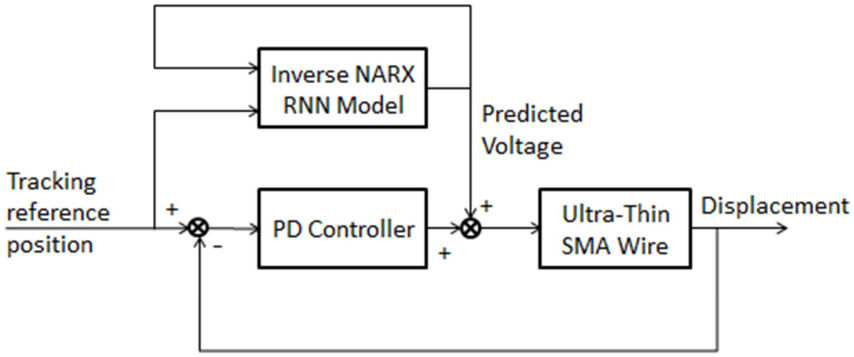


**Figure 4-12: Control scheme of hybrid controller scheme.**

Both the feedforward controller and the feedback controller take information from the reference input. The feedback of the displacement signal only connects to the feedback controller to compensate the error generated by the feedforward controller. The inverse NARX Jordan-Elman network model is used as the feedforward controller, and a simple proportional-derivative (PD) controller is used as the feedback controller. The experimental results of the proposed hybrid controller tracking sinusoid waves with frequencies of 0.05 Hz, 0.1 Hz, 0.3 Hz and 0.5 Hz are shown in Figure 4-13 through Figure 4-16, respectively.

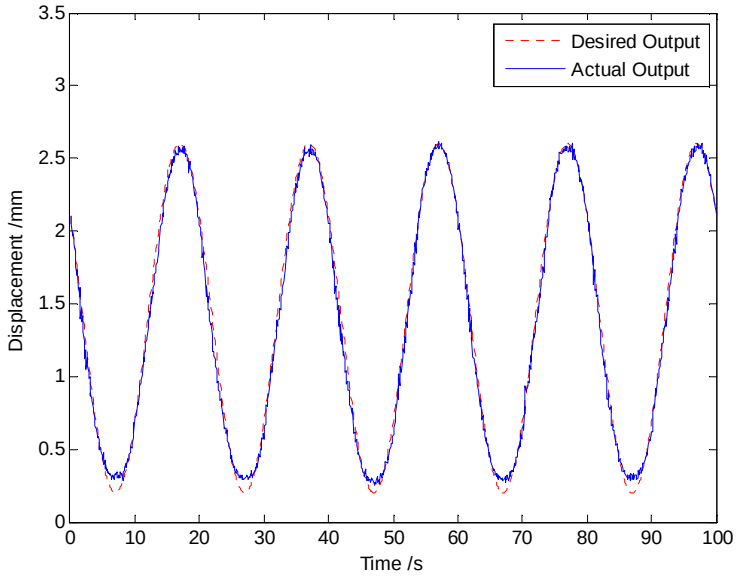


**Figure 4-13: Experimental result of hybrid controller with 0.05 Hz sine wave.**

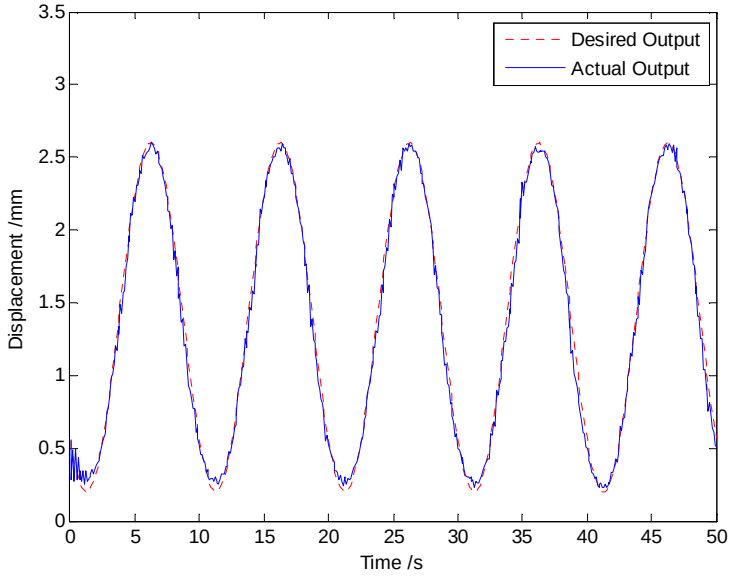


**Figure 4-14: Experimental result of hybrid controller with 0.1 Hz sine wave.**

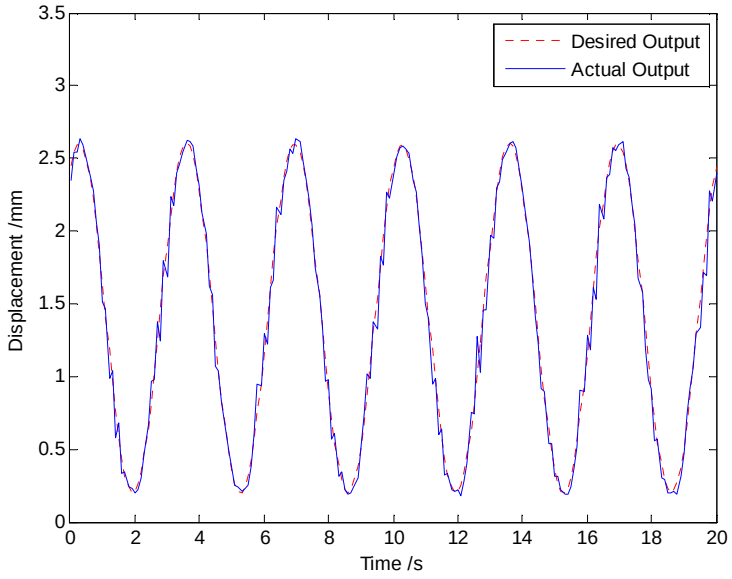


**Figure 4-15: Experimental result of hybrid controller with 0.3 Hz sine wave.**

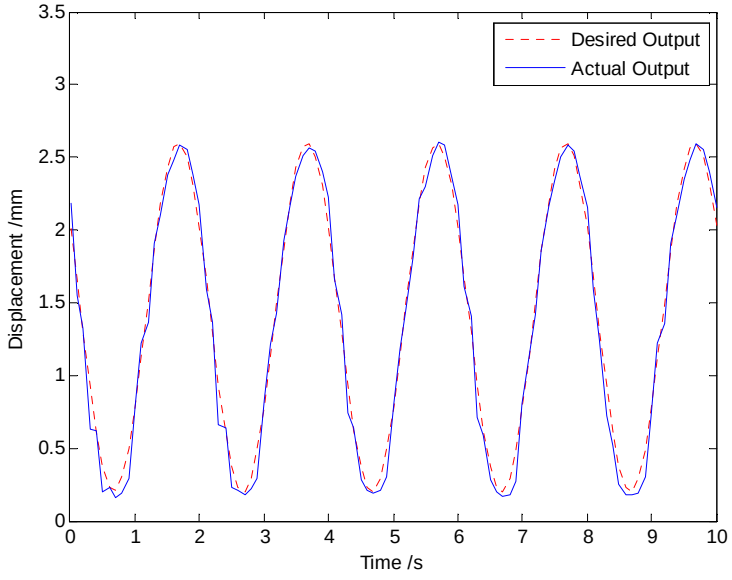


**Figure 4-16: Experimental result of hybrid controller with 0.5 Hz sine wave.**

To evaluate the performance of the hybrid controller under frequency-varying inputs, a chirp signal with frequency range from 0.001 Hz to 0.5 Hz is applied as shown in Figure 4-17, and the corresponding error is shown in Figure 4-18. From the figures, the hybrid controller can track the low frequency signal within considerably small errors, however, for the high frequency part, errors will be dramatically increased to around 0.4 mm. This is possibly caused by the frequency limit of the experimental data used for training is around 0.5 Hz, which happens to be the limit for the hybrid controller. Furthermore, a slight chattering effect can be observed at the beginning of the chirp signal data, which may be caused by an adjustment of the inverse NARX RNN model to compensate the difference to the initial conditions. The observation of this effect also demonstrates the robustness of this control scheme.

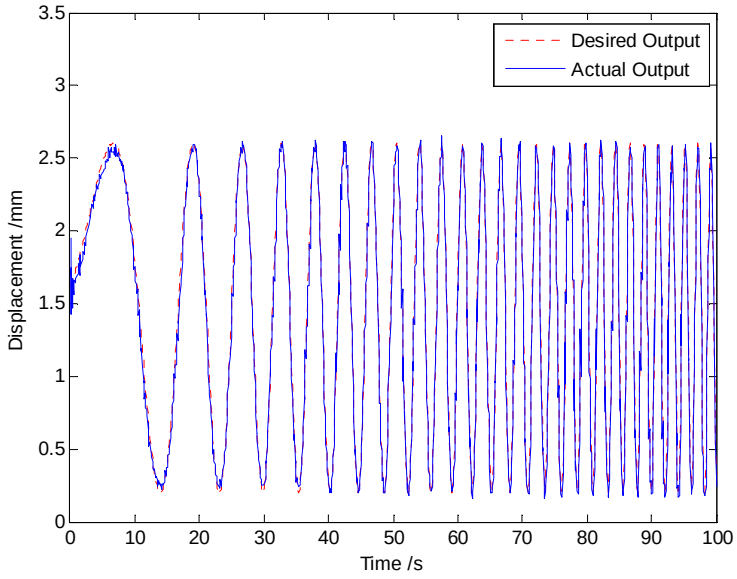


**Figure 4-17: Experimental result of hybrid controller with chirp signal from 0.001 Hz to 0.5 Hz.**

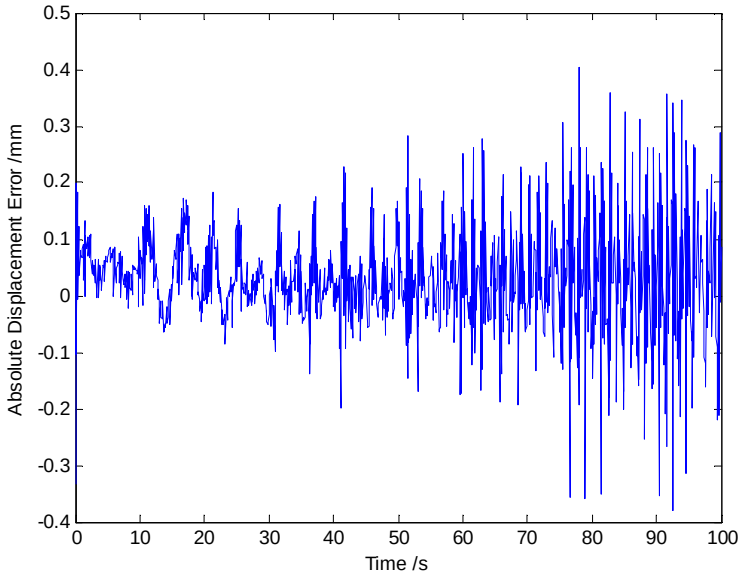


**Figure 4-18: Experimental error of hybrid controller with chirp signal from 0.001 Hz to 0.5 Hz.**

Finally, Table 4-2 presents the summary of the mean absolute errors and the maximum absolute errors for the experimental results comparing the inverse NARX Jordan-Elman network model only and the hybrid controller.

**Table 4-2: Summary of experimental results including mean absolute errors and maximum absolute errors**

| Experiment | Mean Absolute Error (mm) | Max Absolute Error (mm) |
|---|---|---|
| 0.05 Hz inverse | 0.2329 mm | 0.6728 mm |
| 0.05 Hz hybrid | 0.0556 mm | 0.2331 mm |
| 0.1 Hz inverse | 0.1640 mm | 0.6257 mm |
| 0.1 Hz hybrid | 0.0533 mm | 0.2310 mm |
| 0.3 Hz inverse | 0.2284 mm | 0.6373 mm |
| 0.3 Hz hybrid | 0.0664 mm | 0.2947 mm |
| 0.5 Hz inverse | 0.1121 mm | 0.3428 mm |
| 0.5 Hz hybrid | 0.0824 mm | 0.2928 mm |
| Chirp 0.001 Hz to 0.5 Hz hybrid | 0.0705 mm | 0.4036 mm |

From the table above, it is obvious that the hybrid controller will significantly reduce the mean absolute error and the maximum absolute errors. Thus, if the real-time feedback signals are accessible, the hybrid control scheme shall always be a priority choice for tracking control complex nonlinear system such as ultra-thin SMA wires.

To evaluate the adaptability of the proposed hybrid control scheme, square waves are used for testing. Figure 4-19 shows the experimental result of the hybrid controller tracking a 0.1 Hz square wave. To avoid input singularity, steep slope inputs were applied replacing discontinuous step functions. It is obvious that the hybrid controller is able to track the square wave with limited oscillations and errors.

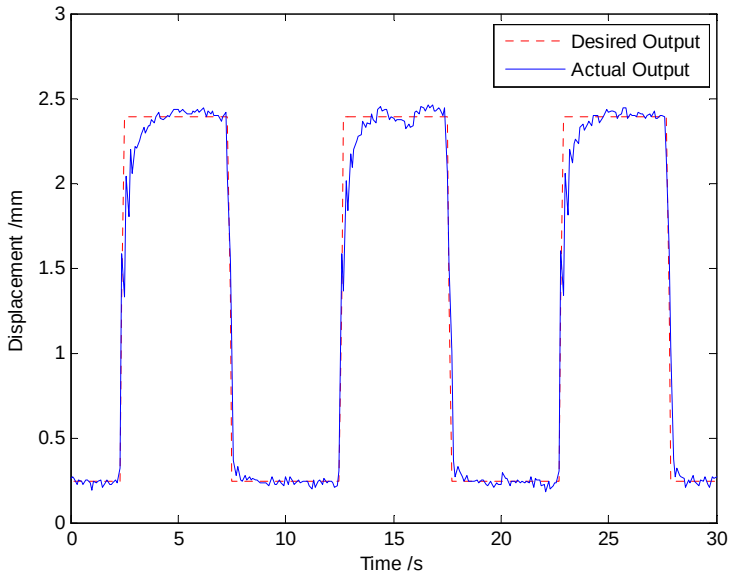


**Figure 4-19: Experimental result of hybrid controller with 0.1 Hz square wave.**

## 4.3 Summary

In this chapter, an inverse NARX Jordan-Elman network model for control purpose was presented mainly to predict control complex nonlinear process as a feedback controller. The inverse model was applied to the experimental setup of the

ultra-thin SMA wire as shown in 3.4 in both numerical simulation and experiment. From the numerical and experimental results, the trained inverse model can successfully track sinusoid reference inputs at various frequencies with reasonable errors. Furthermore, for situations where real-time feedback signals are achievable, a hybrid control scheme was designed to improve the performance of the inverse model by adding a simple feedback controller. The hybrid controller was experimentally proved that it can dramatically improve the performance than inverse NARX Jordan-Elman network model only.

# Chapter 5. Phenomenological Model of Superelastic SMA Helical Springs

As mentioned in the literature review, phenomenolgocal models for helical superelastic SMA springs, as well as its implementation in passive base isolation system, have not been addressed. In this chapter, an innovative phenomenological approach to model superelastic (pseudoelastic) SMA helical springs is introduced. The proposed modeling method is based on experimental bahaviors of SMA springs subjected to cylic strains. Different from SMA wires, the deformation of SMA helical springs is mainly governed by the torsional behavior when the diameter of the SMA is dramatically smaller than the spring diameter. The strain of a helical spring is proportional to the relative displacement when it is loaded. For superelastic SMA springs, the strain induced martensite transformation expands inward from the outer layer of SMA helical springs when loading, and vice versa. Furthermore, the superelastic SMA springs and its modeling approach is applied to an experimental base-isolated structure with results under various types of earthquakes.

## 5.1 Experimental Setup for Superelastic SMA Helical Spring Training and Testing

The proposed phenomennological modeling method is developed based on the experiental hysteric behavior of superelastic SMA helical springs. A superelastic SMA helical spring was trained in Smart Materials and Structures Laboratory, University of Houston by using Nitinol. Figure 5-1 shows the furnace for training SMA springs (b) and the threaded rod (a) used to wind the SMA wire to the shape of helical springs. By

using the threaded rod, high tension during the training should be applied through the SMA wire to achieve a desireable shape and the property of superelastisity. In this chapter, the training procedure includes four cycles of heating at 450 $^{\circ}F$ and cooling down with cold water.

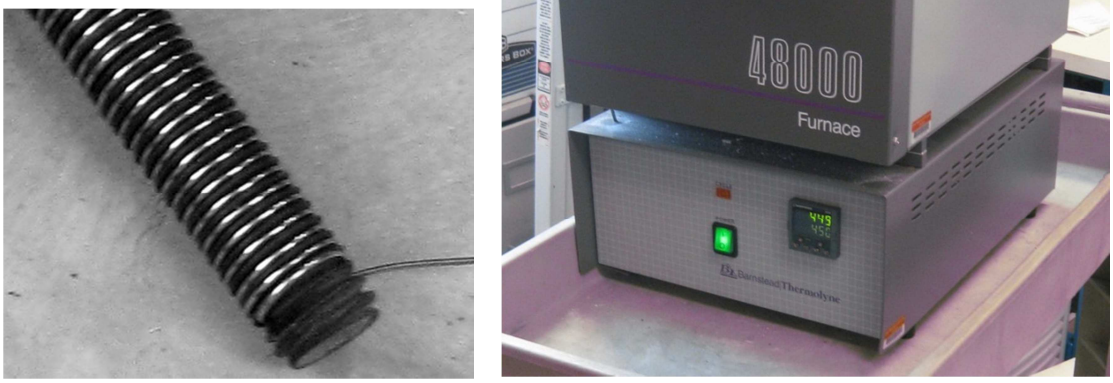


(a) Screw rod with SMA wire winding

(b) Furnace in use for SMA training

**Figure 5-1: Devices for training superelastic SMA helical springs.**

The superelastic SMA spring after training is shown in Figure 5-2. Several turns of coils at both ends were cut to avoid inconsistent performance of the superelastic SMA spring.

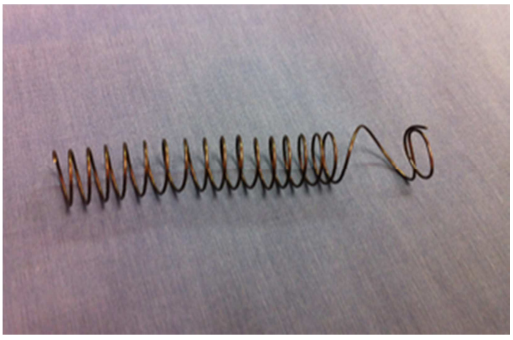

**Figure 5-2: Picture of superelastic SMA spring after training.**

In order to test the hysteric behavior of the trained SMA spring, an experimental setup as shown in Figure 5-3 was used. Partial (~ 5 coils) of the trained SMA spring as shown in Figure 5-2 was pre-strained at 60 mm. This setup includes a linear actuator to apply displacement to the SMA spring, a load sensor to measure the force generated and a sensor transducer. The range of the linear actuator was limited from 0 to 100 mm with an adjustable moving speed. Due to the limitation of the linear actuator, the extending and compressing speed cannot excess 0.1 m/s, and thus, the bandwitdh of this experiment is limited at around 1/20 Hz of triangle waves. All measurements of displacements and load forces were recorded through an A/D converter to the computer.

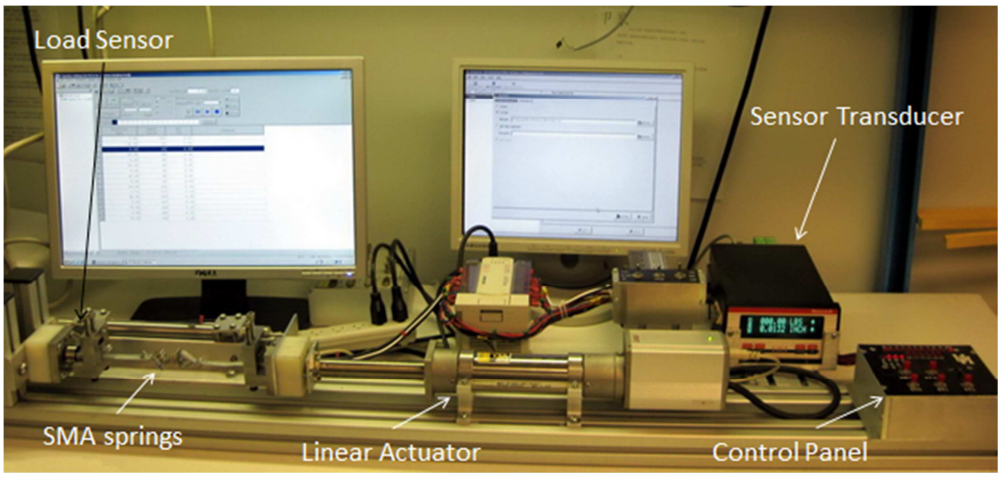


**Figure 5-3: SMA spring testing setup.**

## 5.2 Phenomenological Modeling Method

To identify major loops and minor loops, two technical terms of *inner hysteresis loops* and *outer hysteresis* are used (Thomson *et al*., 1997). The *outer hysteresis loops* refer to the hysteresis curves that start from the origin and end at the origin within one cycle of extension and compression, and on the other hand, the *inner hysteresis loops* refer to the hysteresis curves that do not belong to outer hysteresis loops, for example, the hysteresis curve enclosed by the contour $C \rightarrow D \rightarrow E$ in Figure 5-7 will be considered as an inner hysteresis loop. To find out the behavior of outer hysteresis loops, the input of a triangle wave with various amplitudes, as shown in Figure 5-4, is chosen. The corresponding hysteresis plot of force versus displacement is shown in Figure 5-5 which can be simplified and plot in Figure 5-6.

From Figure 5-5 and Figure 5-6, it is obvious that for the outer hysteresis loops, the hysteresis curves during the extension process ( $A \rightarrow B$ in Figure 5-6) are approximated as a linear straight line. During the compression process, the hysteresis curve can be divided into two individual parts, the nonlinear part ( $B \rightarrow C$ in Figure 5-6) that can be approximated as an exponential function, and the linear part ( $A \rightarrow B$ in Figure 5-6). The critical threshold $x_C$ , as shown in Figure 5-6, should be properly chosen based on experimental testing data.

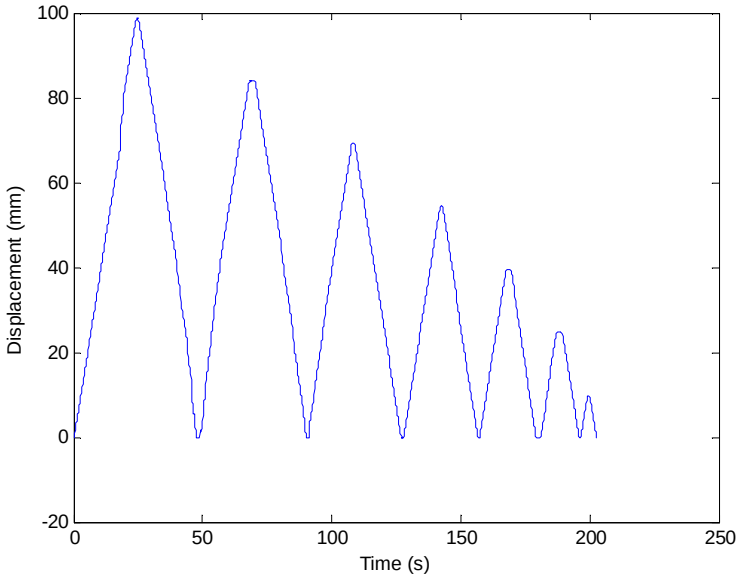


**Figure 5-4: Displacement input for SMA helical spring testing with outer hysteresis loops.**

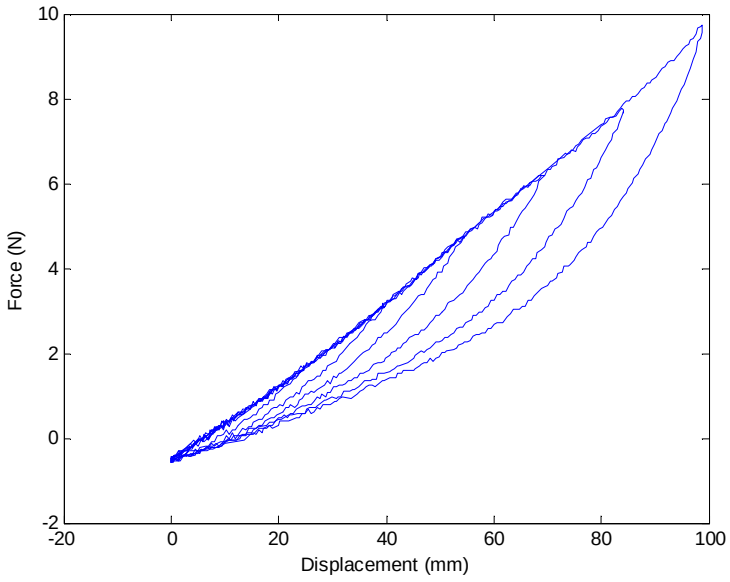


**Figure 5-5: Hysteresis output (force vs. displacement) for the input in Figure 5-4.**

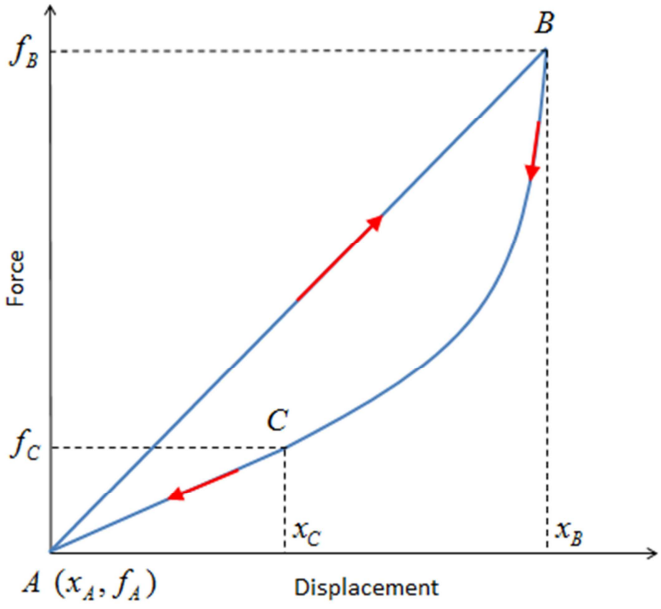


**Figure 5-6: Phenomenological model analysis for outer hysteresis loops.**

Thus, a simple phenomenological model for the outer hysteresis loops can be developed as shown in (Eqn. 5-1)

$$\begin{cases} A \to B: f = k_1 x + b_1 \\ B \to C: f = a_1 e^{c_1 x} \\ C \to A: f = k_2 x + b_2 \end{cases}, \qquad \textbf{(Eqn. 5-1)}$$

where $f$ is the force generated by the SMA spring, $x$ is the relative displacement, $k_1, b_1, a_1, c_1, k_2, b_2$ are coefficients that will be determined by the experimental data. Note that if the point $A$ is assumed fixed at $(x_A, f_A)$, $k_1$ and $b_1$ should be constants calculated from the property of the spring, $a_1$ and $c_1$ are functions determined by the point $B(x_B, f_B)$, and $k_2$ and $b_2$ are functions determined by the point $C(x_C, f_C)$ as

$$a_1 = g_1(x_B), \qquad \textbf{(Eqn. 5-2)}$$

$$c_1 = h_1(x_B), \qquad \textbf{(Eqn. 5-3)}$$

$$k_2 = \frac{f_C - f_A}{x_C - x_A}, \quad \textbf{(Eqn. 5-4)}$$

$$b_2 = \frac{f_A x_C - f_C x_A}{x_C - x_A}, \quad \textbf{(Eqn. 5-5)}$$

where the functions $g_1(\bullet)$ and $h_1(\bullet)$, that are normally linear or polynomial functions, depend on the experimental behaviors of the outer hysteresis loops with various amplitudes.

To model inner hysteresis loops, Figure 5-7 shows the simplified hystersis curve including one innner hysteresis loop. As shown in the figure, with one cycle of extension and compression, the curve does not retrieve back to the origin $A$, but extend for another cycle from the point $C$ that is in the middle of the compression curve of the outer hysteresis loops. Due to the experimental bahaviors, the extension curve $C \rightarrow D$ can be also approximated as a linear straight line connecting the point $C$ and the point $B$ with different slope and bias comparing to the strainght line $A \rightarrow B$. Furthermore, with a sufficient extension, the curve $C \rightarrow D$ will pass the point $B$ (dash line in Figure 5-7) and may continue extending as part of a outer hysteresis loop shown in (Eqn. 5-1). On the contrary, if the curve $C \rightarrow D$ does not surpass the point $B$, the SMA spring will be compressed again with an approximately exponential hysteresis that will contain a bias without passing the origin point $A$.

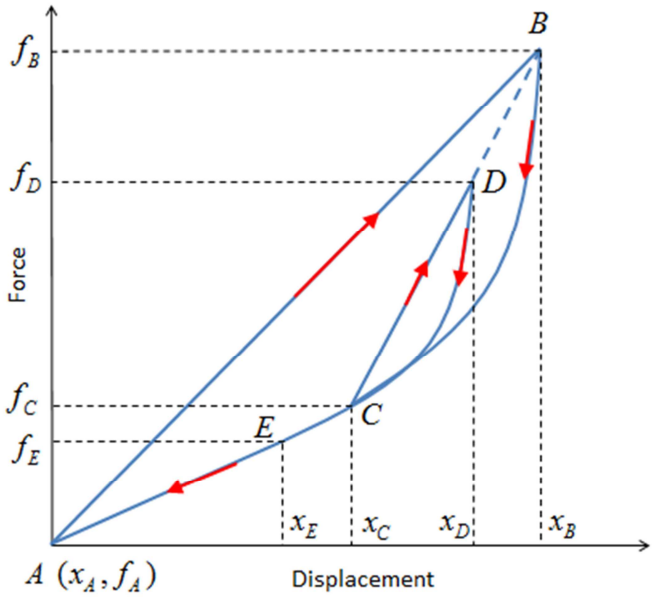


**Figure 5-7: Phenomenological model analysis for outer and inner hysteresis loops.**

Thus, the total equations for the phenomenological model are

$$\begin{cases} A \to B: f = k_1 x + b_1 \\ B \to C: f = a_1 e^{c_1 x} \\ C \to D: f = k_3 x + b_3 \\ D \to E: f = a_2 e^{c_2 x} + b_4 \\ E \to A: f = k_2 x + b_2 \end{cases}, \qquad \textbf{(Eqn. 5-6)}$$

where $k_1, b_1, a_1, c_1, k_2, b_2$ are the coefficient described in (Eqn. 5-1), and $k_3, b_3, a_2, c_2, b_4$ are calculated as

$$k_3 = \frac{f_B - f_C}{x_B - x_C}, \qquad \textbf{(Eqn. 5-7)}$$

$$b_3 = \frac{f_C x_B - f_B x_C}{x_B - x_C}, \qquad \textbf{(Eqn. 5-8)}$$

$$a_2 = g_2(x_D), \qquad \textbf{(Eqn. 5-9)}$$

$$c_2 = h_2(x_D), \qquad \textbf{(Eqn. 5-10)}$$

$$b_4 = k_1 x_D + b_1 - f_D . \quad \textbf{(Eqn. 5-11)}$$

Since the superelastic SMA helical springs have similar hysteretic behaviors (Huang *et al*., n.d.; Attanasi *et al*., 2011), this proposed phenomenological model can be used for general hysteresis modeling. In the following section, this model will be validated according to the self-trained superelastic SMA springs as shown in Figure 5-2.

## 5.3 Experimental Modeling Validation

By using the experimental data plot and the proposed phenomenological model, the following coefficients as shown in (Eqn. 5-1) and (Eqn. 5-5) are chosen in this section:

$$a_1 = -5.50 \cdot 10^{-6} x_B^2 + 1.45 \cdot 10^{-3} x_B + 2.38 \cdot 10^{-1}, \quad \textbf{(Eqn. 5-12)}$$

$$c_1 = 3.74 \cdot 10^{-6} x_B^2 - 9.62 \cdot 10^{-4} x_B + 9.27 \cdot 10^{-2}, \quad \textbf{(Eqn. 5-13)}$$

$$k_1 = 0.10, \quad \textbf{(Eqn. 5-14)}$$

$$b_1 = -0.72, \quad \textbf{(Eqn. 5-15)}$$

Note that $a_1$ and $c_1$ are calculated based multiple outer hysteresis loops from the experimental data in Figure 5-5. For simplification purpose, we choose $g_1(\bullet) = g_2(\bullet)$ and $h_1(\bullet) = h_2(\bullet)$, and the threshold point is selected at $x_C (\text{or } x_E) = 25mm$.

A total of 9 sets of experiments were performed to verify the hysteresis performance of the phenomenological model in various situations including outer hysteresis loops, inner hysteresis loops and their combinations. The comparative results are shown in Figure 5-8 through Figure 5-16, and summarized in Table 5-1.

**Table 5-1: Summary of model validation results in Figure 5-8 through Figure 5-16**

| Displacement Input (mm) | Figure | Mean Squared Errors |
|---|---|---|
| 0 – 100 – 0 … in various frequencies | Figure 5-8 | 0.036 |
| 0 – 100 – 0 – 80 – 0 – 60 – 0 – 40 – 0 – 20 | Figure 5-9 | 0.017 |
| 0 – 40 – 10 – 60 – 30 – 80 – 50 – 100 – 70 - 100 | Figure 5-10 | 0.045 |
| 0 – 80 – 60 – 80 – 40 – 80 – 20 – 80 – 0 | Figure 5-11 | 0.034 |
| 0 – 60 – 50 – 60 – 40 – 60 – 30 – 60 – 20 – 60 – 10 – 60 – 0 | Figure 5-12 | 0.012 |
| 0 – 100 – 20 – 80 – 20 – 60 – 20 – 40 – 0 | Figure 5-13 | 0.018 |
| 0 – 100 – 40 – 80 – 20 – 60 – 0 | Figure 5-14 | 0.033 |
| 0 – 60 – 20 – 80 – 40 – 100 – 0 | Figure 5-15 | 0.020 |
| 0 – 100 – 20 – 80 – 40 – 60 – 0 | Figure 5-16 | 0.022 |

As shown in Figure 5-8 through Figure 5-16 and Table 5-1, the proposed model can successfully track both outer and inner hysteresis loops in various situations.

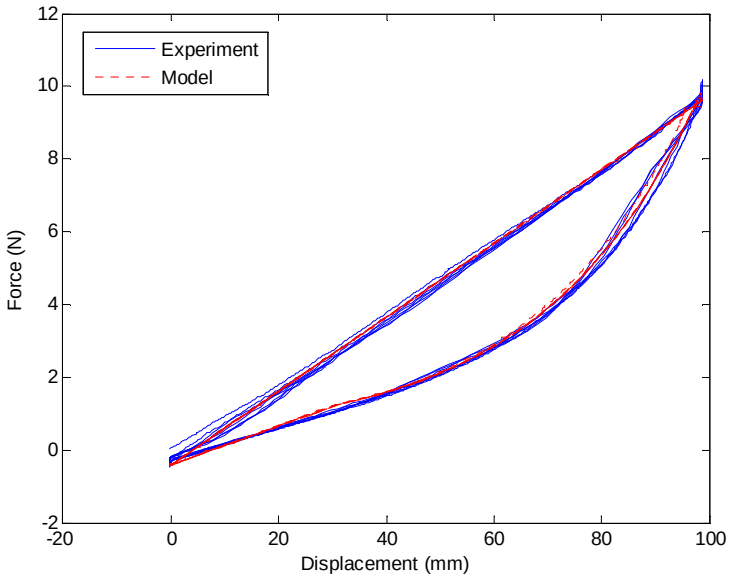


**Figure 5-8: Model validation for outer hysteresis loops (major loops) with various frequencies.**

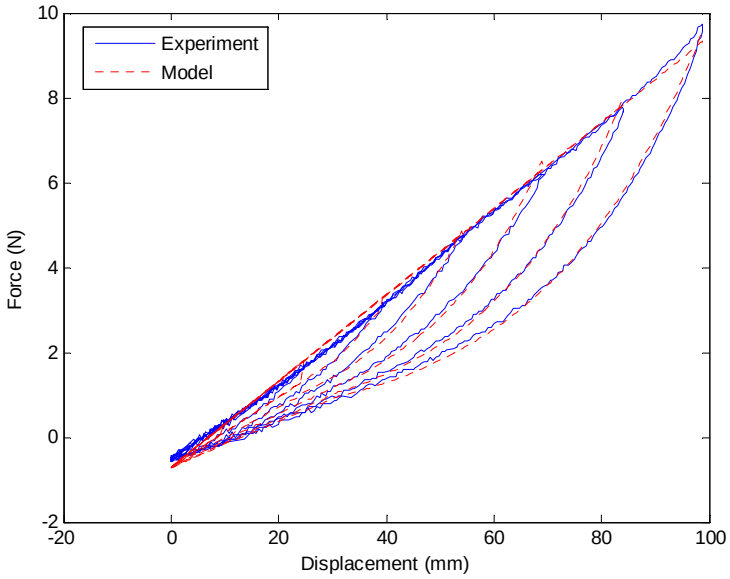


**Figure 5-9: Model validation of outer hysteresis loops starting from origin.**

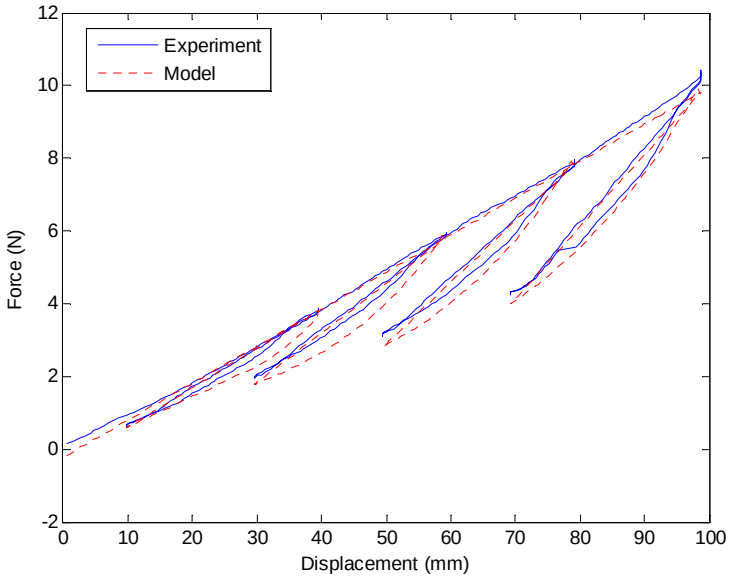


**Figure 5-10: Model validation of inner hysteresis loops with multiple starting points.**

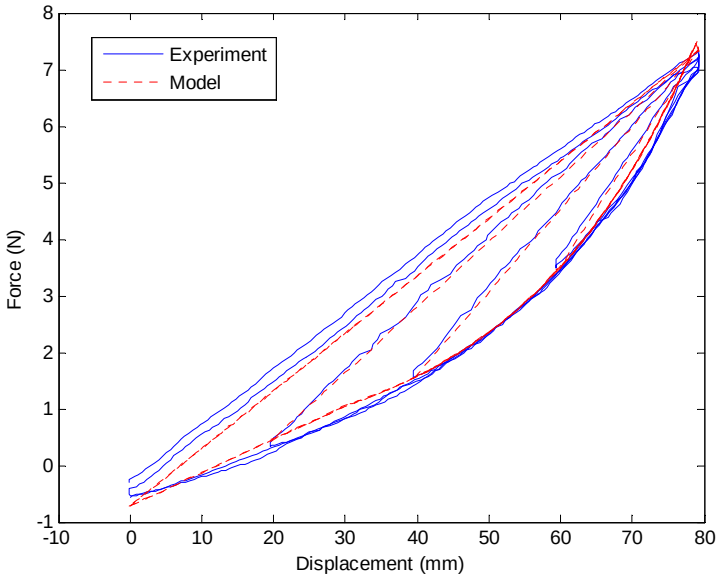


**Figure 5-11: Model validation of inner hysteresis loops with multiple starting points and ends at 80 mm.**

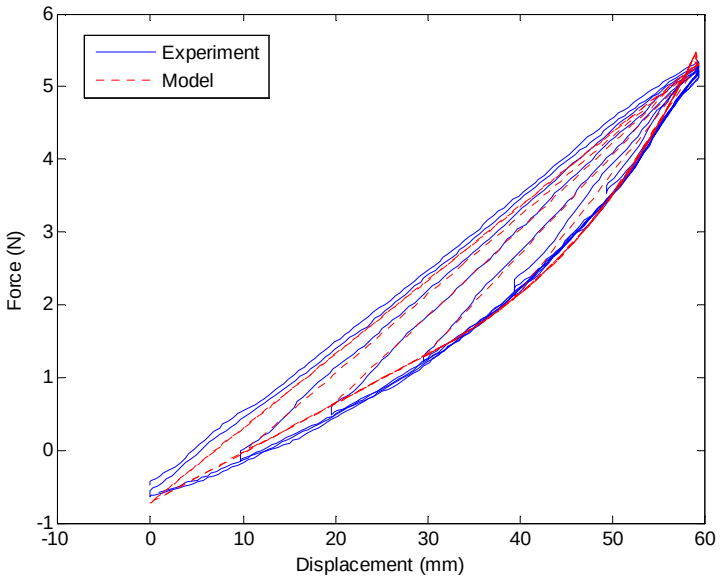


**Figure 5-12: Model validation of inner hysteresis loops with multiple starting points and ends at 60 mm.**

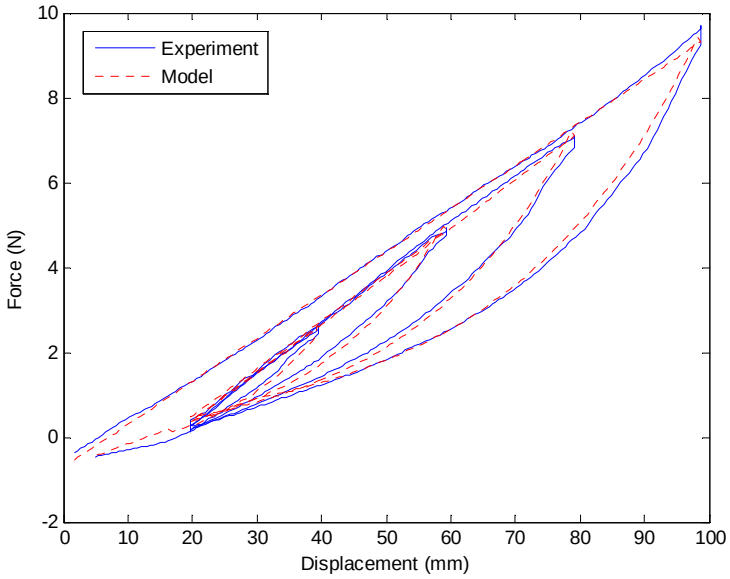


**Figure 5-13: Model validation of inner hysteresis loop with starting point at 20 mm and multiple ending points.**

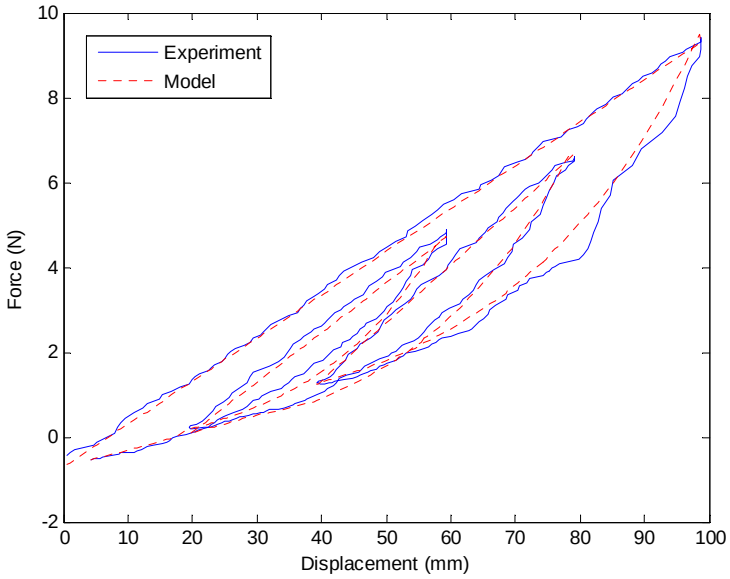


**Figure 5-14: Model validation of inner hysteresis loops with multiple starting and ending points (inner hysteresis loops start from the downward curve).**

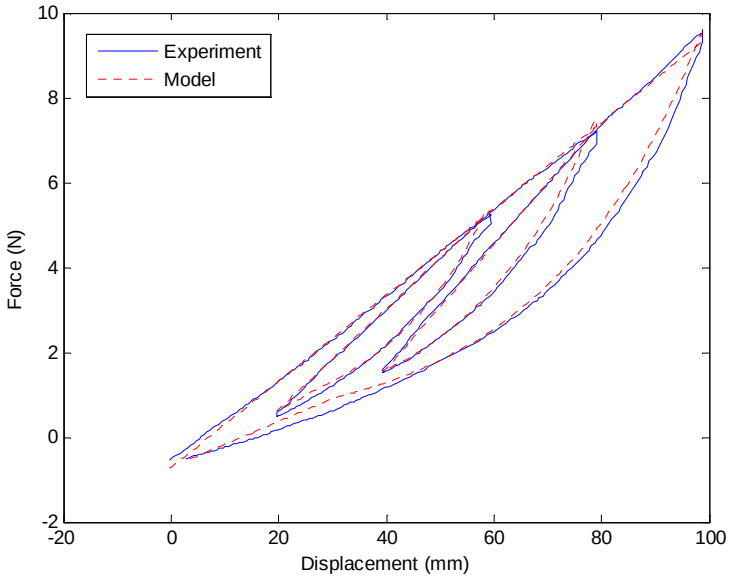


**Figure 5-15: Model validation of inner hysteresis loops with multiple starting and ending points (inner hysteresis loops start from the upward curve).**

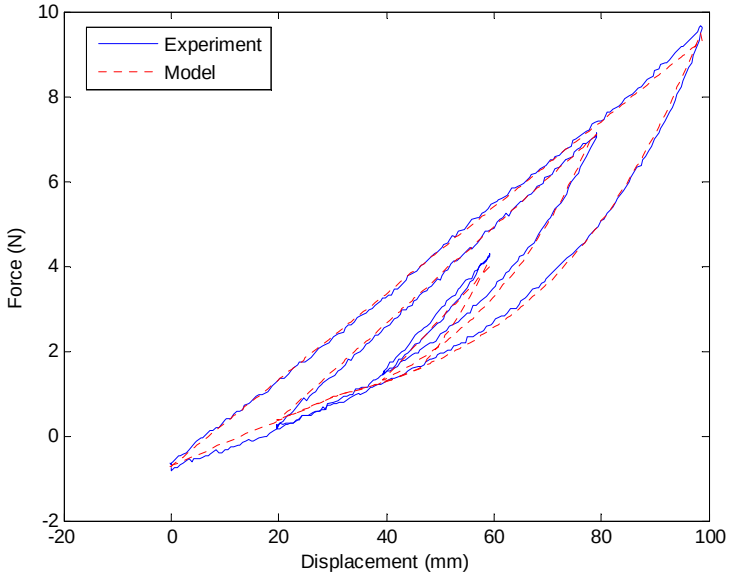


**Figure 5-16: Model validation of inner hysteresis loops with multiple starting and ending points (inner hysteresis loops are enclosed in others).**

## 5.4 Implementation of Superelastic SMA Helical Springs in Base Isolation Systems

As mentioned in previous sections, since superelastic SMA helical springs can behave as a restoring spring, and dissipate energy at the same time, in this section, we propose the implementation of superelastic SMA helical springs in the base isolation systems to passively suppress structural vibrations. In seismic engineering, for resisting strong horizontal earthquakes, stiffness of base isolator such as linear slider is designed to be much smaller than that of upper structure so that structural vibration frequency is kept away from the predominant frequency of possible earthquake. Such design may not be suitable for all types of earthquakes, especially dominant at low frequencies.

In this section, an experimental base isolation structural model as well as the corresponding mathematical model is built. Components and build procedure of the model are introduced and then tested with the model parameters. Two superelastic SMA helical springs are connected on both sides of the base-isolated structure as passive damping and energy dissipation devices. Both springs are pre-strained at 50 mm with 4 coils.

### 5.4.1 Experimental Setup of Base Isolation System

To study the effectiveness of advanced damping devices on base isolation systems, a two-story steel structural model, as shown in Figure 5-17, was experimentally built in Smart Materials and Structures Laboratory, University of Houston. The structural model utilizes a single-axis linear slider (M4410 by Parker Daedal, as shown in Figure 5-18) to isolate the structure base with the simulated ground (shaker). The datasheet of the linear slider can be found in Table 5-2. Two identical

restore springs are attached to the structural base to generate restore forces. The masses for each floor are measured as $m_1 = 1.96kg$, $m_2 = 1.26kg$, and $m_3 = 1.21kg$. The stiffness are measured for each side wall between floors as $k_1 = 1218.6N/m$ and $k_2 = 1497.7N/m$ The kinetic friction $F_f$ is measured at 0.18N.

**Table 5-2: Datasheet of M4410 linear slider by Parker Daedal**

| Travel Range | Normal Load | Accuracy | Size |
|---|---|---|---|
| $76.2mm$ | $48kg$ | $2\mu m/25mm$ | $127mm \times 127mm$ |

Aluminum sheets with a size of 205.7 mm × 50.7 mm × 6.51 mm are selected for each floor, and thin steel sheets with a size of 50.69 mm × 175.5 mm × 0.75 mm are used for the structural side walls. To enhance the stiffness of the connections between the floors and the side walls, strengthen bars with a thickness of 2 mm are added and fixed by using screws.

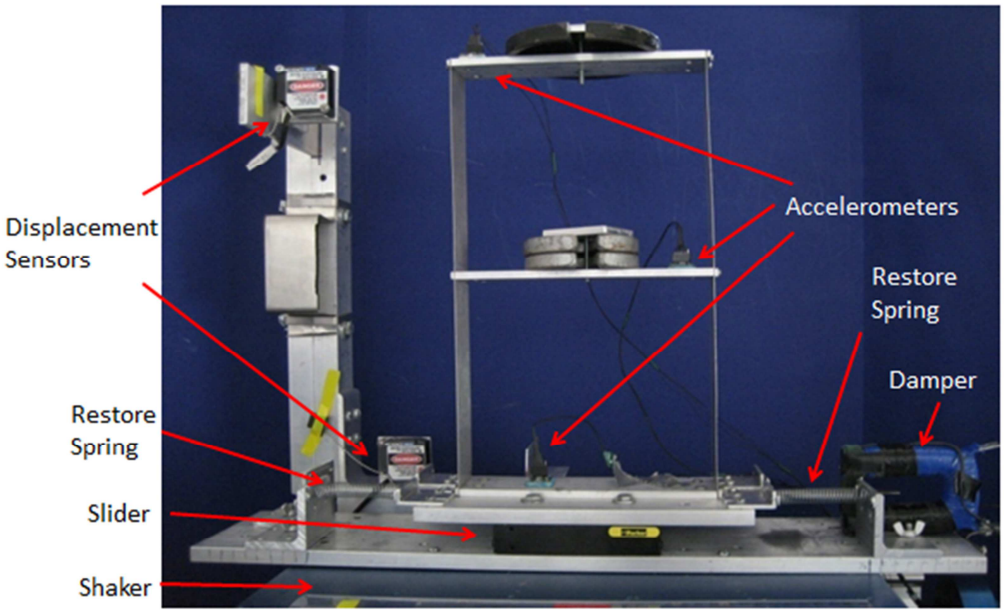


**Figure 5-17: Experimental setup of base isolation structural model.**

**Figure 5-18: M4410 linear slider by Parker Daedal.**

The shaking table used on this model is the Shaker II by Quanser Company. Customized earthquake wave signals from real earthquakes can be simulated. Major components can be found in Figure 5-19, and the parameters of Shaker II are shown in Table 5-3.

**Table 5-3: Parameters of Shaker II**

| **Specification** | **Value** | **Unit** |
|---|---|---|
| Overall dimensions (L×W×H) | 61×46×13 | cm |
| Table dimensions | 46×46 | cm |
| Table Travel | ±7.5 | cm |
| Table operational bandwidth | 20 | Hz |
| Table peak velocity | 83.8 | cm/s |
| Table peak acceleration | 24.5 | $m/s^2$ |
| Motor maximum torque | 1.65 | N·m |
| Table bearing load carrying capability | 930 | kg |
| Accelerometer range | ±49 | $m/s^2$ |
| Accelerometer sensitivity | 1/9.81 | $V \cdot s^2/m$ |


**Figure 5-19: Components of Shaker II system.**

As shown in Figure 5-17, the displacement of the base and second floor can be measured by two individual laser displacement sensors. The laser displacement sensors mounted on a structural model are the LB-70 series product by KEYENCE Company with a measurement range of 100 mm ±40 mm, a response time of 0.7 ms (at sensitivity of 180 μm), and a maximum sensitivity of 10 μm (at response time of 500 ms). Accelerations of the floors and the base are captured by accelerometers attached on each floor. The product number of the accelerometers is ADXL203EB Rev.0 by Analog Device Company. The measurement range is ±1.7 g, and the sensitivity is 1 mg in 60 Hz. Therefore, those sensors completely satisfy the requirement of the experiments.

The dSPACE board, with product number DS1104 R&D Controller board and communication board CLP 1104, is used as data acquisition and output system. This board can communicate with Matlab/Simulink program in the computer (via analog-to-

digital converter and digital-to-analog converter) and control voltage/current signals in real-time.

### 5.4.2 Mathematical Model of Base Isolation System

The mathematical model is developed based on the experimental setup in the previous section. Unlike normal structures with fixed base, base isolation structure enables a building or a non-building structure to have the advantages of a free-moving base. For example, as shown in Figure 5-20, a linear slide is used to simulate a free-moving base in three degrees of freedom (DOF) structure model. Two identical superelastic SMA springs are utilized to dissipate seismic energy and restore initial positions.

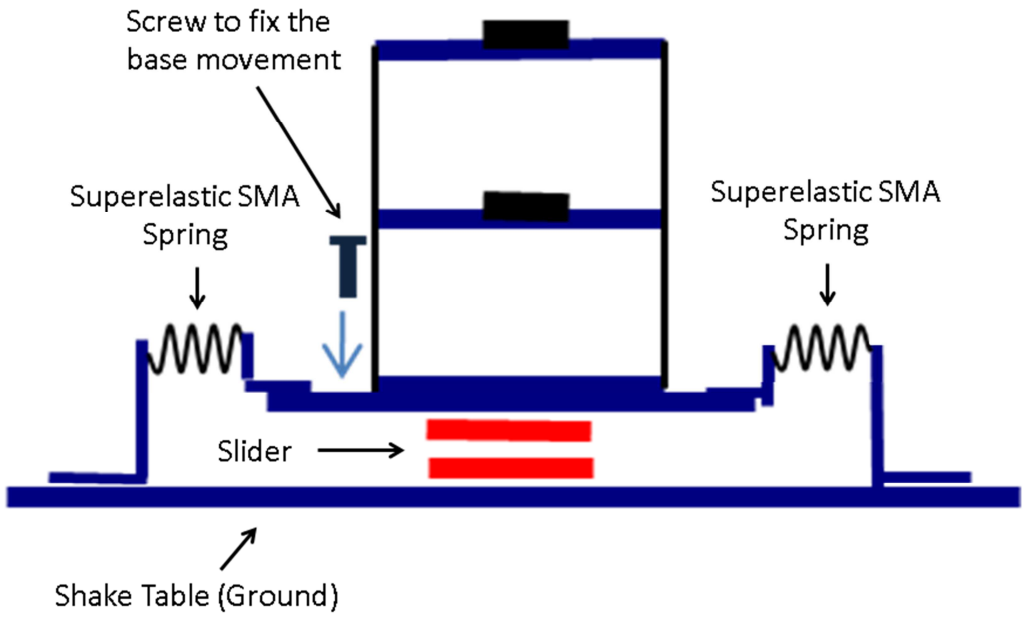


**Figure 5-20: Diagram of the base-isolated structural model with superelastic SMA springs.**

The system can be described as below:

$$M\ddot{X} + C\dot{X} + KX = -m\ddot{x}_g + F\ , \qquad \textbf{(Eqn. 5-16)}$$

where $M$ is the mass matrix, $C$ is the damping matrix, $K$ is the stiffness matrix, $X$ is the displacement vector, and $F$ is the external force input vector, as

$$M = \begin{bmatrix} m_3 & 0 & 0 \\ 0 & m_2 & 0 \\ 0 & 0 & m_b \end{bmatrix}, K = \begin{bmatrix} k_2 & -k_2 & 0 \\ -k_2 & k_1 + k_2 & -k_1 \\ 0 & -k_1 & k_1 + k_b \end{bmatrix}, F = \begin{Bmatrix} 0 \\ 0 \\ F_{SMA} - F_f \operatorname{sgn}(\dot{x}_b) \end{Bmatrix},$$
$$X = \begin{Bmatrix} x_2 \\ x_1 \\ x_b \end{Bmatrix}, C = \begin{bmatrix} c_2 & -c_2 & 0 \\ -c_2 & c_1 + c_2 & -c_1 \\ 0 & -c_1 & c_1 \end{bmatrix} \qquad \textbf{. (Eqn. 5-17)}$$

where $m_3, m_2, m_b$ are the mass for the second floor, the first floor and base, respectively, $k_2, k_1$ are the inter-story stiffness, $k_b$ is the combined stiffness of the restore springs, $F_f$ is the friction force of slider, $F_{SMA}$ is the force generated by the superelastic SMA springs on both sides of the structural model, $\ddot{x}_g$ is earthquake wave input, $x_b, x_1$ and $x_2$ are the displacements of base, the first floor and the second floor, respectively, and $\operatorname{sgn}(\dot{x}_b)$ is a function shown in

$$\operatorname{sgn}(\dot{x}_b) = \begin{cases} 1 & (\dot{x}_b > 0) \\ 0 & (\dot{x}_b = 0) \\ -1 & (\dot{x}_b < 0) \end{cases}. \qquad \textbf{(Eqn. 5-18)}$$

In order to achieve the damping matrix, the Rayleigh damping theory is used to model the structural damping. Consider the structural model without the base isolation part, and thus, the mass matrix and stiffness matrix for the fixed structure are

$$M' = \begin{bmatrix} m_2 & 0 \\ 0 & m_1 \end{bmatrix}, K' = \begin{bmatrix} k_2 & -k_2 \\ -k_2 & k_1 + k_2 \end{bmatrix}. \qquad \textbf{(Eqn. 5-19)}$$

From (Eqn. 5-19), the natural frequencies at first mode $\omega_1$ and second mode $\omega_2$ as well as the matrix of modal shape $\Phi$ can be calculated. Thus, the general mass matrix $M^*$ is

$$M^* = \Phi^T M' \Phi . \qquad \textbf{(Eqn. 5-20)}$$

If the damping ratios for the first mode and second mode are $\xi_1$ and $\xi_2$, respectively, the damping matrix for the fixed structure can be calculated as

$$C' = M'\Phi D \Phi^T M' = \begin{bmatrix} c_2 & -c_2 \\ -c_2 & c_1 + c_2 \end{bmatrix}, \qquad \textbf{(Eqn. 5-21)}$$

where $D$ is a diagonal matrix as

$$D = \begin{bmatrix} d_1 & 0 \\ 0 & d_2 \end{bmatrix}, d_n = \frac{2\xi_n \omega_n}{M_n^*}, n = 1, 2 , \qquad \textbf{(Eqn. 5-22)}$$

where $M_n^*$ is the *nth* diagonal element of the general mass matrix.

(Eqn. 5-21) can be modified to achieve the damping matrix of the base isolation structure model as shown in (Eqn. 5-17).

To obtain the state space model, let $\tilde{X} = \begin{bmatrix} X \\ \dot{X} \end{bmatrix}$, then

$$\dot{\tilde{X}} = \begin{bmatrix} 0 & I \\ -M^{-1}K & -M^{-1}C \end{bmatrix} \tilde{X} + \begin{bmatrix} 0 & 0 \\ -1 & M^{-1} \end{bmatrix} \begin{Bmatrix} \ddot{x}_g \\ F \end{Bmatrix}. \qquad \textbf{(Eqn. 5-23)}$$

Therefore, the mathematical base isolation model can be simulated using the equation above.

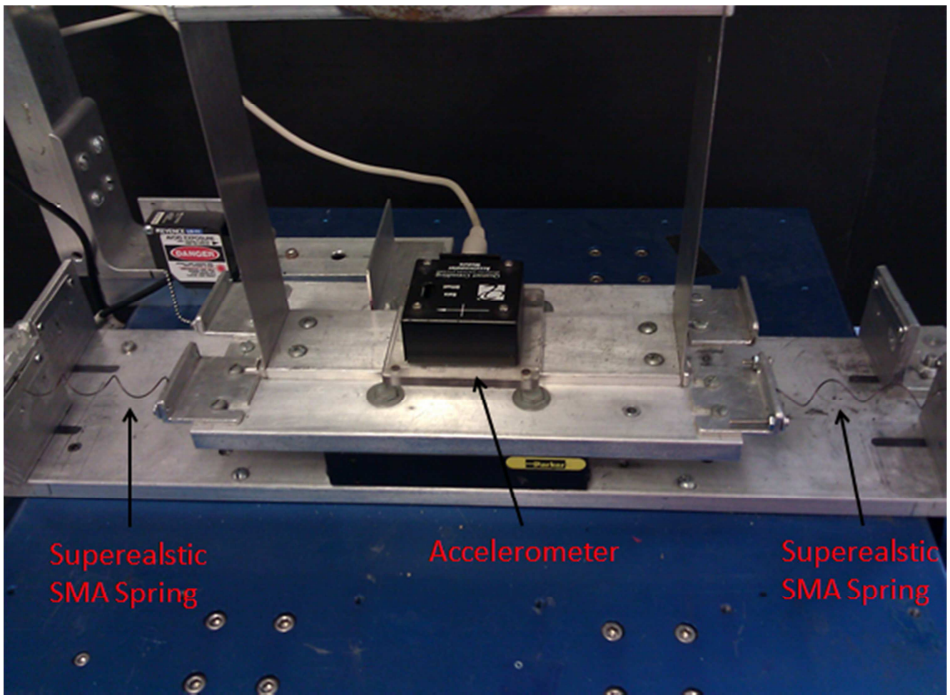


**Figure 5-21: Zoom-in picture of base-isolated structure with superelastic SMA springs.**

### 5.4.3 Experimental Results

In this chapter, both springs are pre-strained at 50 mm with 4 coils. Based on the experimental data of free vibration at each mode, in this section, the damping ratios for each mode are assumed as $\xi_1 = \xi_2 = 0.0014$. The structural performance should be compared in two parts: one is the time response comparing the vibration amplitude and the other is the maximum structural response. Furthermore, three parameters will be compared including the relative displacement between the 2$^{nd}$ floor and the base that can cause damage to the structure, the 2$^{nd}$ floor (top floor) acceleration that may lead to discomfort for people inside, and the base movement that should be limited for experimental applications. Four different types of earthquake including El Centro, Kobe, North Ridge and Hachinohe with the PGA of 0.1g are applied to the experimental base-isolated structure.

First, the El Centro earthquakes have relative weaker responses, and last longer at the same Peak Ground Acceleration (PGA) among these four earthquakes. The acceleration of the 0.1g El Centro earthquake is shown in Figure 5-22.

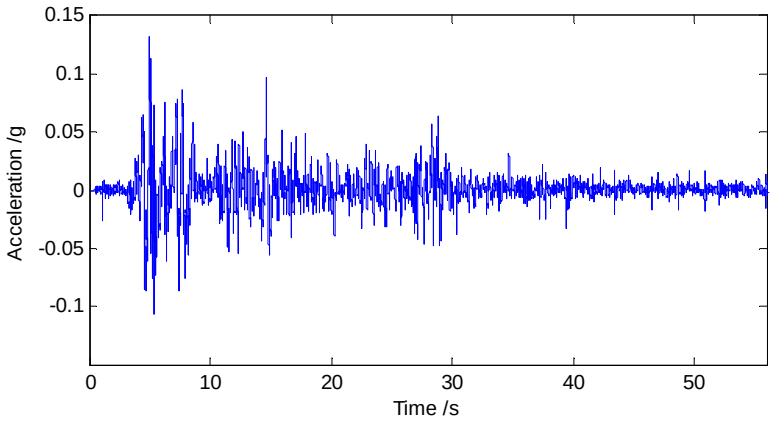


**Figure 5-22: Plot of El Centro earthquake in acceleration.**

The phenomenological model of the superelastic SMA spring sample is validated under the El Centro earthquake excitation. Figure 5-23 shows the model validation of the 2$^{nd}$ floor acceleration, and Figure 5-24 shows the relative displacement. Apparently, for the 2$^{nd}$ floor acceleration, the phenomenological model (red dash curve) of the superelastic SMA spring sample can track the experimental result (blue solid curve) with considerably limited error (MAE: 0.0952 mm). On the other hand, the relative displacement of the model performs acceptable with a MAE of 0.2277 mm, but not as good as the 2$^{nd}$ floor acceleration.

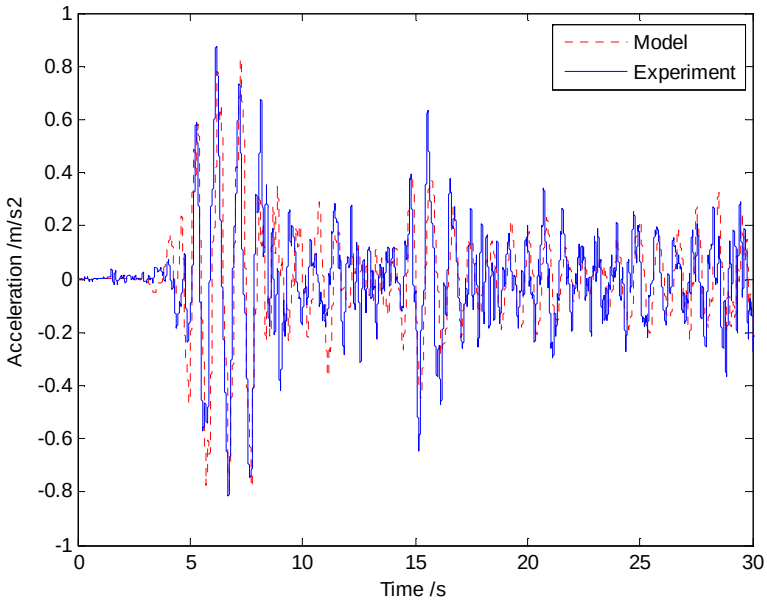


**Figure 5-23: Experimental model validation of 2nd floor acceleration under El Centro 0.1g earthquake.**

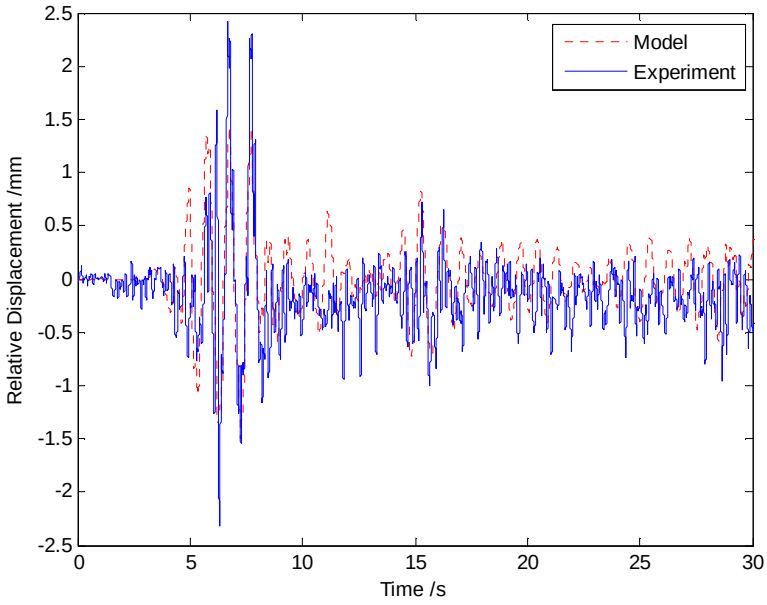


**Figure 5-24: Experimental model validation of relative displacement under El Centro 0.1g earthquake.**

Thus, the above figures have proved that the phenomenological model of the superelastic SMA spring sample is successful and acceptable for both the extension experiments and the earthquake experiments.

Then, we seek the performance of the base-isolated structure can be improved by utilizing superelastic SMA springs. Four sets of experiments with four different types of earthquake are conducted in subsection. Figure 5-25 and Figure 5-26 show the performance comparisons under the El Centro 0.1g earthquake between the base-fixed structure and the base-isolated structure with superelastic SMA springs.

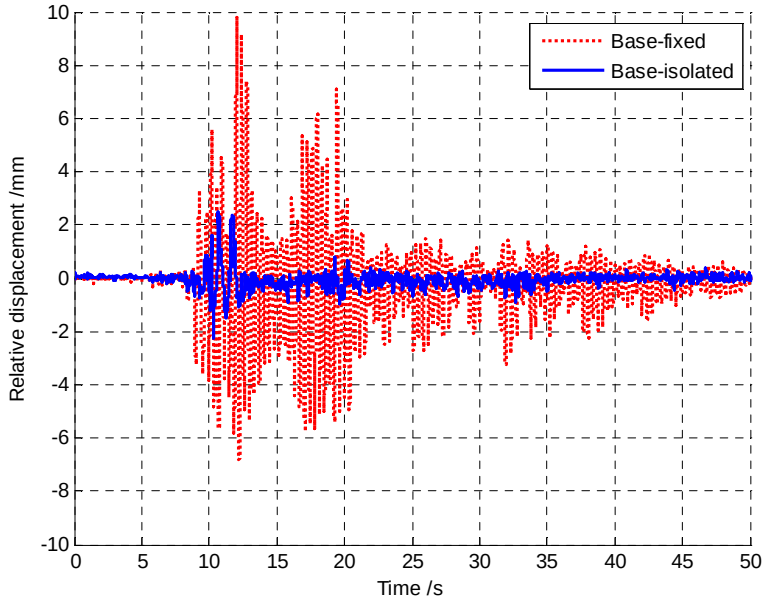


**Figure 5-25: Relative displacement between 2nd floor and base comparison under El Centro 0.1g earthquake.**

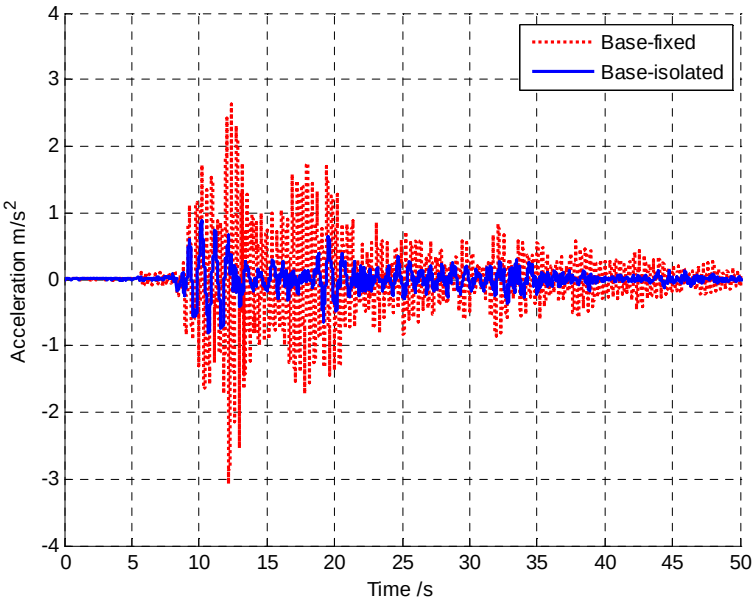


**Figure 5-26: 2nd floor acceleration comparison under El Centro 0.1g earthquake.**

With the same strength level, the Kobe earthquakes have the most vibration response among these four types of earthquakes. The acceleration of the Kobe earthquake at PGA of 0.1g is shown in Figure 5-27. Similarly, Figure 5-28 and Figure 5-29 show the comparisons under the Kobe 0.1g earthquake.

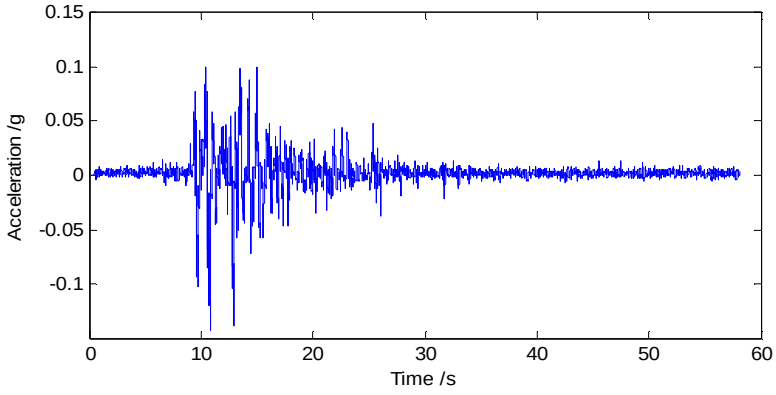


**Figure 5-27: Plot of Kobe earthquake in acceleration.**

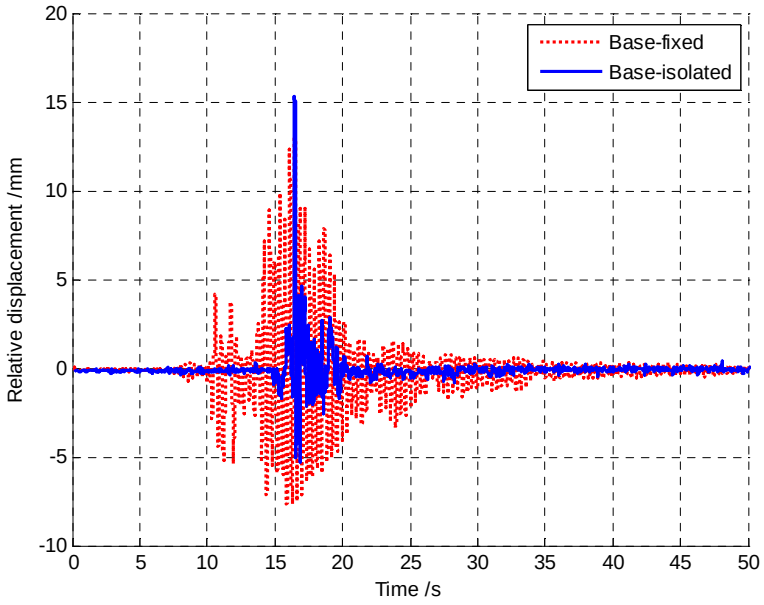


**Figure 5-28: Relative displacement between 2nd floor and base comparison under Kobe 0.1g earthquake.**

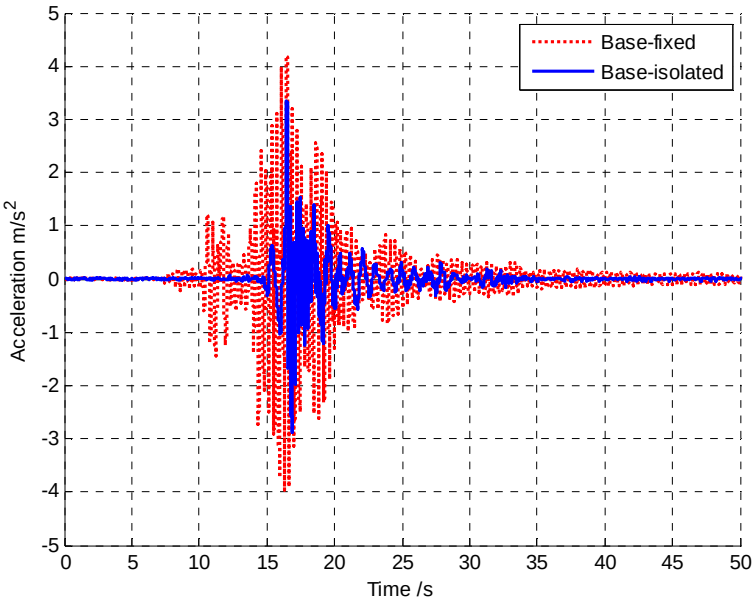


**Figure 5-29: 2nd floor acceleration comparison under Kobe 0.1g earthquake.**

Relatively, the North Ridge earthquake is the mildest one. The acceleration of the North Ridge earthquake in 0.1g is shown in Figure 5-30. The corresponding comparisons of structural performance are shown in Figure 5-31 and Figure 5-32.

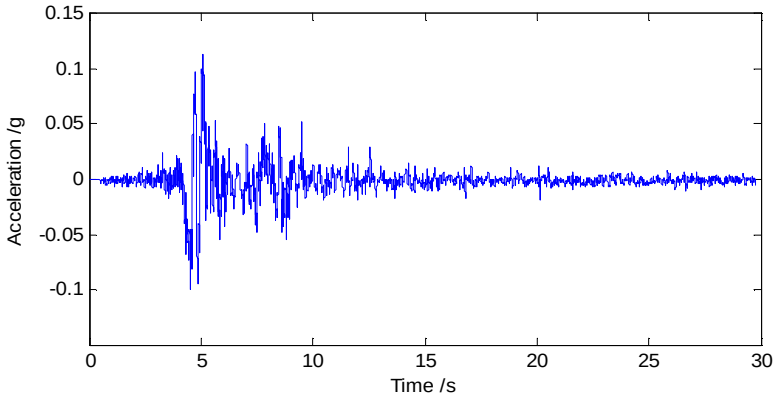


**Figure 5-30: Plot of North Ridge earthquake in acceleration.**

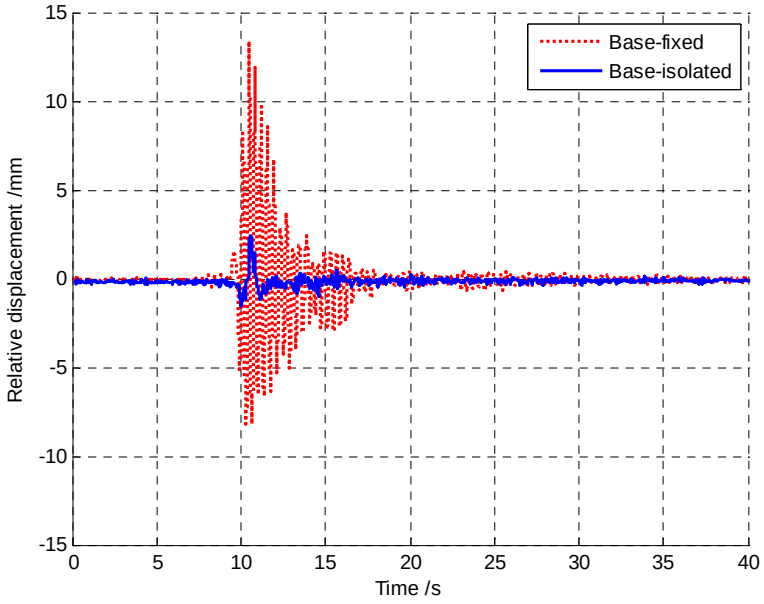


**Figure 5-31: Relative displacement between 2nd floor and base comparison under North Ridge 0.1g earthquake.**

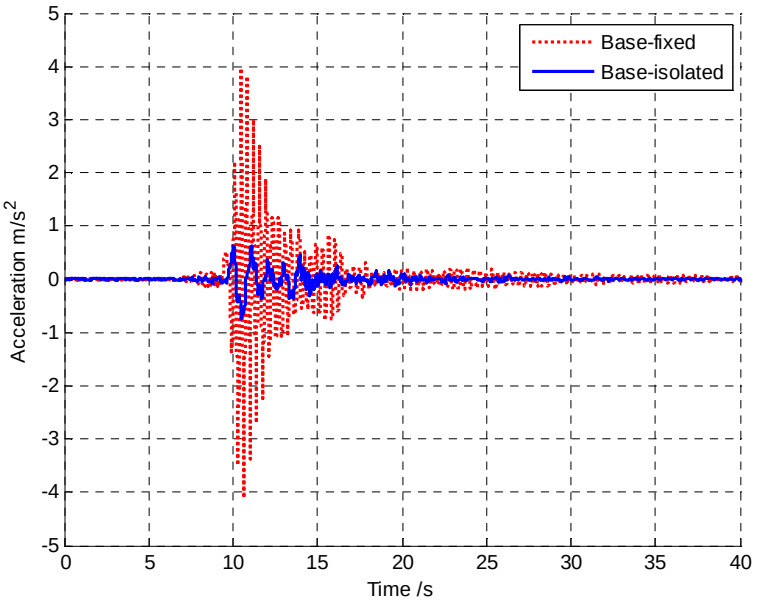


**Figure 5-32: 2nd floor acceleration comparison under North Ridge 0.1g earthquake.**

The Hachinohe earthquake is the shortest one in time comparing to the other three. The acceleration of the Hachinohe earthquake in 0.1g is shown in Figure 5-33. Figure 5-34 and Figure 5-35 show the comparisons under the Hachinohe 0.1g earthquake.

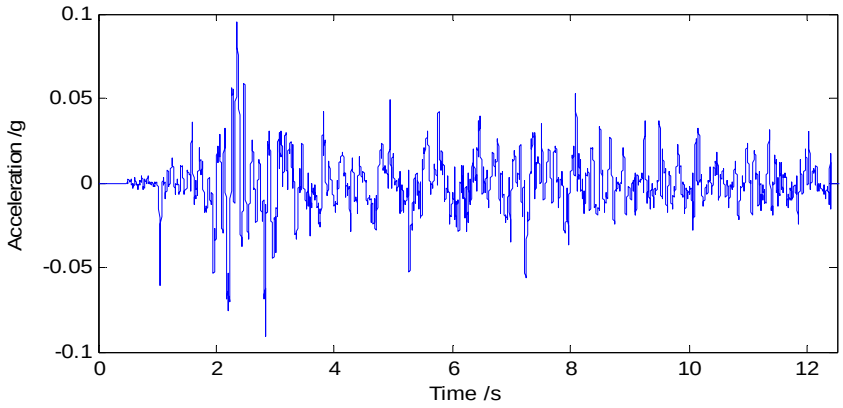


**Figure 5-33: Plot of Hachinohe earthquake in acceleration.**

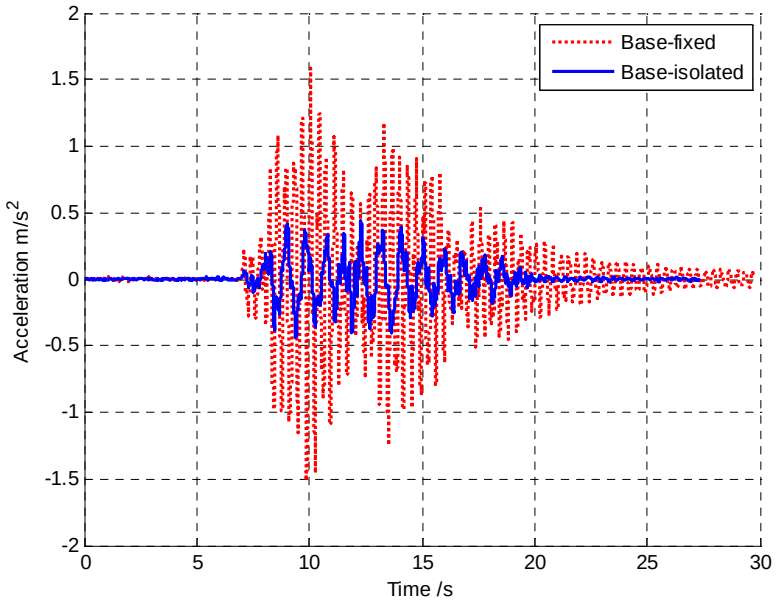


**Figure 5-34: Relative displacement between 2nd floor and base comparison under Hachinohe 0.1g earthquake.**

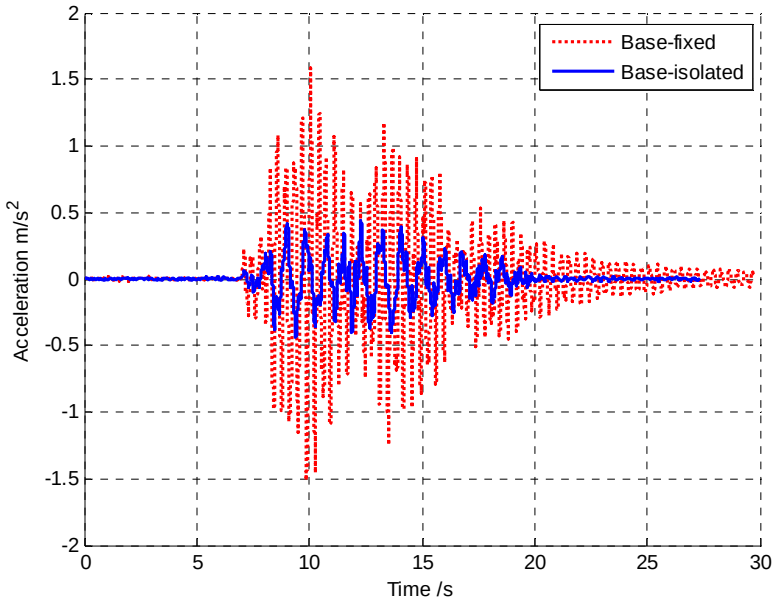


**Figure 5-35: 2nd floor acceleration comparison under Hachinohe 0.1g earthquake.**

In the above figures, the solid blue curve stands for the base-fixed structure, and the dash red curve stands for the base-isolated structure with superelastic SMA springs. For all the applied earthquakes, the energy of the structural vibration dissipates dramatically faster in the base-isolated structure with SMA springs than the base-fixed structure. For most of the applied earthquakes, the maximum amplitude of the structural performance in base-fixed structure is much higher than the base-isolated structure except the relative displacement under Kobe 0.1g earthquake, which was led by extensive base movement. Thus, for earthquakes dominant in a high frequency range, superelastic SMA springs with higher stiffness should be trained for those applications.

The summary of the experimental comparison results can be found in Table 5-4. In the table, "Max. rela-dis" stands for the maximum relative displacement between the $2^{nd}$ floor and the base, and "Max. acc-$2^{nd}$ " stands for the maximum $2^{nd}$ floor acceleration.

**Table 5-4: Summary of base isolation system with superelastic SMA springs**

| **Earthquake** | **Structural Performance Comparison** | **Base-fixed structure** | **Base-isolated structure with SMA springs** |
|---|---|---|---|
| El Centro 0.1g | Max. rela-dis | 10.0441mm | **2.7187mm** |
| | Max. acc-$2^{nd}$ | 3.0695m/$s^2$ | **0.8762m/$s^2$** |
| Kobe 0.1g | Max. rela-dis | **13.1782mm** | 15.5170mm |
| | Max. acc-$2^{nd}$ | 4.1913m/$s^2$ | **3.3557m/$s^2$** |
| North Ridge 0.1g | Max. rela-dis | 4.3138mm | **1.0003mm** |
| | Max. acc-$2^{nd}$ | 4.1093m/$s^2$ | **0.7454m/$s^2$** |
| Hachinohe 0.1g | Max. rela-dis | 13.4794mm | **2.6838mm** |
| | Max. acc-$2^{nd}$ | 1.5822m/$s^2$ | **0.4419m/$s^2$** |

As mentioned before, the base-isolated structure outperforms the base-fixed structure significantly for most of earthquakes. For the Kobe earthquake, the nature of the earthquake causes ground movements with excessive amplitude at low frequency, which may lead to the resonance of the base isolation system using springs with low stiffness. Using helical superelastic SMA springs with higher stiffness may solve this problem.

## 5.5 Summary

This chapter introduced an approach to train superelastic SMA helical springs and analyzed their hysteresis behaviors. More importantly, a new type of phenomenological model for superelastic SMA helical springs was presented. The proposed model consists of a liner function for the extending part and an exponential function for the compression part. The experimental verification shows that it successfully simulated the hysteresis behavior of a self-trained superelastic SMA helical spring including behaviors in both major loops and minor loops. Furthermore, the superelastic SMA helical springs as well as the proposed model are applied to the experimental base-isolated structure as presented in this chapter to dissipate energy and restore position. The experimental result also validates the phenomenological model Comparative results under various types of earthquakes show that the superelastic SMA helical springs can dramatically reduce the relative displacement and the floor accelerations for most of earthquakes.

# Chapter 6. Passive Electromagnetic Damper Mathematical Modeling

This chapter introduces a new type of structural damper: passive electromagnetic (EM) damper based on Palomera's research (Palomera, 2005). A mathematical model of the prototype EM dampers is derived based on quasi-static electromagnetic theory with performances improved from the literature. Since the implementation of passive EM dampers in base isolation systems has not been studied, a numerical simulation of a base isolation system with a prototype EM damper is performed in this chapter. The numerical simulation results demonstrate that, with the prototype EM damper, the structural vibrations are dramatically reduced than the system without EM damper.

## 6.1 Introduction

A passive EM damper is an electromechanical device which can apply an opposing force to impart the movement with no requirement of external energy. In addition, a well-designed EM damper may be able to generate small amount of electrical energy that could be possibly critical for emergent uses. For example, that energy could be stored and used as back-up power when a destructive earthquake may destroy the major power supply line of the building.

Similar to an electric generator, the EM damper converts kinetic energy into electric energy. However, an important difference should be noticed: the purpose of the damper is to reduce significantly, if not completely, the kinetic energy of the mover,

while the generator is to provide electrical energy to the devices in the electric circuit to which the generator is connected without detaining the mover.

In this chapter, a prototype tubular moving-magnet EM damper, as shown in Figure 6-1, is proposed and analyzed. The proposed prototype EM damper is operated based on the relative linear displacement of the mover (permanent magnet). The force-velocity relationship of the EM damper is similar to that of an ideal mechanical damper where the force $F_d$ is directly proportional to the applied velocity $v$ as

$$F_d = c_d v . \qquad \textbf{(Eqn. 6-1)}$$

where $c_d$ is the damping coefficient of the EM damper, which is determined by the geometric and electric properties of the device, and will be calculated in latter sections. The electrical equations are developed based on electromagnetic theory and Maxwell's equations, and the mechanical equations are based on Newton's laws (Woodson and Melcher, 1968).

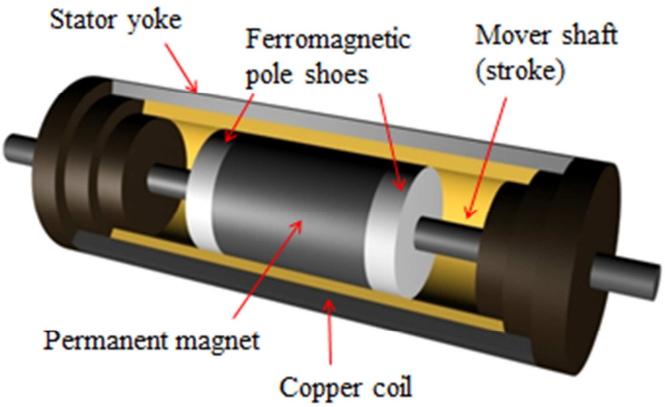


**Figure 6-1: The picture of the prototype tubular moving-magnet EM damper.**

In this prototype EM damper, the mover includes a single cylindrical permanent magnet with axial magnetization between two cylindrical ferromagnetic pole shoes. The length of the magnet equals the stroke of the damper. Ideally, the radius of the permanent magnet should be identical to the radius of the pole shoes. The armature of the EM damper is slot-less with a single phase winding over its length, which is made of two coils wound in opposite directions and connected in series. Both ends of the EM damper are made of non-magnetic materials to avoid magnetic leakages.

## 6.2 Electromagnetic Damper Model Derivation

In this section, the mathematical model will be derived to quantify the damping coefficient $c_d$ in (Eqn. 6-1) given the geometric and electric properties of the EM damper device. The purpose of this section is to express the damping force corresponding to an applied velocity. In order to derive its analytical model, the EM damper has to be assumed as follows:

1. Magnetic leakages will be neglected.
2. No magnetic saturation in the materials will be considered.
3. The magnetic field in the air gap is purely radial.
4. The magnetic field in the stator yoke and the permanent magnet are purely axial.

The geometric properties of the EM damper are described in Table 6-1.

**Table 6-1: EM damper geometric properties**

| Name | Symbol | Description |
|---|---|---|
| Mover radius | $r_m$ | Radius of the permanent magnet or the pole shoes. |
| Armature radius | $r_a$ | Radius of the inside of the armature. |
| Yoke radius | $r_y$ | Radius of the inside of the stator yoke. |
| Damper radius | $r_d$ | Radius of the EM damper. |
| Yoke thickness | $t_y$ | Thickness of the armature shell. $t_y = r_d - r_y$. |
| Coil thickness | $t_w$ | Thickness of the coils in the armature. $t_w = r_y - r_a$. |
| Air gap thickness | $t_a$ | Distance between the mover and the armature |
| Wire radius | $r_w$ | Radius of the coil wire cross-section. |
| Coil turns | $N_w$ | Total number of turns on each coil. |
| Active coil turns | $N_a$ | Active number of turns intercepted by the pole shoe flux. |
| Number of coils | $p$ | Number of coils (poles) per phase. |
| Pole shoe length | $l_p$ | Length of the pole shoes. |
| Magnet length | $l_m$ | Length of the permanent magnet. |
| Coil width | $l_w$ | Width of each coil in the armature. |

The half-section dimensional diagram of the prototype EM damper is presented in Figure 6-2.

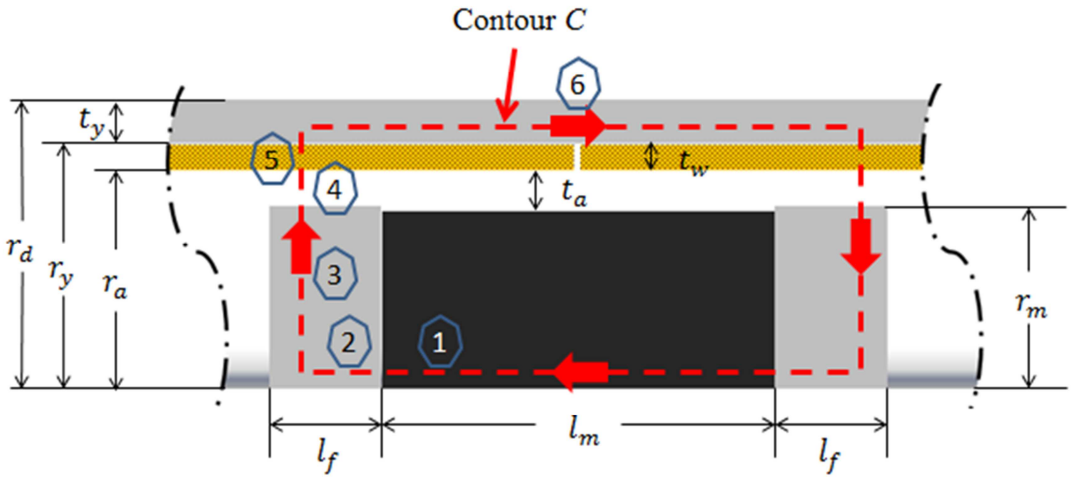


**Figure 6-2: Half-section diagram of the prototype EM damper showing dimension and analysis integration path.**

### 6.2.1 EM damper operating point

To calculate the permanent magnet operating point, Ampere's law shall be first applied. Ampere's law states that the line integral of a magnetic field intensity $\vec{H}$ around a closed contour $C$ equals the net current passing through the surface $S$ enclosed by said contour (Owen, 2003). The integral form of Ampere's law is

$$\oint_C \vec{H} \cdot d\vec{l} = \int_S \vec{J} \cdot d\vec{s}\,, \qquad \textbf{(Eqn. 6-2)}$$

where $\vec{J}$ is the current density.

Assume the magnetic field $\vec{H}$ is parallel to $d\vec{l}$, which follows the direction of contour $C$ as shown in Figure 6-2, since no magnetic leakages will be considered, (Eqn. 6-2) gives

$$\oint_C \vec{H} \cdot d\vec{l} = \int_1 \vec{H}_m \cdot d\vec{l} + 2\int_2 \vec{H}_{p2} \cdot d\vec{l} + 2\int_3 \vec{H}_{p3} \cdot d\vec{l} + 2\int_4 \vec{H}_g \cdot d\vec{l} + 2\int_5 \vec{H}_c \cdot d\vec{l} + \int_6 \vec{H}_s \cdot d\vec{l} = \int \vec{J} \cdot d\vec{s} = 0 \qquad \textbf{(Eqn. 6-3)}$$

,

where $\vec{H}_m$, $\vec{H}_{p2}$, $\vec{H}_{p3}$, $\vec{H}_g$, $\vec{H}_c$ and $\vec{H}_s$ are the magnetic field in the permanent magnet, the pole shoe of horizontal direction, the pole shoe of vertical direction, the air gap, the coil layer and the stator yoke shell, respectively. Number 1 through 6 indicate certain ranges within the integral contour $C$.

Without the consideration of magnetic saturation in the materials, the magnetic field $H$ and the magnetic flux density $B$ outside the permanent magnet are related by

$$H = \frac{B}{\mu_0 \mu_r}, \qquad \textbf{(Eqn. 6-4)}$$

where $\mu_0 = 4\pi \times 10^{-7}$ H/m is the permeability of free space, and $\mu_r$ is the relative permeability of the soft ferromagnetic material with a value typically much greater than unity. For non-magnetic materials, set $\mu = \mu_0$ for practical purposes; for permanent magnets (hard ferromagnetic materials), the permeability should not be a constant but a function of the magnetic field intensity $\vec{H}$. Also, since the permeability of copper is similar to that of air, the effective air gap is the thickness of both the actual air gap and the copper coil.

Moreover, the magnetic flux continuity condition must be satisfied. This condition states that no net magnetic flux emanates from a given space, which mathematically can be expressed as

$$\oint_S \vec{B} \cdot d\vec{s} = 0, \qquad \textbf{(Eqn. 6-5)}$$

where $d\vec{s}$ is perpendicular to the enclosed surface $S$.

Thus, as shown in Figure 6-1, the horizontal magnetic flux density $\vec{B}_{p2}$ in the pole shoes can be determined by applying the continuity condition to an enclosed

surface 1. The enclosed surface creates the surface $A_{p2}$ and $A_m$ perpendicular to the magnetic field $\vec{B}_m$ and $\vec{B}_{p2}$, and thus,

$$\oint_{S_1} \vec{B} \cdot d\vec{s} = B_m A_m - B_{p2} A_{p2} = 0 \Rightarrow B_{p2} = B_m \cdot \frac{A_m}{A_{p2}} = B_m . \quad \textbf{(Eqn. 6-6)}$$

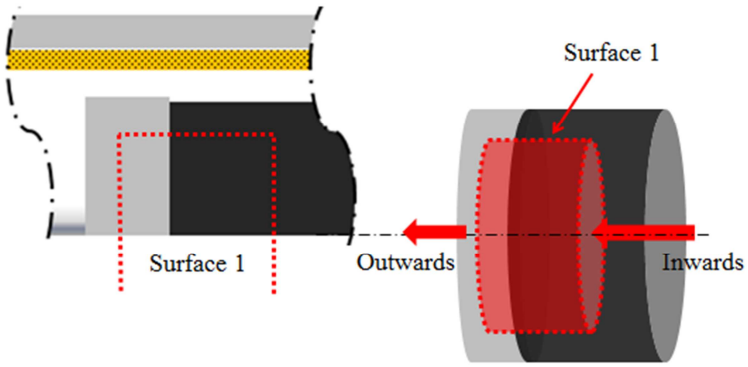


**Figure 6-3: Enclosed surface 1 in the prototype EM damper.**

By applying above conditions and substituting (Eqn. 6-4) and (Eqn. 6-6) into (Eqn. 6-3),

$$\oint_C \vec{H} \cdot d\vec{l} = H_m l_m + 2\int_0^{l_p} \frac{B_m}{\mu_0 \mu_{Fe}} dl + 2\int_0^{r_m} \frac{B_{p3}}{\mu_0 \mu_{Fe}} dr + 2\int_{r_m}^{r_y} \frac{B_g}{\mu_0} dr + \frac{B_s}{\mu_0 \mu_{Fe}} (l_m + 2l_p) = 0 \quad \textbf{(Eqn. 6-7)}$$

,

where $\mu_{Fe}$ is the relative permeability of iron used for the pole shoes and the stator shell.

To find the vertical magnetic flux density $\vec{B}_{p3}$ in the pole shoes, an enclosed cylindrical surface with a radius of $r$, as shown in Figure 6-4, should be applied.

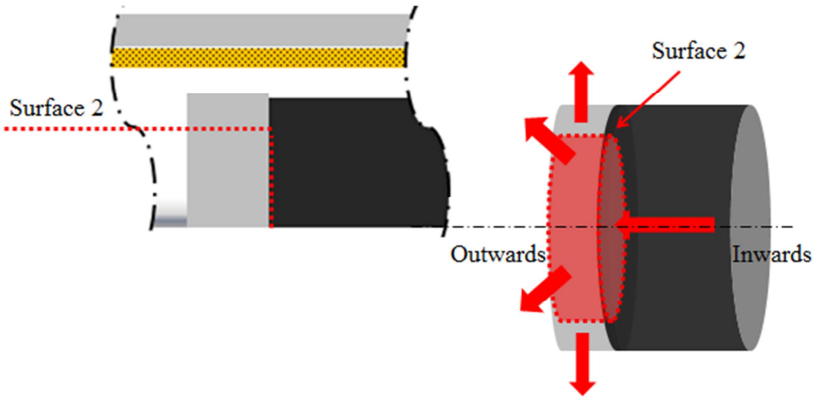


**Figure 6-4: Enclosed surface 2 in the prototype EM damper.**

Because of the continuity condition in (Eqn. 6-5), the magnetic flux going inwards should be equal to the magnetic flux going outwards, and thus

$$B_m A_m - B_{p3} A_{p3} = 0 \Rightarrow B_{p3} = \frac{\pi r^2 B_m}{2\pi r l_p} = \frac{r B_m}{2 l_p}, 0 \le r \le r_m \quad \textbf{(Eqn. 6-8)}$$

Similarly, the air gap flux density is determined using the cylindrical surface of radius $r$ partially enclosing the permanent magnet as shown in Figure 6-5. This surface intercepts the magnet and the gap fields perpendicularly; therefore, the air gap flux density $B_g$ is given by

$$B_m A_m - B_g A_g = 0 \Rightarrow B_g = \frac{r_m^2 B_m}{2 l_p r}, r_m \le r \le r_y \quad \textbf{(Eqn. 6-9)}$$

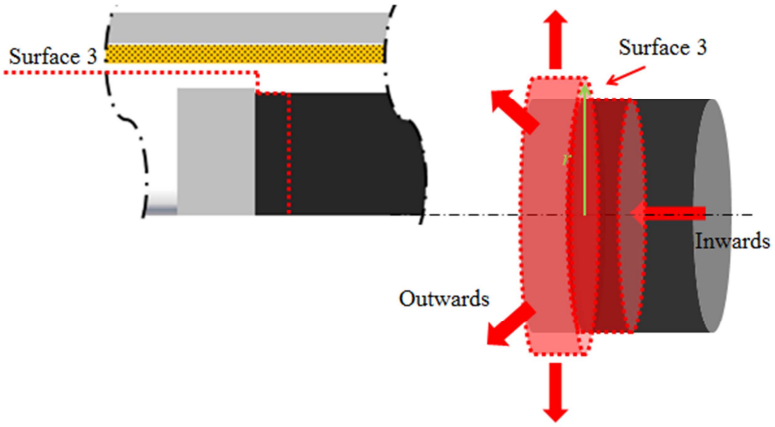


**Figure 6-5: Enclosed surface 3 in the prototype EM damper.**

Finally, as shown in Figure 6-6, using the cross-section 1 which creates the cross-sectional area $A_m$ and $A_s$ perpendicular to the magnetic field $\vec{B}_m$ and $\vec{B}_s$, respectively, the flux density in the stator shell $B_s$ is given by

$$B_m A_m - B_s A_s = 0 \Rightarrow B_s = \frac{r_m^2 B_m}{t_y (r_y + r_d)}. \qquad \textbf{(Eqn. 6-10)}$$

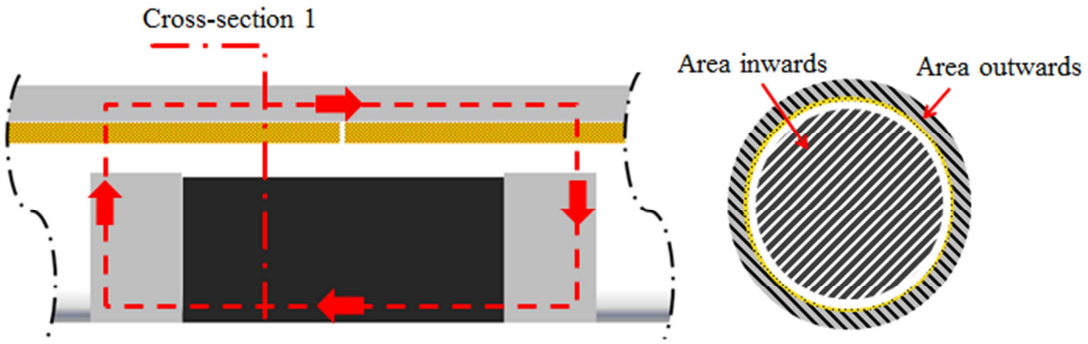


**Figure 6-6: Cross-section 1 in the prototype EM damper.**

Substituting (Eqn. 6-8) thru (Eqn. 6-10) into (Eqn. 6-7) results in

$$H_m = -\frac{r_m^2 B_m}{\mu_0 \mu_{Fe} l_p l_m}\left( \ln(\frac{r_y}{r_m})\mu_{Fe} + \frac{(l_m + 2l_p)l_p}{t_y (r_y + r_d)} + \frac{2l_p^2}{r_m^2} + \frac{1}{2} \right). \qquad \textbf{(Eqn. 6-11)}$$

For permanent magnets, the relationship between the flux density $B$ and the field intensity $B$ is typically represented by a hysteresis as shown in Figure 6-7. The first quadrant shows the initial magnetization of the permanent magnet, and the second quadrant, known as the demagnetization curve, represents the region in which the magnet is typically operating.

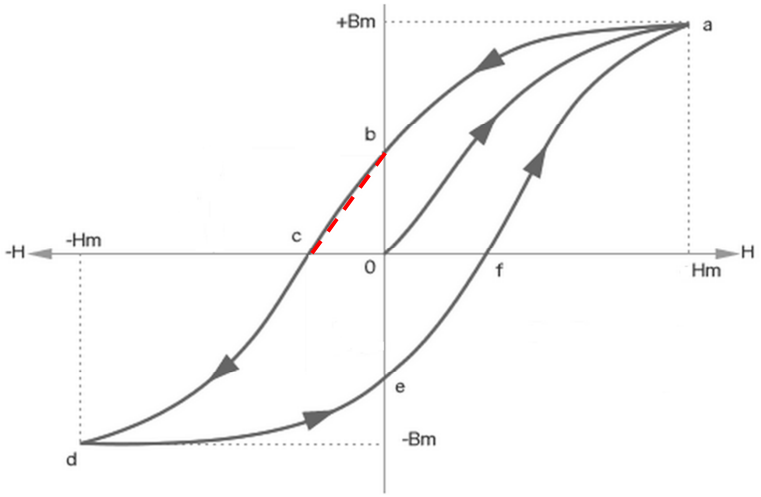


**Figure 6-7: Typical flux density to field intensity relationship for permanent magnet materials.**

Two major points in the demagnetization curve are of interest in this dissertation: point b representing the remanence induction $B_r$ and point c representing the coercivity force $H_c$. To simplify the analytical estimation, a straight line connecting the two points, as shown in Figure 6-7, usually approximates the demagnetization curve as

$$B_m = B_r + \mu_{rec} H_m, \qquad \textbf{(Eqn. 6-12)}$$

where $\mu_{rec} = \dfrac{B_r}{H_c}$ is the recoil permeability.

Substituting (Eqn. 6-11) into (Eqn. 6-12) gives

$$B_m = \frac{B_r l_m l_p \mu_0 \mu_{Fe}}{l_m l_p \mu_0 \mu_{Fe} + r_m^2 \mu_{rec} (\ln(\frac{r_y}{r_m}) \mu_{Fe} + \frac{2l_p^2}{r_m^2} + \frac{(l_m + 2l_p) l_p}{t_y (r_y + r_d)} + \frac{1}{2})}. \quad \textbf{(Eqn. 6-13)}$$

The above equations define the operating point of the permanent magnet in the EM damper modeling.

### 6.2.2 EM damper machine force

Next step is to find the damping coefficient of the EM damper. The Lorentz's law, which quantifies the force $\vec{F}$ acting in a moving current $i$ at a given velocity in the presence of a magnetic field $\vec{B}$, should be applied to calculate the force exerted on the mover. When the current moves along the direction $d\vec{l}$, the Lorentz's law gives

$$\vec{F} = \oint i d\vec{l} \times \vec{B}. \quad \textbf{(Eqn. 6-14)}$$

The current in the coil induces a magnetic flux perpendicular to the air gap flux produced by the permanent magnet in the EM damper. If the effect of the induced field on the air gap field is neglected, let $pN_a$ be the total number of active coil turns, which is the number of turns intercepting the magnetic flux at any time, and then the damping force is given by

$$F_d = pN_a \oint i d\vec{l} \times \vec{B}_g, \quad \textbf{(Eqn. 6-15)}$$

where $d\vec{l}$ is the direction tangential to the coil, and $\vec{B}_g$ is the magnetic flux density perpendicular to the coils and through the coils in radial direction. Substituting (Eqn. 6-9) into (Eqn. 6-15) yields

$$F_d = \frac{pN_a \pi r_m^2 B_m}{l_p} \cdot i_{cir} = K_{t,f} i_{cir}. \quad \textbf{(Eqn. 6-16)}$$

where $K_{t,f} = \frac{pN_a \pi r_m^2 B_m}{l_p}$ is the force constant of the EM damper device with the unit of [N/A]. Therefore, the damping force of a passive EM damper is determined by the current of the electric circuit, which is caused by the voltage induced by the translation of the mover.

### 6.2.3 EM damper open circuit induced voltage

To derive the induced voltage or the electromotive force on the coil due to the mover translation, consider the cylindrical surface of the coil as a flatten surface. The air gap magnetic flux is perpendicular to the coil surface and the mover translation.

Faraday's Law should be applied, which states that an electric filed $\vec{E}$ can be generated by a time varying magnetic field $\vec{B}$ (Woodson 1968). The derivation of the damper equation uses the integral form of the relationship as

$$\oint_C \vec{E} \cdot d\vec{l} = -\int_S \frac{\partial \vec{B}}{\partial t} \cdot d\vec{s}\,, \qquad \textbf{(Eqn. 6-17)}$$

where $S$ is the surface enclosed by the contour $C$, $d\vec{l}$ is parallel to the contour, and $d\vec{s}$ is perpendicular to the surface.

Since the EM damper is under open circuit condition (i.e. $i_{cir} = 0$), assuming the moving distance of the mover is $x$, and the right side of (Eqn. 6-17) yields

$$-\int_S \frac{\partial}{\partial} \vec{B} \cdot d\vec{s} = -\frac{\partial}{\partial t}(B_g \cdot 2\pi r x) = -2\pi r B_g \cdot v\,, \qquad \textbf{(Eqn. 6-18)}$$

where $v$ is the relative velocity between the translator and the mover.

To achieve the left side of (Eqn. 6-17), the voltage between the open ends of the coils should be calculated as

$$\oint_C \vec{E} \cdot d\vec{l} = -V_{turn} + R_{coil} i_{cir} = -V_{turn}, \quad \textbf{(Eqn. 6-19)}$$

where $V_{turn}$ is the open circuit voltage for one turn of coil.

Thus,

$$V_{turn} = -2\pi r B_g v . \quad \textbf{(Eqn. 6-20)}$$

Substituting (Eqn. 6-9) into (Eqn. 6-20) and considering $pN_a$ turns connected in series that are linked by the air gap magnetic flux, the total open circuit voltage induced in the EM damper $V_{emf}$ is given by

$$V_{emf} = \frac{pN_a \pi r_m^2 B_m}{l_p} v = K_{t,e} v, \quad \textbf{(Eqn. 6-21)}$$

where the term $K_{t,e} = \frac{pN_a \pi r_m^2 B_m}{l_p}$ is known as the electromotive force constant (emf) of the EM damper device. Note that, for the EM damper, the electromotive force constant $K_{t,e}$ has the same numerical value with the force constant $K_{t,f}$, and their units (N/A and Vs/m) are dimensionally equivalent. However, in practice, the measured emf constants and force constants may be different due to losses that have not been taking accounted for the modeling.

Therefore, in this dissertation, the EM damper damping coefficient $K_d$ is defined as $K_d = K_{t,f} = K_{t,e}$ for numerical simulations. By substituting (Eqn. 6-13) into (Eqn. 6-16) or (Eqn. 6-21), the damping coefficient can be expressed in terms of the geometric and magnetic properties of the device as below:

$$K_d = \frac{\pi r_m^2 p N_a B_{rem} (l_m + l_p)}{(l_m + l_p) l_p + r_m^2 \frac{2\mu_{rec}}{\mu_0} \left( \frac{\ln(\frac{r_y}{r_m})}{2} + \frac{1}{\mu_{Fe}} + \frac{(l_m + l_p) l_p}{\mu_{Fe} t_y (r_y + r_d)} + \frac{l_p^2}{r_m^2 \mu_{Fe}} \right)} \quad \textbf{(Eqn. 6-22)}$$

Combining with the electrical parameters (i.e. resistance and inductance), this coefficient will lead to the constitutive relationship between the force and the velocity of the EM damper.

### 6.2.4 EM damper resistance and inductance

Since the EM damper will be operated under closed circuit situations, the non-ideal parameters caused by the winding should be considered as essential factors. First, by the Ohm's Law, the coils will cause a slight voltage drop and dissipate energy, and thus, the resistance for the coils should be calculated. Second, an axial magnetic flux inside the coil will develop due to the non-zero current, and it will manifest itself as a circuit inductance. Also, the inductance will introduce a time delay between the induced emf voltage and the current, which is equivalent between the applied movement and the damping force.

The resistance of the coils can be simply calculated by adding the total amount of turns in the coil $N_w$ and the average radius of the coil. Consider the number of poles is $p$ and the coils are connected in series, the resistance of the coils is calculated as

$$R_{coil} = \frac{p N_w (r_y + r_a)}{r_w^2 \sigma}, \quad \textbf{(Eqn. 6-23)}$$

where $\sigma$ is the conductivity of the coil material.

The EM damper (coil) inductance is generally different when the relative position of the mover inside the winding varies. However, since we assumed the length

of the translator equals to the length of the coil and its relative movement should be constrained to avoid the edge of the winding, the inductance of the coil is assumed independent of its relative position, and thus approximated.

The self-inductance of the EM damper (coil) can be derived by using magnetic circuits or reluctance networks. Mutual inductance between the coils in the damper should be neglected for simplification. The magnetic flux due to the current in the coil is assumed axial, and the magnetic flux due to the permanent magnet is neglected. The total inductance of the EM damper is calculated by adding the inductance of each coil.

The inductance $L$ is defined as

$$L = \frac{\partial \Lambda}{\partial i}, \qquad \textbf{(Eqn. 6-24)}$$

where $\Lambda$ is the magnetic flux linkage and $i$ is the current in the coil wire. The flux linkage $\Lambda$ is defined as

$$\Lambda = \int_S \vec{B} \cdot dS . \qquad \textbf{(Eqn. 6-25)}$$

Thus, for a tightly wounded coil, $\Lambda$ can be calculated as

$$\Lambda = N\Phi , \qquad \textbf{(Eqn. 6-26)}$$

where $\Phi$ is the magnetic flux through each of the $N$ coils. The magnetomotive force $F$ in an inductor or electromagnet consisting of a coil of wire is given by

$$F = Ni . \qquad \textbf{(Eqn. 6-27)}$$

Also, the Hopkinson's law gives

$$F = \Phi \Re = Ni , \qquad \textbf{(Eqn. 6-28)}$$

where $\Re$ is the reluctance of the circuit. Substituting (Eqn. 6-26) and (Eqn. 6-28) into (Eqn. 6-24) gives the inductance of the coil in terms of the reluctance as

$$L = \frac{N^2}{\Re}. \qquad \textbf{(Eqn. 6-29)}$$

Figure 6-8 shows a schematic diagram of the prototype electromagnetic damper with two poles. Based on the structure, the equivalent reluctance network can be found in Figure 6-9, which is simply a series circuit of reluctance.

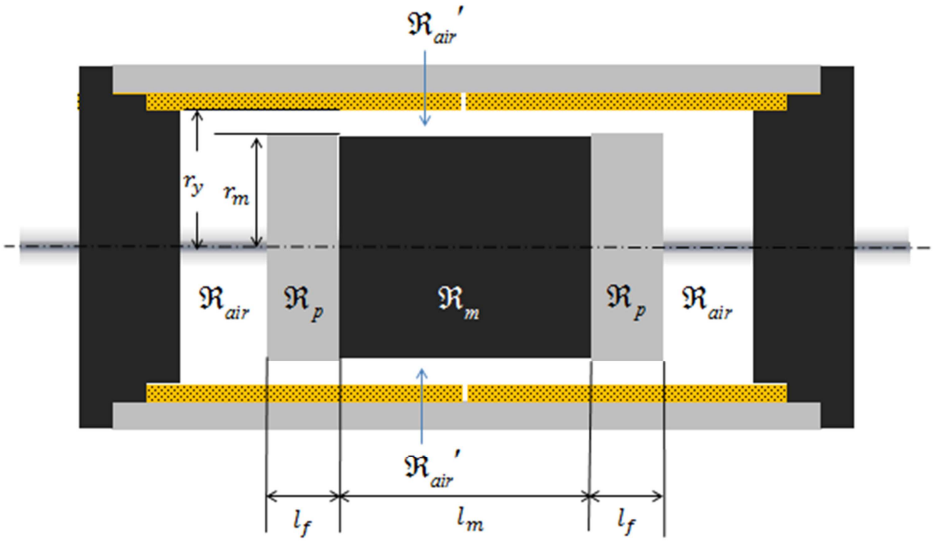


**Figure 6-8: EM damper schematic diagram.**

The reluctance of a component can be computed by

$$\Re = \int \frac{dl}{\mu A}, \qquad \textbf{(Eqn. 6-30)}$$

where $l$ is the length, $A$ is the cross-sectional area and $\mu$ is the permeability of the component.

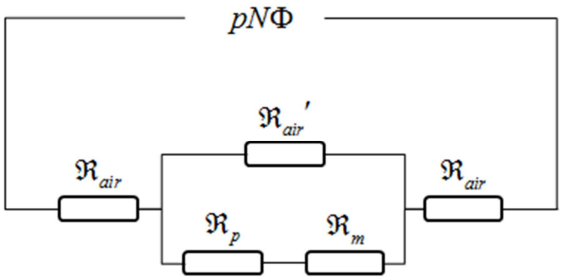


**Figure 6-9: EM damper reluctance network diagram.**

By using (Eqn. 6-30), the reluctances of $\Re_{air}, \Re_p, \Re_m$ and $\Re_{air}'$ as shown in Figure 6-9 can be calculated as

$$\Re_{air} = \frac{2l_w - 2l_p - l_m}{\mu_0 \pi r_a^2}, \quad \textbf{(Eqn. 6-31)}$$

$$\Re_{air}' = \frac{l_m + 2l_p}{\mu_0 \pi (r_a^2 - r_m^2)}, \quad \textbf{(Eqn. 6-32)}$$

$$\Re_p = \frac{2l_p}{\mu_0 \mu_{Fe} \pi r_m^2}, \quad \textbf{(Eqn. 6-33)}$$

$$\Re_m = \frac{l_m}{\mu_0 \mu_m \pi r_m^2}. \quad \textbf{(Eqn. 6-34)}$$

Based on Figure 6-9, the total reluctance of the EM damper is

$$\Re_{total} = \Re_{air} + \frac{1}{1/\Re_{air}' + 1/(\Re_p + \Re_m)}. \quad \textbf{(Eqn. 6-35)}$$

Thus, substituting (Eqn. 6-31) through (Eqn. 6-34) into (Eqn. 6-35) yields

$$\Re_{total} = \frac{1}{\mu_0 \pi}\left[\frac{2l_w - 2l_p - l_m}{r_a^2} + \frac{1}{\frac{\mu_{Fe} r_m^2}{2l_p + \mu_{Fe} l_m} + \frac{r_a^2 - r_m^2}{l_m + 2l_p}}\right]. \quad \textbf{(Eqn. 6-36)}$$

By substituting (Eqn. 6-36) into (Eqn. 6-29), the inductance of the coils is shown as

$$L_{coil} = \frac{\mu_0 \pi p N_w^2}{\frac{2l_w - 2l_p - l_m}{r_a^2} + 1/\left(\frac{\mu_{Fe} r_m^2}{2l_p + \mu_{Fe} l_m} + \frac{r_a^2 - r_m^2}{l_m + 2l_p}\right)}. \quad \textbf{(Eqn. 6-37)}$$

where the geometric parameters can be found in Table 6-1, $\mu_0$ is the permeability of free space equal to $4\pi e - 7$ henry/m and $\mu_{Fe}$ is the relative permeability of iron.

### 6.2.5 EM damper force-velocity model

Based on the relationships developed in the previous subsections, the damping force of an ideal EM damper can be calculated as

$$F_d = K_d i_{cir}, \quad \textbf{(Eqn. 6-38)}$$

and

$$e = K_d v, \quad \textbf{(Eqn. 6-39)}$$

where $i_{cir}$ is the current in the coils, $v$ is the relative velocity of the EM damper, and $K_d$ is the damping coefficient defined in (Eqn. 6-22). The above equations have coupled both the mechanical and electrical domains. Note that losses of mechanical origin, such as frictions, are neglected in the equations, but possibly included in the applications utilizing EM dampers.

If a load of a resistor $R_{load}$ is applied to the circuit, the relationship between the induced emf voltage $e$ and the circuit current $i_{cir}$ is

$$e = L_{coil} \frac{di_{cir}}{dt} + (R_{coil} + R_{load}) i_{cir}, \quad \textbf{(Eqn. 6-40)}$$

where $L_{coil}$ and $R_{coil}$ are the inductance and resistance of the coils as calculated in (Eqn. 6-37) and (Eqn. 6-23), respectively.

Substituting (Eqn. 6-38) and (Eqn. 6-39) into (Eqn. 6-40) yields

$$L_{coil}\frac{dF_d}{dt}+(R_{coil}+R_{load})F_d=K_d^2 v. \quad \textbf{(Eqn. 6-41)}$$

As shown above, the EM damper behaves as a linear mechanical component (damper). Normally, a time delay should be included in the modeling that it should be set by the damper coefficient and the electrical circuit components. Furthermore, the time delay will cause hysteresis for the force-velocity curve.

Thus, assume initial conditions are zero, and (Eqn. 6-41) can be simply converted into a transfer function with the input of velocity and the output of damping force as

$$\frac{F_d(s)}{v(s)}=\frac{K_d^2}{L_{coil}s+R_{coil}+R_{load}}e^{-t_d s}, \quad \textbf{(Eqn. 6-42)}$$

where $t_d$ is the time delay term.

## 6.3 Electromagnetic Damper Model Verification

In order to validate the modeling approach mentioned above, a tubular non-commutated moving magnet DC linear motor made by Baldor Motors and Drives™ (model number LMNM2-1F5-1F1), as shown in Figure 6-10, was used as a prototype electromagnetic damper in this section. The motor datasheet is supplied by the manufacture, and presented in Figure 6-11.

The geometric and material properties of the linear DC motor are shown in Table 6-2. Note that the pole shoes are consisted of two cylinders have slightly different diameters with the permanent magnet. In this modeling method, the difference will be neglected.

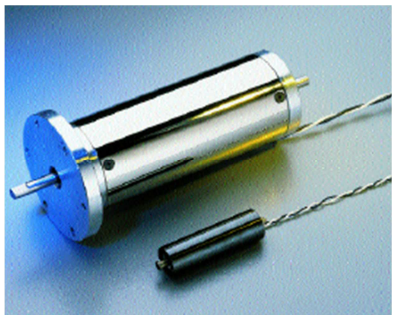

**Figure 6-10: DC linear motor from Baldor Motors and Drives (model number LMNM2-1F5-1F1).**

## Non-Commutated Moving Magnet Technical Data

| | | Catalog Number | | | |
|---|---|---|---|---|---|
| Parameters | Units | LMNM2-F8-F6 | LMNM2-1F3-F2 | LMNM2-1F5-F8 | LMNM2-1F5-1F1 |
| **General:** | | | | | |
| Stroke | in [mm] | 0.600 [15.2] | 0.250 [6.4] | 0.750 [19.1] | 1.125 [28.6] |
| Continuous Force | lbs [N] | 0.5 [3] | 1.9 [9] | 2.5 [12] | 2.5 [12] |
| Continuous Current | Amps | 0.87 | 1.02 | 0.86 | 1.47 |
| Peak Force@ 10% Duty | lbs [N] | 1.5 [7] | 5.7 [26] | 7.5 [34] | 7.5 [34] |
| Peak current @ 10% Duty | Amps | 2.6 | 3.1 | 2.6 | 4.4 |
| Continuous Power | Watts | 2 | 10 | 10 | 9 |
| **Mechanical:** | | | | | |
| No. of poles | | 2 | 2 | 2 | 2 |
| Motor moving weight | lbs [kg] | 0.050 [0.030] | 0.100 [0.050] | 0.313 [0.150] | 0.486 [0.230] |
| Motor total weight | lbs [kg] | 0.163 [0.080] | 0.800 [0.370] | 1.110 [0.510] | 1.280 [0.590] |
| Bearing Type | | Jewel Sapphire | Ball Bushing | Ball Bushing | Ball Bushing |
| **Electrical:** | | | | | |
| Force Constant Ph to Ph | lbs[N]/amps | 0.58 [2.6] | 1.87 [8.3] | 2.91 [13.0] | 1.70 [7.6] |
| Back EMF Constant Ph to Ph | V/in/s [V/m/s] | 0.07 [2.6] | 0.21 [8.3] | 0.33 [13.0] | 0.19 [7.6] |
| Resistance Ph to Ph at 25˚C | Ohms | 3.2 | 9.7 | 13.6 | 4 |
| Resistance Ph to Ph at 125˚C | Ohms | 4.5 | 13.5 | 2.7 | 5.6 |
| Inductance Ph to Ph | mH | 0.225 | 0.9 | 0.9 | 1.52 |
| Electrical Time Constant | msec | 0.070 | 0.093 | 0.066 | 0.380 |
| Km Motor Constant | lbs[N]/$\sqrt{W}$ | 0.32 [1.44] | 0.60 [2.67] | 0.79 [3.51] | 0.85 [3.78] |

**Figure 6-11: Datasheet of DC linear motor LMNM2-1F5-1F1.**

By applying the parameters in Table 6-2 into equations in the previous subsections, Table 6-3 presents the numerical comparison between the actual values of the DC linear motor and the theoretical model values of the EM damper. This includes the damping coefficient (force constant / emf constant), the coil resistance, and the coil inductance.

**Table 6-2: Geometric and material properties of LMNM2-1F5-1F1 linear DC motor**

| Name | Symbol | Value | Unit |
|---|---|---|---|
| Mover radius | $r_m$ | 13.34 | mm |
| Armature radius | $r_a$ | 13.82 | mm |
| Yoke radius | $r_y$ | 16.40 | mm |
| Damper radius | $r_d$ | 19.05 | mm |
| Yoke thickness | $t_y$ | 2.65 | mm |
| Coil thickness | $t_w$ | 2.58 | mm |
| Air gap thickness | $t_a$ | 0.48 | mm |
| Wire radius | $r_w$ | 28.65 | mm |
| Coil turns | $N_w$ | 250 | / |
| Number of coils | $p$ | 2 | / |
| Pole shoe length | $l_p$ | 24.9 | mm |
| Magnet length | $l_m$ | 39.1 | mm |
| Coercivity force | $H_c$ | 900 | kA/m |
| Remanence induction | $B_r$ | 1.2 | T |

**Table 6-3: Comparison of EM damper coefficients between mathematical model and experimental data**

| Parameters | Damping Coefficient (V/m/s) | Resistance (ohms) | Inductance (mH) |
|---|---|---|---|
| Model | 7.6368 | 1.5095 | 3.9979 |
| Experimental | 7.6 | 1.52 | 4 |
| Difference in % | 0.48% | −0.69% | −0.05% |

As shown in Table 6-3, the proposed mathematical model is a good representation of the EM damper device, as the mathematical values are within 1% of the experimental values.

## 6.4 Numerical Simulation of EM damper in Base Isolation System

The mathematical model is developed based on the experimental setup in the previous section. Figure 6-12 shows the diagram of a base-isolated structure with a prototype EM damper. Two identical regular steel springs are connected at both sides of the isolated base to provide restore force. The EM damper is used to limit the base movement, and springs are used to generate the restoring force.

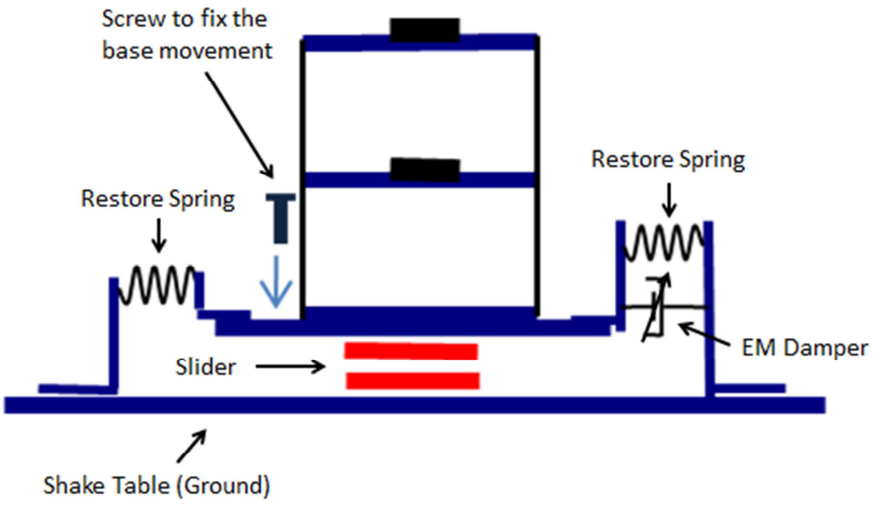


**Figure 6-12: Diagram of the base-isolated structural model with EM damper.**

Similar to (Eqn. 5-16), the system can be described as below:

$$M\ddot{X} + C\dot{X} + KX = -M\{1\}\ddot{x}_g + F\,, \qquad \textbf{(Eqn. 6-43)}$$

where $M$ is the mass matrix, $C$ is the damping matrix, $K$ is the stiffness matrix, $X$ is the displacement vector, which are all presented in 5.4, and $F$ is the external force input vector, as

$$F = \begin{Bmatrix} 0 \\ 0 \\ F_{EM} - F_f \operatorname{sgn}(\dot{x}_b) \end{Bmatrix}, \qquad \textbf{. (Eqn. 6-44)}$$

where $F_f$ is the friction force of slider, $F_{EM}$ is the damping force generated by the EM damper on one side of the structural model.

To obtain the state space model, let $\tilde{X} = \begin{bmatrix} X \\ \dot{X} \end{bmatrix}$, then

$$\dot{\tilde{X}} = \begin{bmatrix} 0 & I \\ -M^{-1}K & -M^{-1}C \end{bmatrix} \tilde{X} + \begin{bmatrix} 0 & 0 \\ -1 & M^{-1} \end{bmatrix} \begin{Bmatrix} \ddot{x}_g \\ F \end{Bmatrix}. \qquad \textbf{(Eqn. 6-45)}$$

Therefore, the mathematical base isolation model can be simulated using the equation above.

## 6.5 Numerical Simulation Results

Similar to 5.4, the relative displacement between the 2nd floor and the base and the 2nd floor acceleration are compared as the performance of the systems. To test the performance of the base isolation structure with EM damper, four different types of earthquakes at PGA of 0.1g are applied. The simulation results with comparisons for each earthquake can be found in the following subsections, and the summarized in Table 6-4 at the end of this section.

We compare the structural performance for three situations: the fixed structure without base isolation, the base isolation structure with EM damper, the base isolation structure without EM damper. As shown in Figure 6-13 and Figure 6-14, with help from the base isolation system and the EM damper, the vibration has been substantially suppressed. Also, the EM damper can dissipate the energy of the vibration much faster, and reduce the maximum base movement as shown in Figure 6-15.

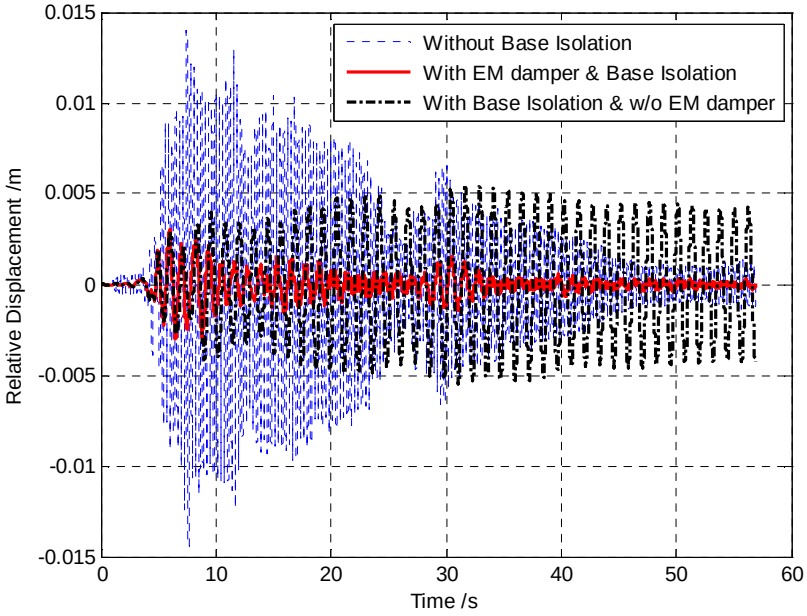


**Figure 6-13: Comparison of relative displacement under El Centro earthquake.**

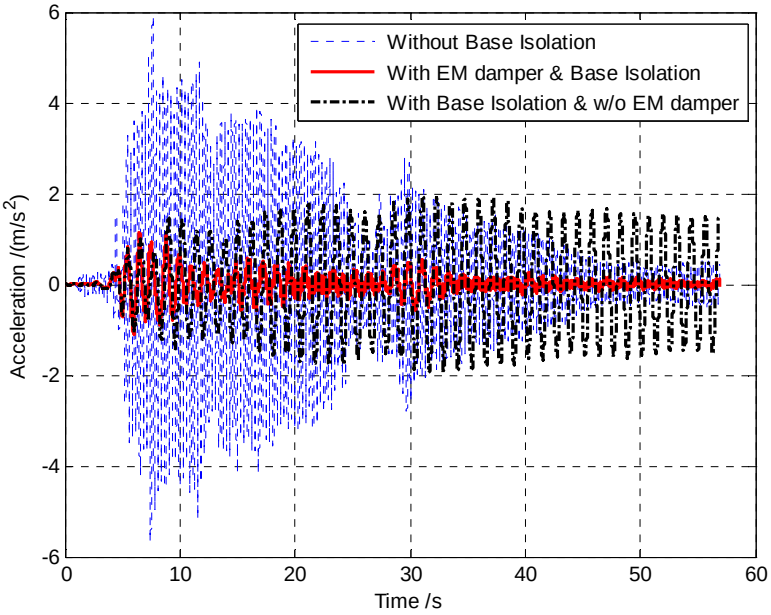


**Figure 6-14: Comparison of 2nd floor acceleration under El Centro Earthquake.**

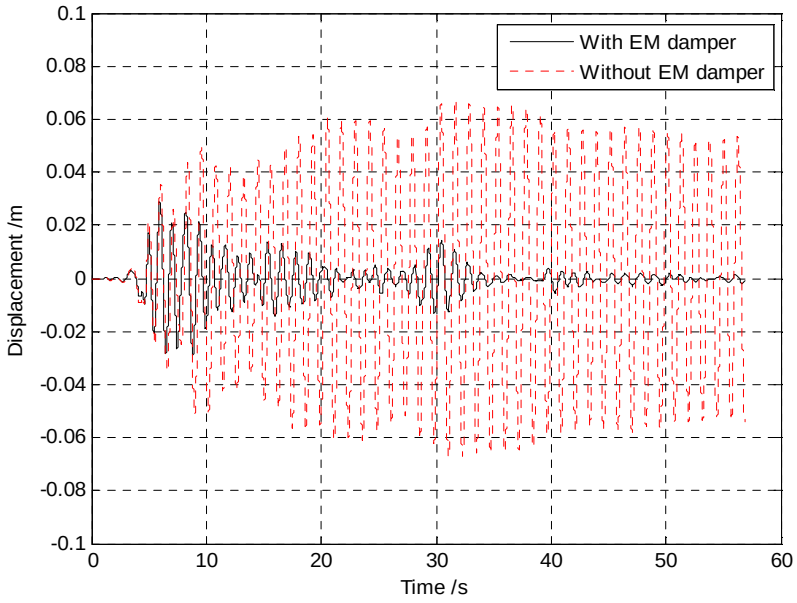


**Figure 6-15: Comparison of base displacement under El Centro Earthquake.**

Similar to the El Centro earthquake, in the Kobe earthquake, it is obvious that the base isolation structure can dramatically reduce the relative displacement and the 2nd floor acceleration as shown in Figure 6-16 and Figure 6-17. On the other hand, the EM damper can only slightly improve the structural performance of the relative displacement and the 2nd floor acceleration due to the powerful acceleration of the earthquake around 11s, but greatly reduce the vibration of the base as shown in Figure 6-18.

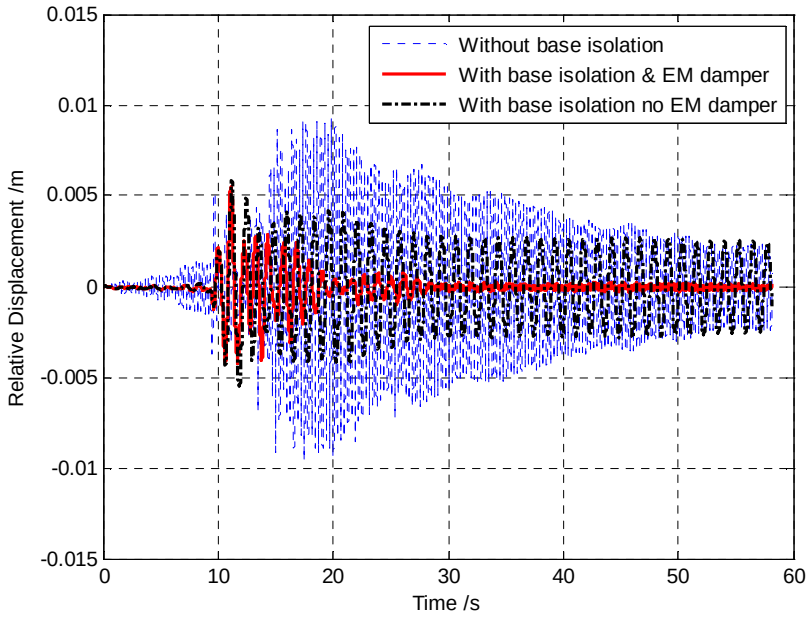


**Figure 6-16: Comparison of relative displacement under Kobe earthquake.**

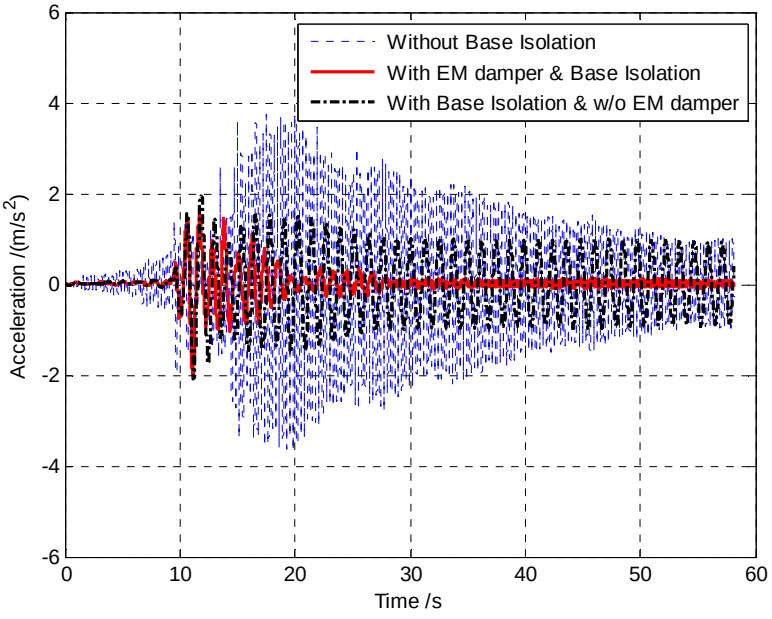


**Figure 6-17: Comparison of 2nd floor acceleration under Kobe Earthquake.**

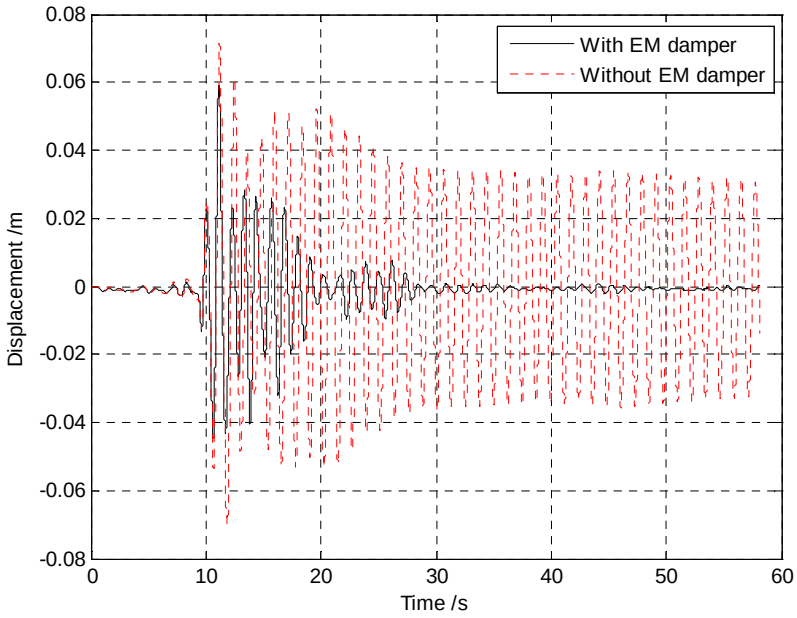


**Figure 6-18: Comparison of base displacement under Kobe Earthquake.**

Figure 6-19 and Figure 6-20 show the comparison of the relative displacement and the 2nd floor acceleration under the earthquake of Northridge 0.1g, respectively. Figure 6-21 shows the comparison of the base movement. As shown in the figures, the structural vibrations have been significantly reduced by introducing the base isolation system, and further improved with EM damper. At the meanwhile, the base movement is improved as well.

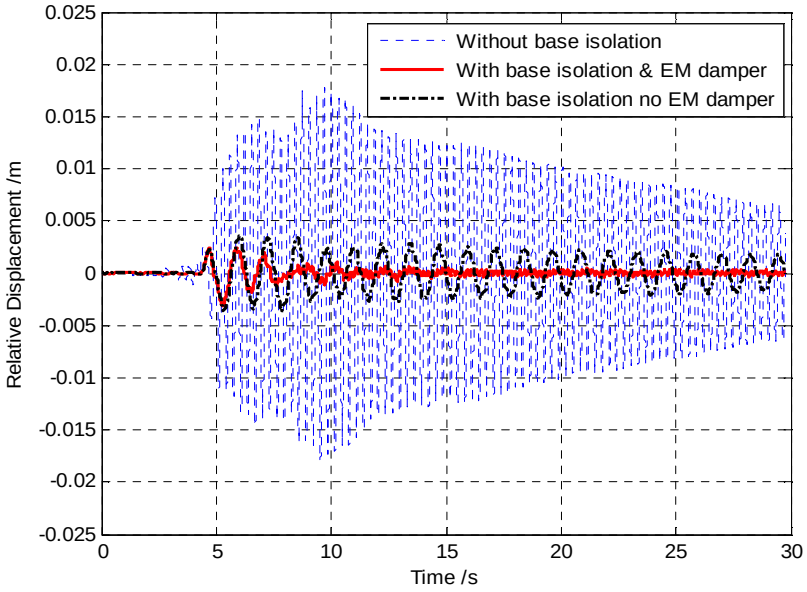


**Figure 6-19: Comparison of relative displacement under North Ridge earthquake.**

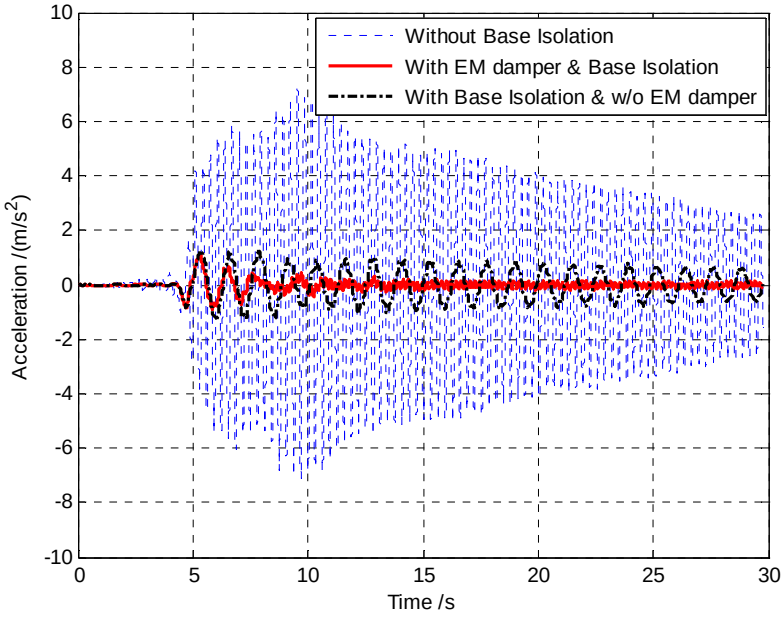


**Figure 6-20: Comparison of 2nd floor acceleration under North Ridge Earthquake.**

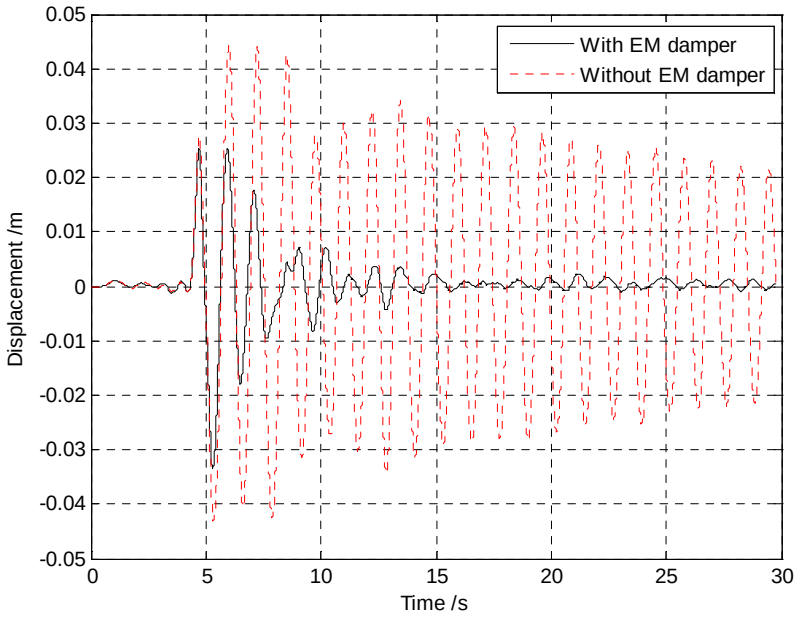


**Figure 6-21: Comparison of base displacement under North Ridge Earthquake.**

For the Hachinohe 0.1g earthquake, the relative displacement comparison can be found in Figure 6-22, and the 2nd floor acceleration comparison can be found in Figure 6-23. With the base isolation system, structural vibrations are barely visible comparing to the normal fixed structure. Figure 6-24 shows the base movement comparison under Hachinohe 0.1g earthquake. Since the Hachinohe earthquake does not cause a significant vibration, only minor differences can be observed between the base isolation system with and without EM damper.

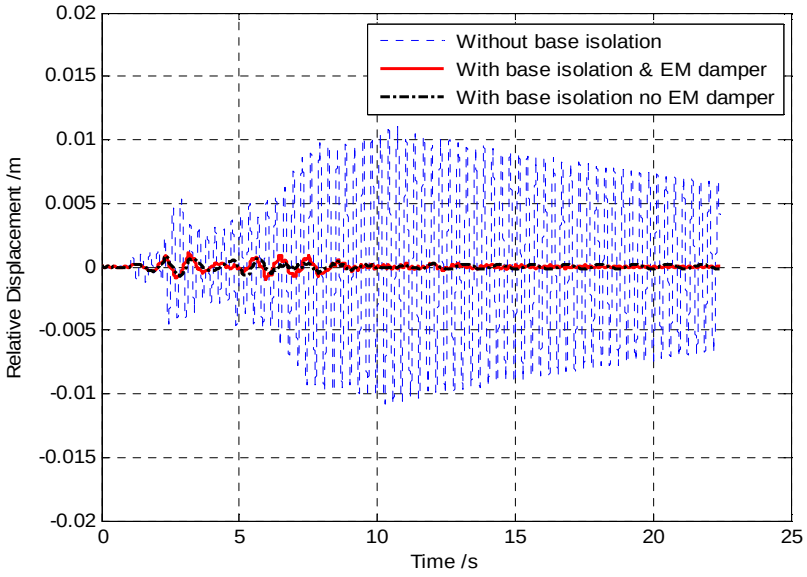


**Figure 6-22: Comparison of relative displacement under Hachinohe earthquake.**

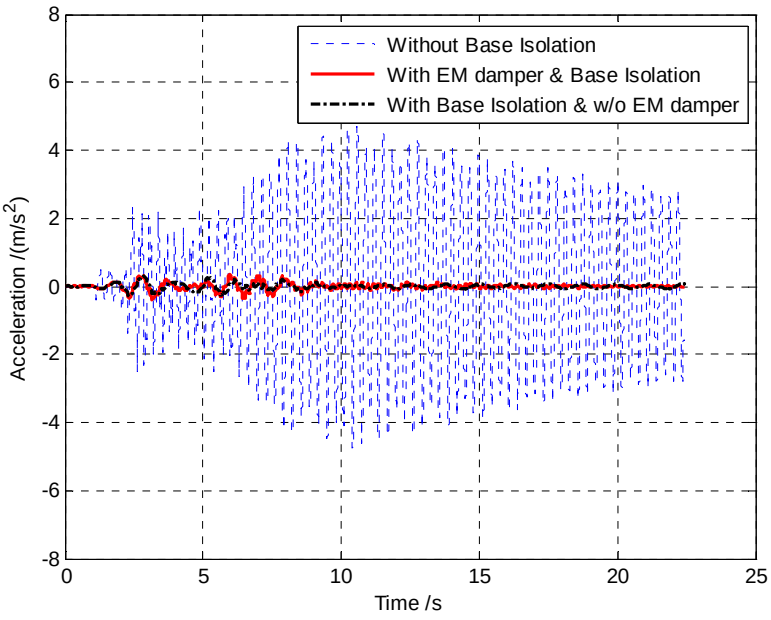


**Figure 6-23: Comparison of 2nd floor acceleration under Hachinohe Earthquake.**

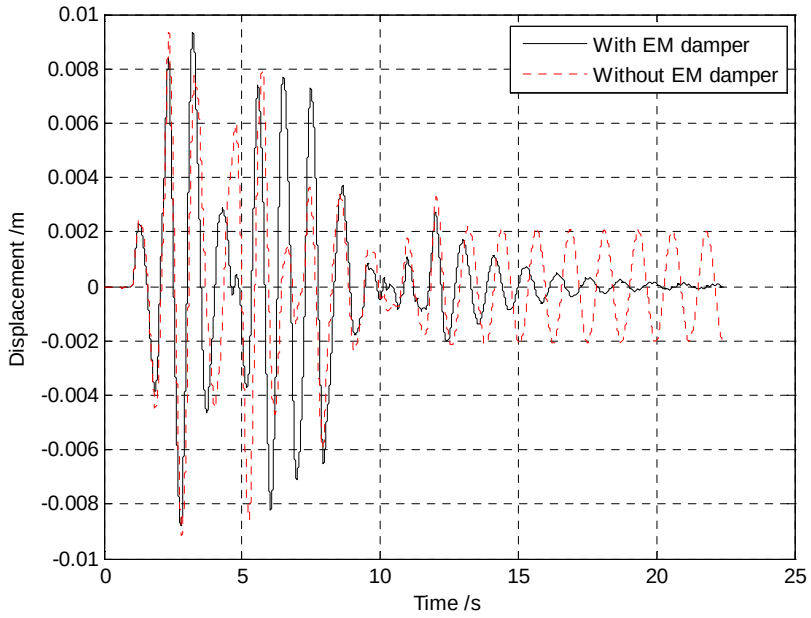


**Figure 6-24: Comparison of base displacement under Hachinohe Earthquake.**

As shown in the figures above, the base isolation structure can always reduce the structural vibration, and improve the safety of the building. Furthermore, for some earthquakes, the EM damper can dramatically enhance the performance of the base isolation system, and remain almost the same performance for the rest. As mentioned above, the summary of maximum amplitude of structural response is presented in Table 6-4. Since for structure without base isolation, the base is fixed with the ground, the "Max. base-dis" is shown "N/A". The bold numbers stand for the lowest maximum amplitude among three systems under the same earthquake excitation. Obviously, the base isolation with EM damper has lowest amplitude in all categories, and thus should be chosen despite the earthquake inputs.

**Table 6-4: Summary of numerical simulation of base isolation system with EM damper (max. rela-dis: maximum relative displacement between 2nd floor and base; max. acc-2nd: maximum acceleration of 2nd floor; max. base-dis: maximum displacement of base )**

| Earthquake | Structural Performance Comparison | Without base isolation | Base isolation without EM damper | Base isolation with EM damper |
|---|---|---|---|---|
| El Centro | Max. rela-dis | 14.5mm | 5.5mm | **3.0mm** |
| | Max. acc-2nd | 5.9m/s$^2$ | 2.0m/s$^2$ | **1.1m/s$^2$** |
| | Max. base-dis | N/A | 67mm | **29mm** |
| Kobe | Max. rela-dis | 9.5mm | 5.8mm | **5.5mm** |
| | Max. acc-2nd | 3.7m/s$^2$ | 2.1m/s$^2$ | **2.0m/s$^2$** |
| | Max. base-dis | N/A | 71mm | **59mm** |
| North Ridge | Max. rela-dis | 17.7mm | 3.6mm | **3.2mm** |
| | Max. acc-2nd | 7.2m/s$^2$ | 1.3m/s$^2$ | **1.2m/s$^2$** |
| | Max. base-dis | N/A | 44mm | **34mm** |
| Hachinohe | Max. rela-dis | 10.9mm | 1.1mm | **0.8mm** |
| | Max. acc-2nd | 4.7m/s$^2$ | 0.4m/s$^2$ | **0.3m/s$^2$** |
| | Max. base-dis | N/A | **9.3mm** | **9.3mm** |

## 6.6 Summary

This chapter has proposed a mathematical model for a prototype moving magnet electromagnetic damper device based on quasi-static electromagnetic theory. The EM damper has the ability to convert the kinetic energy into electric energy without any external excitation, and thus produce a resistant force. The damping force-velocity relationship is derived in this chapter as shown in (Eqn. 6-42), which includes the modeling of the damping coefficient as shown in (Eqn. 6-22), the coil resistance as shown in (Eqn. 6-23) and the coil inductance as shown in (Eqn. 6-37). In addition, the experimental measurements have validated the mathematical model within a reasonable

error range. This EM damper prototype and its mathematical model will be utilized in the next chapter of base-isolated structure and Chapter 7 of subsea jumper system.

Furthermore, this chapter has presented a promising application of prototype EM dampers in structural vibration suppression. The EM damper was attached to a base isolation structural model to behave as both energy dissipation and vibration damping device. Under various earthquake excitations, the structural response was simulated based on the proposed mathematical model of EM damper and the linear model derived from the experimental setup presented in 5.4. The numerical results illustrate that the base isolation system with EM damper always has the most promising performance in spite of the earthquake excitations.

# Chapter 7. Subsea Jumper System with Hybrid Electromagnetic Damper

As mentioned in the literature review, supplemental passive damping systems can resolve the issue of excessive structural vibration of the unsupported part in subsea jumper systems. With extreme conditions, intense vibrations may result in fatigue at the bend, which may cause system down time or even oil leak. In this chapter, we investigate the utilization of smart materials and structures in the area of offshore oil and gas industry. Subsea jumper system is a commonly used structure to reduce the stress level of the pipeline connections between underwater devices. A high stress may cause failure due to fatigue under millions of cycles of vibrations, and lead to an oil leak. Although subsea jumpers can dramatically protect the connections, they also endure extensive structural vibrations. Thus, advanced damping strategy should be applied to subsea jumper systems to suppress the structural vibrations.

Based on the knowledge in previous chapters, a hybrid EM damper, based on a prototype EM damper and superelastic SMA helical springs, is designed as both energy dissipation and position restore device. Two types of passive damping scenarios are presented in this chapter, and follow the numerical results. Sensitivities of the proposed subsea jumper systems area are also studied by modifying the mass matrix of the subsea jumper model in the numerical simulation.

## 7.1 Mathematical Model of Subsea Jumper System

To initialize the numerical simulations, subsea jumper systems should be properly modeled (Peng *et al*., n.d.). Figure 7-1 shows a three dimensional picture of a normal subsea jumper system. The two ends connect to underwater devices, such as

Christmas trees, risers and manifolds. In this dissertation, a simple finite element method (FEM) is used to model a regular subsea jumper system.

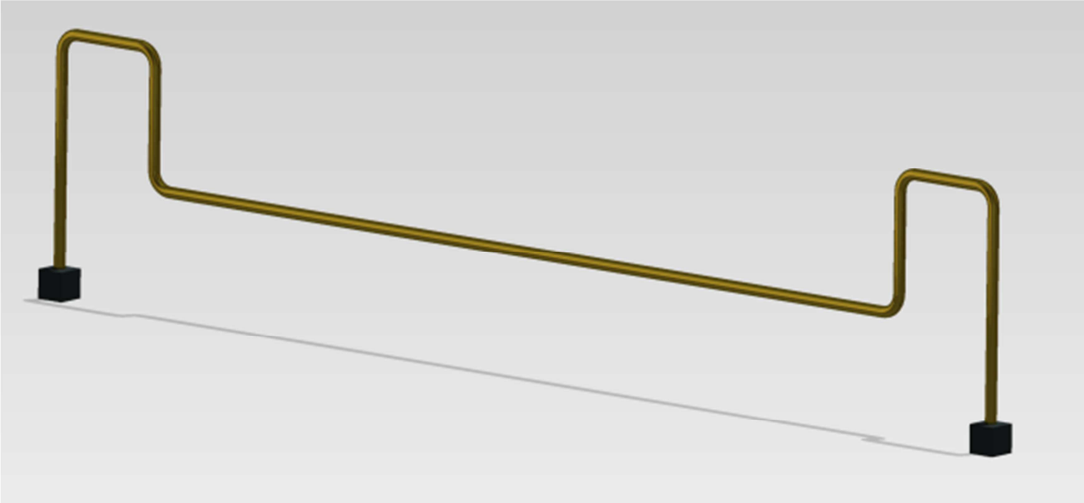

**Figure 7-1: 3D picture of a regular subsea jumper system.**

As shown in Figure 7-2, the subsea jumper system is divided into 11 different nodes. The mass of *ith* node is $m_i$, and the stiffness between *ith* node and *jth* is $k_{ij}$. Assume the damping ratio $\xi = 0.005$ universally in the subsea jumper. Consider the material of the pipelines used in the subsea jumper system is regular steel with isotropic properties listed in Table 7-1.

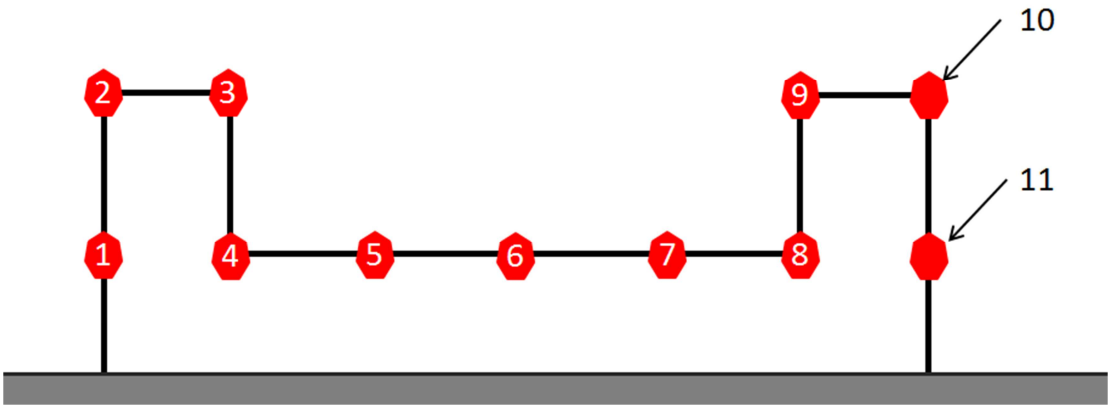


**Figure 7-2: Nodes distribution for FEM modeling subsea jumper systems.**

**Table 7-1: Isotropic properties of steel**

| Modulus of Elasticity E (Pa) | Poisson's Ratio U | Density $\rho$ (kg/m$^3$) | Minimum Yield Stress $F_y$ (Pa) |
|---|---|---|---|
| $1.999E+11$ | 0.3 | 7697.2 | $2.482E+08$ |

Consider $x_i$ is the displacement at *ith* node. Assume the connections between nodes are rigid, the subsea jumper system can be modeled as a second order system as

$$M\ddot{X} + C\dot{X} + KX = 0, \quad \textbf{(Eqn. 7-1)}$$

where the state variable $X = \begin{bmatrix} x_1 \\ x_2 \\ \vdots \\ x_{10} \\ x_{11} \end{bmatrix}$, the mass matrix $M = \begin{bmatrix} m_1 & 0 & \cdots & 0 & 0 \\ 0 & m_2 & \vdots & \vdots & \vdots \\ 0 & 0 & \ddots & 0 & 0 \\ \vdots & \vdots & \vdots & m_{10} & 0 \\ 0 & 0 & \cdots & 0 & m_{11} \end{bmatrix}$, the stiffness matrix $K$ is determined by inversing the flexibility matrix $\Delta$ that is achieved by using SAP2000, and the damping matrix $C$ is calculated by using the Rayleigh theory (Tedesco *et al*., 1999).

Thus, the state space model for the subsea jumper system is

$$\begin{bmatrix} \dot{X} \\ \ddot{X} \end{bmatrix} = \begin{bmatrix} 0 & I \\ -M^{-1}K & -M^{-1}C \end{bmatrix} \begin{bmatrix} X \\ \dot{X} \end{bmatrix} + \begin{bmatrix} 0 \\ -1 \end{bmatrix} \ddot{x}_g, \quad \textbf{(Eqn. 7-2)}$$

$$Y = \begin{bmatrix} X \\ \dot{X} \\ \ddot{X} \end{bmatrix} = \begin{bmatrix} I & 0 \\ 0 & I \\ -M^{-1}K & -M^{-1}C \end{bmatrix} \begin{bmatrix} X \\ \dot{X} \end{bmatrix}, \quad \textbf{(Eqn. 7-3)}$$

where the output $Y$ contains the displacement, the velocity and the acceleration at each node.

## 7.2 Hybrid EM Damper Design with Damping System

In this section, a prototype hybrid EM damper is designed based on the implementation of a prototype EM damper as presented in Chapter 3 and superelastic SMA helical springs as presented in Chapter 7. The design of the hybrid damper is developed from the prototype EM damper. As shown in Figure 7-3, four identical superelastic SMA helical springs are embedded in the prototype hybrid EM damper connecting the pole shoes with damper sides. With applied motions, the hybrid EM damper can generate resistant force with respect to the velocity and the displacement of the motions. The position of the mover in the hybrid EM damper can always be restored due to the superelasticity of the SMA springs.

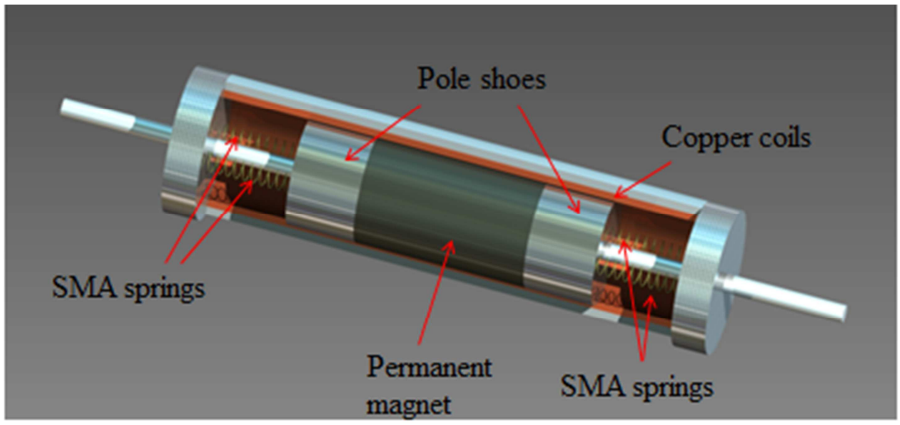


**Figure 7-3: 3D picture of a prototype hybrid EM damper.**

Assume the connections of the SMA springs in the hybrid EM damper is rigid, the modeling approach for the hybrid EM damper will consist of the mathematical model of the prototype EM damper in Chapter 3 and the phenomenological model of superelastic SMA helical springs in Chapter 7.

To apply the hybrid EM damper to the subsea jumper system, two types of damping system are designed as follows: 1) a hook-to-ground subsea jumper system

and 2) a hook-to-tuned mass damper (TMD) subsea jumper system. Both the damping system are connecting to the 6th node in Figure 7-2. The hook-to-ground subsea jumper system, as shown in Figure 7-4, is a regular structure-damper system where the dampers connects the most moving parts to the static locations.

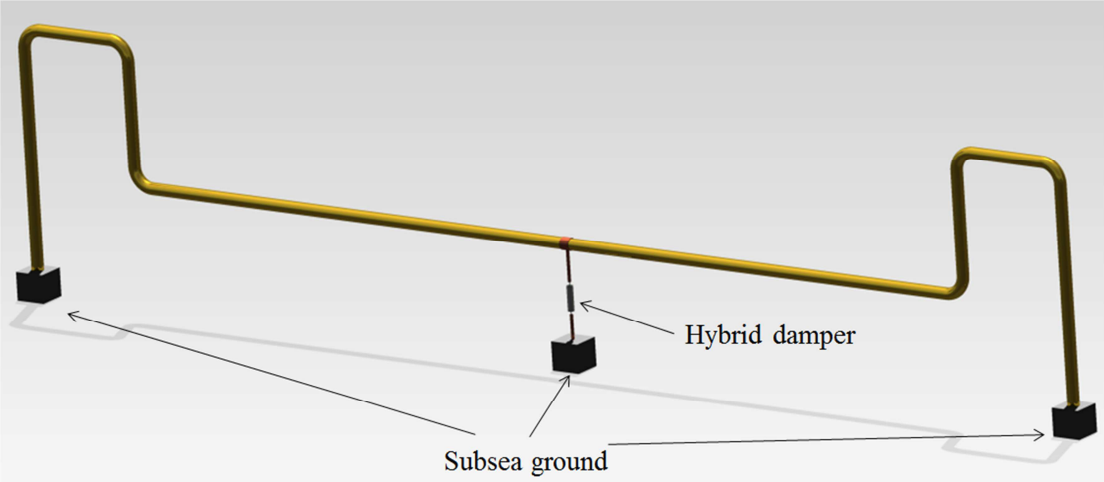


**Figure 7-4: Picture of hook-to-ground subsea jumper system.**

Since the hybrid EM damper is connected between the 6th node of the subsea jumper and sea floor, the state space model of the hook-to-ground subsea jumper system is

$$\begin{bmatrix} \dot{X} \\ \ddot{X} \end{bmatrix} = \begin{bmatrix} 0 & I \\ -M^{-1}K & -M^{-1}C \end{bmatrix} \begin{bmatrix} X \\ \dot{X} \end{bmatrix} + \begin{bmatrix} 0 & 0 \\ -1 & B_d \end{bmatrix} \begin{bmatrix} \ddot{x}_g \\ f_d \end{bmatrix}, \quad \textbf{(Eqn. 7-4)}$$

$$Y = \begin{bmatrix} X \\ \dot{X} \\ \ddot{X} \end{bmatrix} = \begin{bmatrix} I & 0 \\ 0 & I \\ -M^{-1}K & -M^{-1}C \end{bmatrix} \begin{bmatrix} X \\ \dot{X} \end{bmatrix}, \quad \textbf{(Eqn. 7-5)}$$

where $B_d = [0 \quad 0 \quad \cdots \quad -1/m_6 \quad 0 \quad \ldots \quad 0]^T$ with only the 6th element nonzero.

However, to utilize the hook-to-ground damping system, many operations need to be finished at the sea floor that will be significantly costly to build and difficult to

maintain. Thus, to reduce the cost, the hook-to-TMD damping system is presented in Figure 7-5 that most of the assembling can be completed onshore. As shown in the figure, a properly weighted mass (designed to be 1%~10% of the whole system mass) is connected on top of the hybrid EM damper. The kinetic energy of the vibration of the subsea jumper can be transferred to the TMD system, and dissipated by the hybrid EM damper. The stiffness of the TMD $k_{TMD}$ should be properly chosen to match the natural frequency of the TMD system with the natural frequency of the subsea jumper system. Since the first mode is most dominant one in subsea jumper structural vibration, the stiffness is tuned to compensate only the first mode.

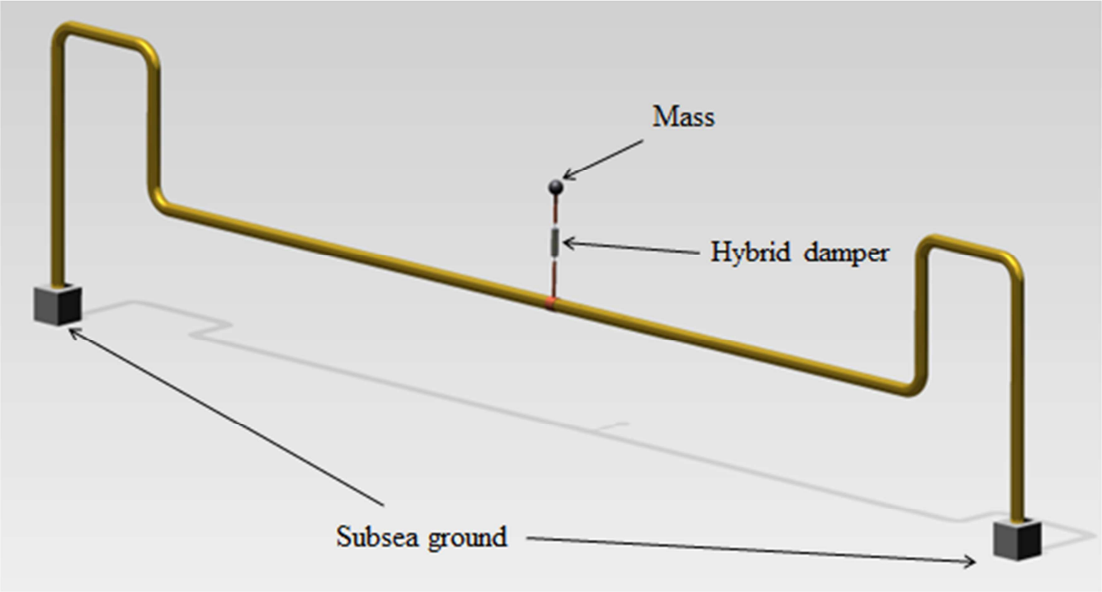


**Figure 7-5: Picture of hook-to-TMD subsea jumper system.**

For the hook-to-TMD subsea jumper system, the new introduced node, the node of the mass $m_{TMD}$, will be considered as the 12$^{th}$ node of the FEM model. Thus,

$$\begin{bmatrix} \dot{\tilde{X}} \\ \ddot{\tilde{X}} \end{bmatrix} = \begin{bmatrix} 0 & I \\ -\tilde{M}^{-1}\tilde{K} & -\tilde{M}^{-1}\tilde{C} \end{bmatrix} \begin{bmatrix} \tilde{X} \\ \dot{\tilde{X}} \end{bmatrix} + \begin{bmatrix} 0 & 0 \\ -1 & \tilde{B}_d \end{bmatrix} \begin{bmatrix} \ddot{x}_g \\ f_d \end{bmatrix}, \quad \textbf{(Eqn. 7-6)}$$

$$\tilde{Y} = \begin{bmatrix} \tilde{X} \\ \dot{\tilde{X}} \\ \ddot{\tilde{X}} \end{bmatrix} = \begin{bmatrix} I & 0 \\ 0 & I \\ -\tilde{M}^{-1}\tilde{K} & -\tilde{M}^{-1}\tilde{C} \end{bmatrix} \begin{bmatrix} \tilde{X} \\ \dot{\tilde{X}} \end{bmatrix}, \quad \textbf{(Eqn. 7-7)}$$

where $\tilde{X} = \begin{bmatrix} X \\ x_{TMD} \end{bmatrix}$, $\tilde{M} = \begin{bmatrix} M & 0 \\ 0 & m_{TMD} \end{bmatrix}$, $\tilde{K} = \begin{bmatrix} K & 0 \\ 0 & k_{TMD} \end{bmatrix}$, $\tilde{C} = \begin{bmatrix} C & 0 \\ 0 & 0 \end{bmatrix}$, and $\tilde{B}_d = \begin{bmatrix} 0 & 0 & \cdots & -1/m_6 & 0 & \cdots & 0 & 1/m_{TMD} \end{bmatrix}^T$ with the 6th and 12th element nonzero.

The priority of the subsea jumper system is to reduce the stress level at the jumper connections to underwater devices, and at the same time, reduce the structural vibration. Thus, the stress at the jumper connections and the displacement of the 6th node will be selected as system performance factors. Assume the subsea jumpers are symmetric, the bending stresses $\sigma$ at the jumper connections are calculated as

$$\sigma = \frac{My}{I_x}, \quad \textbf{(Eqn. 7-8)}$$

where $M$ is the moment about axis of sea floor, $y$ is the perpendicular distance to the axis of sea floor, and $I_x$ is the moment of inertia about the axis of sea floor.

In this dissertation, we only investigate the vertical vibrations of subsea jumpers, but with minor modifications, such designs can be easily applied to horizontal vibrations or combined.

## 7.3 Numerical Simulation

In this section, a numerical example of a subsea jumper system and a prototype hybrid EM damper will be presented and simulated. Figure 7-6 shows the dimensional schematic of the subsea jumper example. This numerical example is built based on an

experimental setup in Smart Materials and Structures Laboratory, University of Houston.

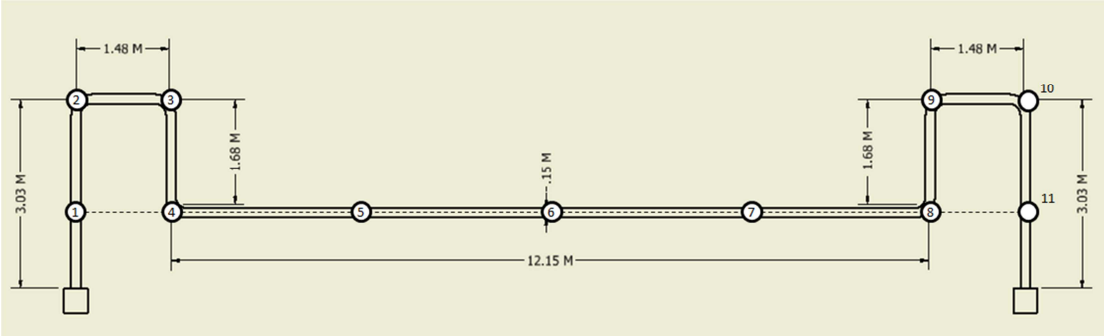


**Figure 7-6: Dimensional schematic of the subsea jumper system in numerical simulation.**

The masses $m_1, m_2, ..., m_{11}$ from 1st node to 11th node are 74.19 kg, 5.55 kg, 44.34 kg, 54.97 kg, 72.78 kg, 68.57 kg, 72.78 kg, 54.97 kg, 44.34 kg, 5.55 kg and 74.19 kg, respectively. The damping ratios are chosen at 0.005 for the first two modes. The stiffness matrix $K$ is achieved by using SAP2000, and the damping matrix $C$ is calculated based on the Rayleigh theory. Detailed information about the state space model of the subsea jumper example can be found in A.2. The first mode of this numerical subsea jumper example is at 2.25 Hz.

The dimensional schematic of the prototype hybrid EM damper example is shown in Figure 7-7. In addition to the EM damper, four identical superelastic SMA helical springs with a length of 50 mm are embedded between the pole shoes and the damper ends. Similar to the prototype EM damper presented in Chapter 3, the hybrid EM damper also has two coils.

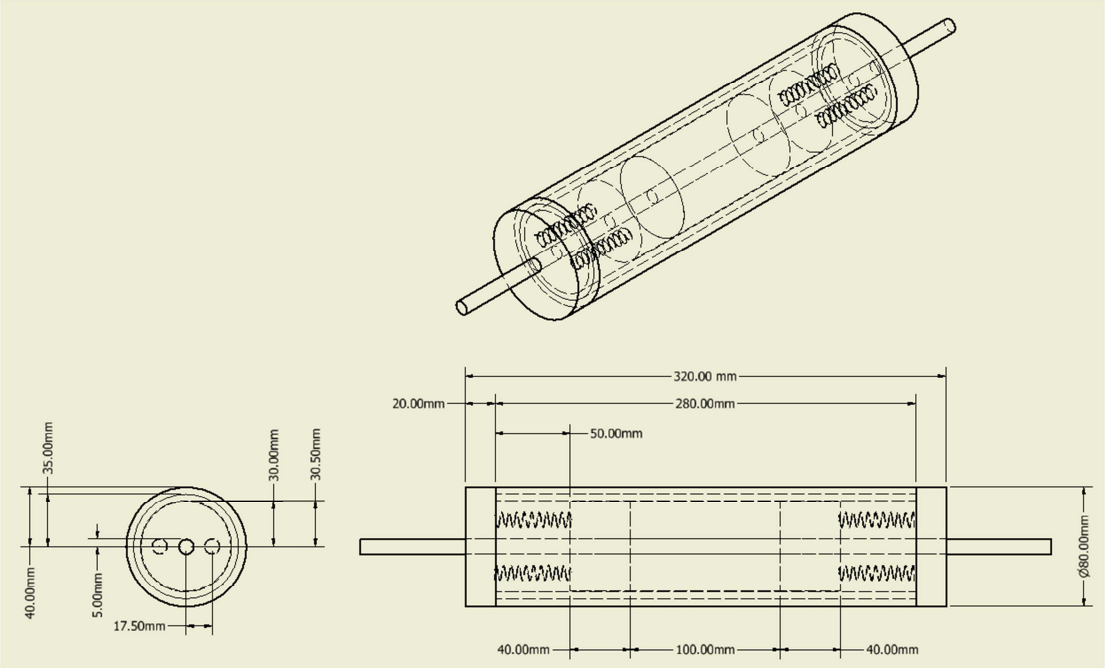


**Figure 7-7: Dimensional schematic of the hybrid EM damper in numerical simulation.**

To calculate the damping coefficient $K_D$, the coil resistance $R_{Coil}$ and the coil inductance $L_{Coil}$, apply the magnetic and the geometric properties of the hybrid EM damper into (Eqn. 6-22), (Eqn. 6-23) and (Eqn. 6-37) yields $K_D = 27.22$ V/N/m, $R_{Coil} = 17.33\,\Omega$, and $L_{Coil} = 9.18$ mH. The load resistance $R_{Load}$ is chosen at 34 $\Omega$.

For the hook-to-TMD subsea jumper system, the mass $m_{TMD}$ of the TMD system is chosen at 18.14 kg, and the stiffness $k_{TMD}$ is calculated at 3622 N/m to equalize the first mode natural frequency at 2.25 Hz.

The sensitivity studies area included in the numerical simulation by reducing 20% of the masses at node 2, 3, 4, 8, 9 and 10, since those nodes are the nodes at the bends which mass may slightly vary due to different methods of manufacture.

### 7.3.1 Hook-to-Ground Subsea Jumper System

To evaluate the performance of the hook-to-ground subsea jumper system, it is compared with a regular subsea jumper system under two different excitations: free vibration and El Centro earthquake signal. For the comparisons in free vibrations, both the subsea jumpers are excited at the first mode before 10s, and release the excitation thereafter. Between a regular subsea jumper without any additional damping device and a hook-to-ground subsea jumper, Figure 7-8 and Figure 7-9 show the comparison of the bending stress at the jumper connections and the displacement at the $6^{th}$ node, respectively. From the figures, it is obviously that, comparing to a regular subsea jumper, the hook-to-ground system can dramatically increase the damping and reduce the stress and the structural vibrations.

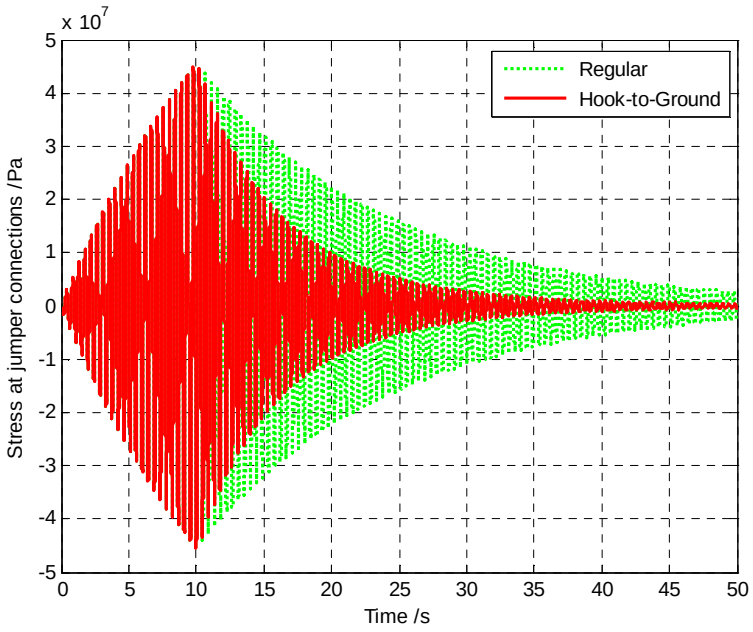


**Figure 7-8: Free vibration comparison of bending stress at jumper connections (regular vs. hook-to-ground).**

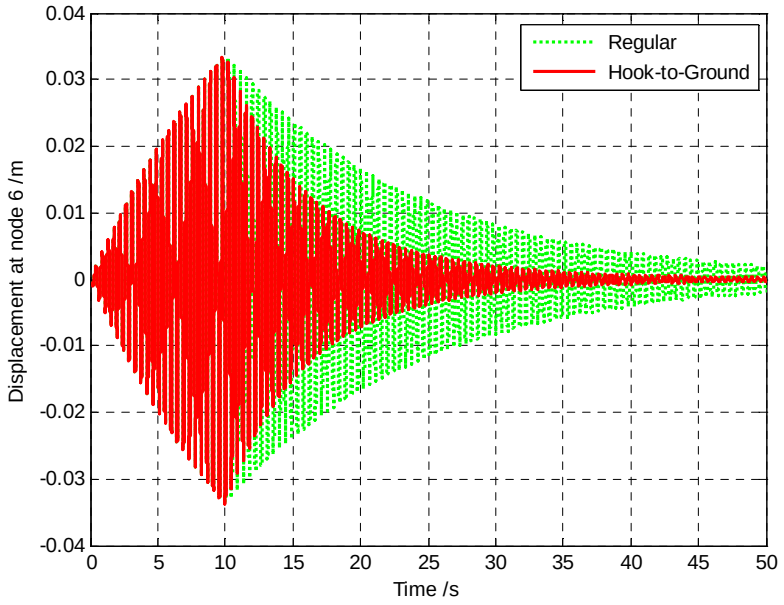


**Figure 7-9: Free vibration comparison of displacement at node 6 (regular vs. hook-to-ground).**

To evaluate the structural performance under random excitations, an El Centro earthquake signal is chosen as the excitation input. Similar to the free vibrations, the bending stress at the jumper connections and the displacement at node 6 will be compared. Figure 7-10 shows the comparison of the bending stress, and Figure 7-11 shows the comparison of the displacement. Obviously, the hook-to-ground subsea jumper system significantly depresses the structural vibration and the stress at the connections.

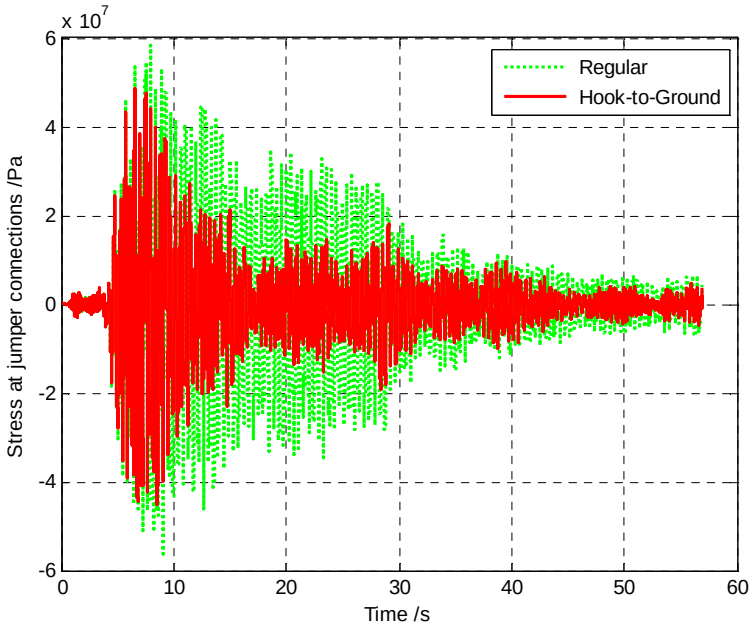


**Figure 7-10: Earthquake comparison of bending stress at jumper connections (regular vs. hook-to-ground).**

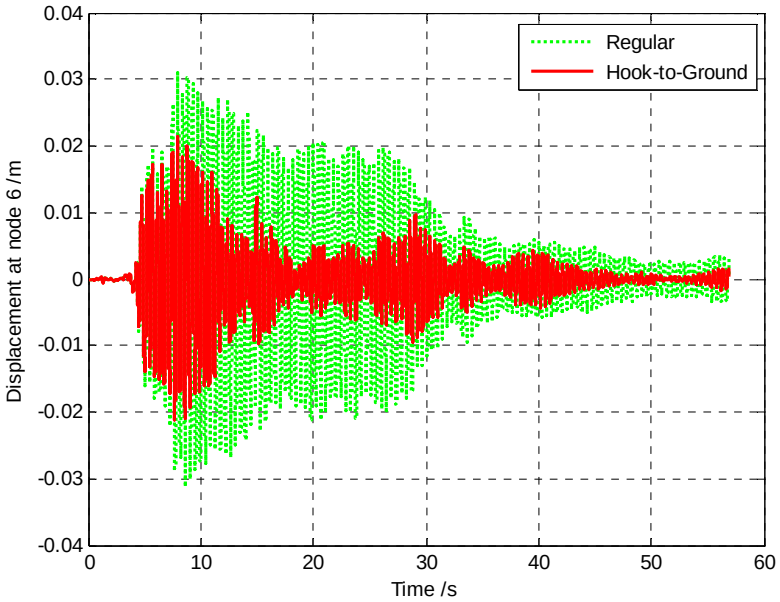


**Figure 7-11: Earthquake comparison of displacement at node 6 (regular vs. hook-to-ground).**

### 7.3.2 Hook-to-TMD Subsea Jumper System Hook-to-TMD

As mentioned before, the hook-to-ground subsea jumper system is costly and difficult to install and maintain, the hook-to-TMD system is presented with numerical simulations. In this subsection, three types of subsea jumper system are simulated including a regular subsea jumper system (regular), a subsea jumper system with only TMD without additional damping devices (TMD only), a hook-to-TMD subsea jumper system (hook-to-TMD). Similar to the hook-to-ground system, excitations of free vibrations and earthquake are utilized for comparison purpose. Figure 7-12 and Figure 7-13 show the comparisons of the bending stress at the jumper connections and the displacement of the 6$^{th}$ node, respectively, under the free vibration excitation. Figure 7-14 and Figure 7-15 present the comparisons under the El Centro earthquake excitation.

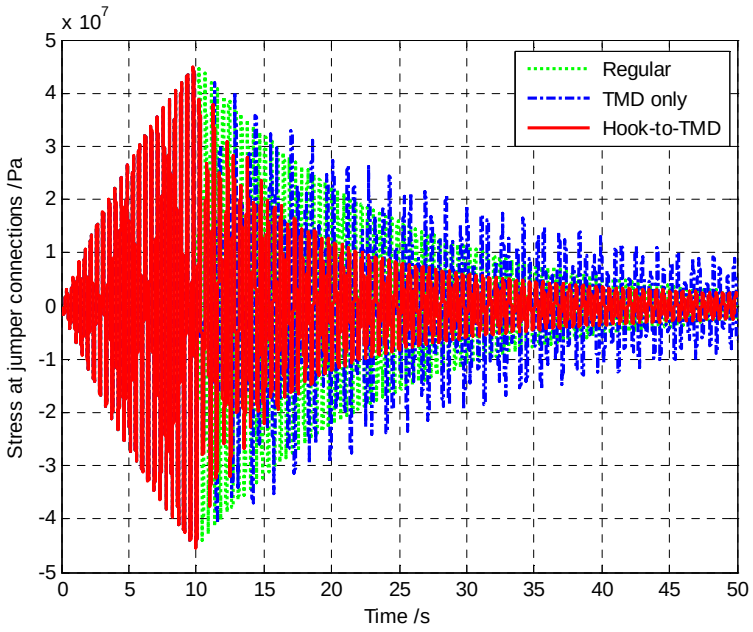


**Figure 7-12: Free vibration comparison of bending stress at jumper connections (regular vs. TMD only vs. hook-to-TMD).**

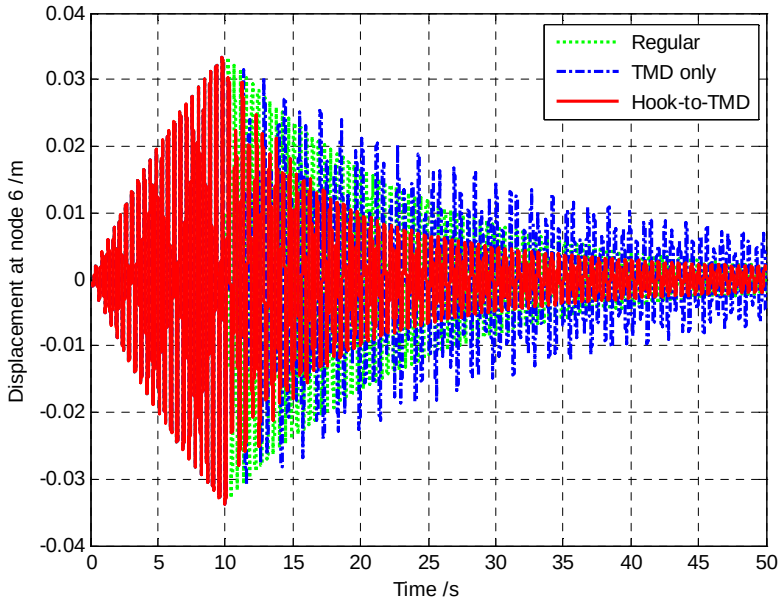


**Figure 7-13: Free vibration comparison of displacement at node 6 (regular vs. TMD only vs. hook-to-TMD).**

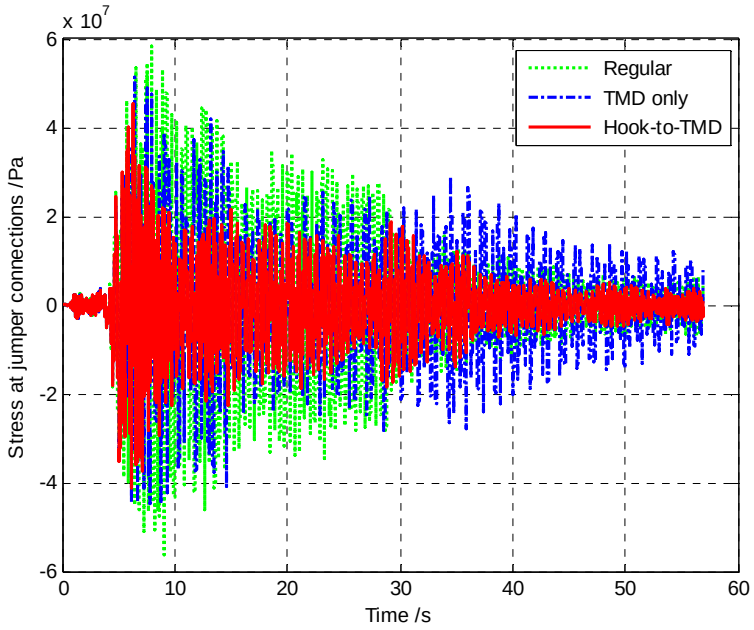


**Figure 7-14: Earthquake comparison of bending stress at jumper connections (regular vs. TMD only vs. hook-to-TMD).**

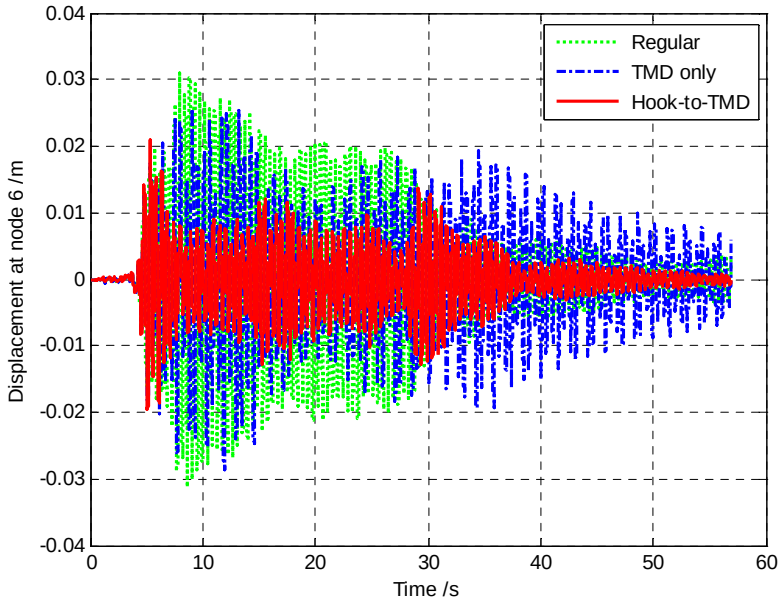


**Figure 7-15: Earthquake comparison of displacement at node 6 (regular vs. TMD only vs. hook-to-TMD).**

As shown in the above figures, the TMD only system can slightly suppress the maximum amplitude. However, the structural vibration of the TMD only system saturates more slowly than the regular subsea jumper, because the TMD only system has limited damping itself. Thus, the TMD only system should not be utilized. On the other hand, the hook-to-TMD system greatly improves the performance of the TMD only system.

The numerical simulations are summarized in Table 7-2. Based on the absolute maximum value and mean value of the stress at the connections and the displacement at the $6^{th}$ node, the best performance from the table is the hook-to-ground subsea jumper system. However, considering the cost of the hook-to-ground system is too high for experimental applications, the hook-to-TMD system should be the more reasonable choice for practical offshore applications.

**Table 7-2: Summary of subsea jumper systems' performance**
**(Stress: bending stress at jumper connections; Dis: displacement at node 6)**

| System Type | Performance Factor | Free Vibration | | El Centro Earthquake | |
|---|---|---|---|---|---|
| | | Max | Mean | Max | Mean |
| Regular subsea jumper | Stress (Pa) | 4.55e07 | 9.65e06 | 5.83e07 | 1.04e07 |
| | Dis. (mm) | 33.8 | 7.2 | 31.3 | 7.4 |
| Hook-to-ground subsea jumper | Stress (Pa) | 4.55e07 | 4.92e06 | 4.87e07 | 5.26e06 |
| | Dis. (mm) | 33.8 | 3.6 | 21.5 | 3.1 |
| Subsea jumper with TMD only | Stress (Pa) | 4.55e07 | 9.96e06 | 5.14e07 | 9.30e06 |
| | Dis. (mm) | 33.8 | 8.1 | 28.6 | 7.1 |
| Hook-to-TMD subsea jumper | Stress (Pa) | 4.55e07 | 5.99e06 | 4.54e07 | 5.35e06 |
| | Dis. (mm) | 33.8 | 4.9 | 20.9 | 3.5 |

### 7.3.3 Sensitivity Study of Subsea Jumper Systems

For practical applications, the sensitivity of the proposed subsea jumper systems should be studied, since the precise model of the practical subsea jumper may be difficult to achieve due to various configurations, assembling approaches and so on. In this subsection, the numerical model of the subsea jumper system is modified by reducing 20% of the masses at all bends. The first natural frequency of the subsea jumper system in numerical simulation has changed from 2.25 Hz to 2.28 Hz. Two types of excitation signal, a free vibration and an El Centro earthquake excitation, are used to evaluate the performance of the modified subsea jumper system. Figure 7-16 through Figure 7-19 show the comparisons of structural vibration responses under the two excitations.

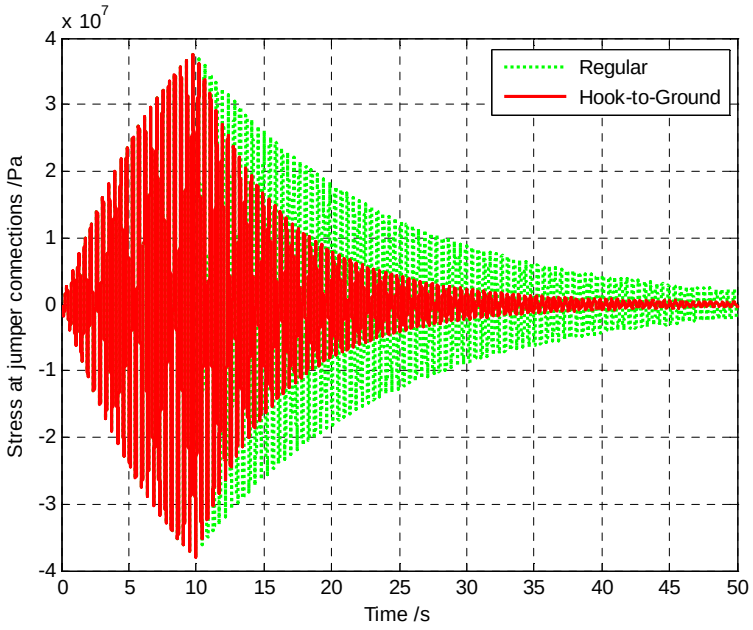


**Figure 7-16: Free vibration comparison of bending stress at jumper connections for sensitivity study (regular vs. hook-to-ground)**

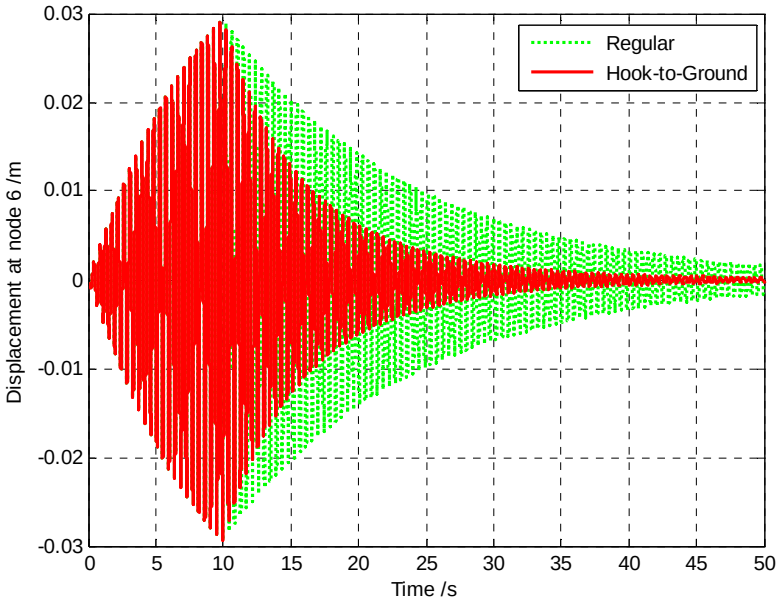


**Figure 7-17: Free vibration comparison of 6th node displacement for sensitivity study (regular vs. hook-to-ground)**

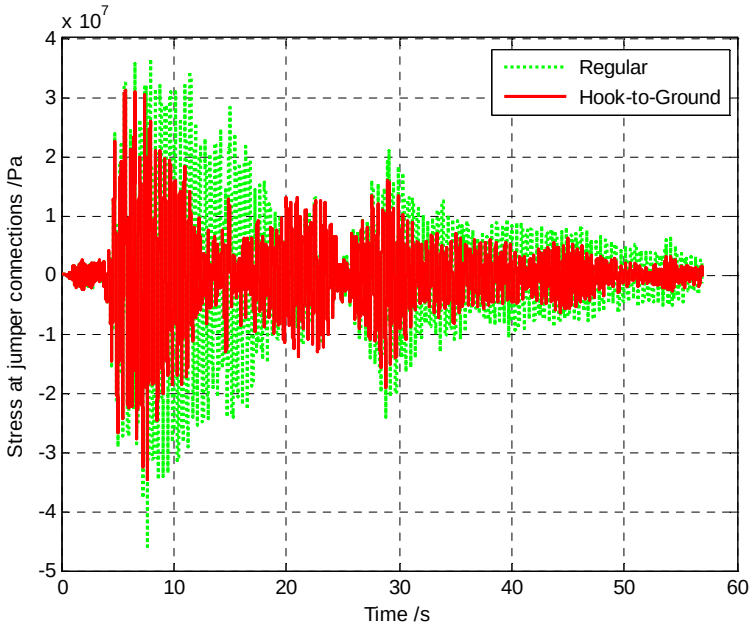


**Figure 7-18: Earthquake comparison of bending stress at jumper connections for sensitivity study (regular vs. hook-to-ground)**

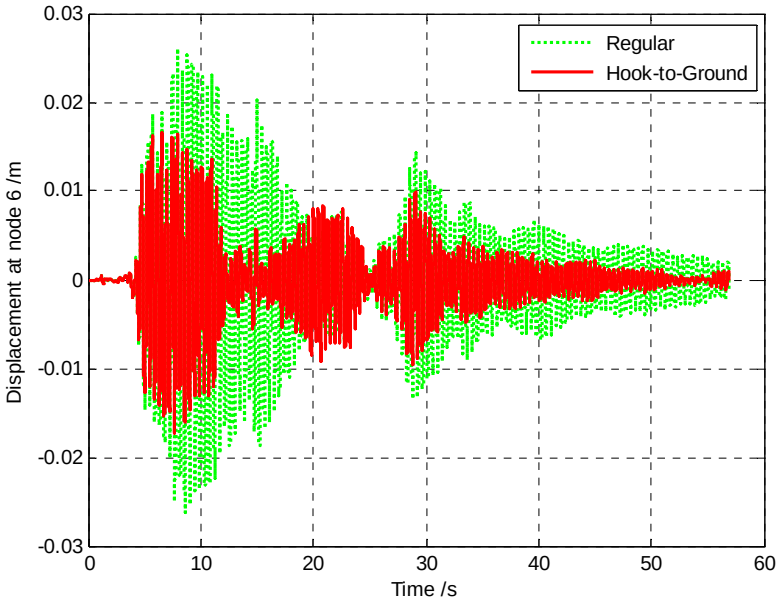


**Figure 7-19: Earthquake comparison of 6th node displacement for sensitivity study (regular vs. hook-to-ground)**

In Figure 7-16 and Figure 7-17, the structural performances of the modified subsea jumper system have not changed dramatically, and the hook-to-ground subsea jumper system has significantly increased the damping. However, as shown in Figure 7-18 and Figure 7-19, the change of the natural frequency has resulted in an apparent change in the structural vibration. Despites the change, the hook-to-ground subsea jumper can still promisingly suppress the vibration.

Since the hook-to-TMD subsea jumper systems require a preliminary design of TMD system based on the natural frequency of the subsea jumper, the change of the natural frequency may worsen the performance of the hook-to-TMD systems. Figure 7-20 through Figure 7-23 show the structural performance comparing the modified subsea jumper system without supplemental damping, the modified subsea jumper system with TMD, and the hook-to-TMD system.

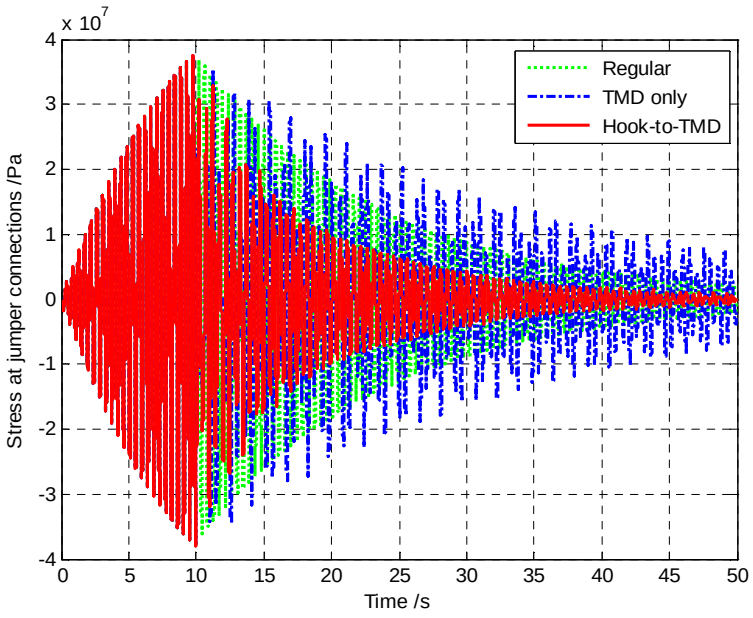


**Figure 7-20: Free vibration comparison of bending stress at jumper connections for sensitivity study (regular vs. TMD only vs. hook-to-TMD)**

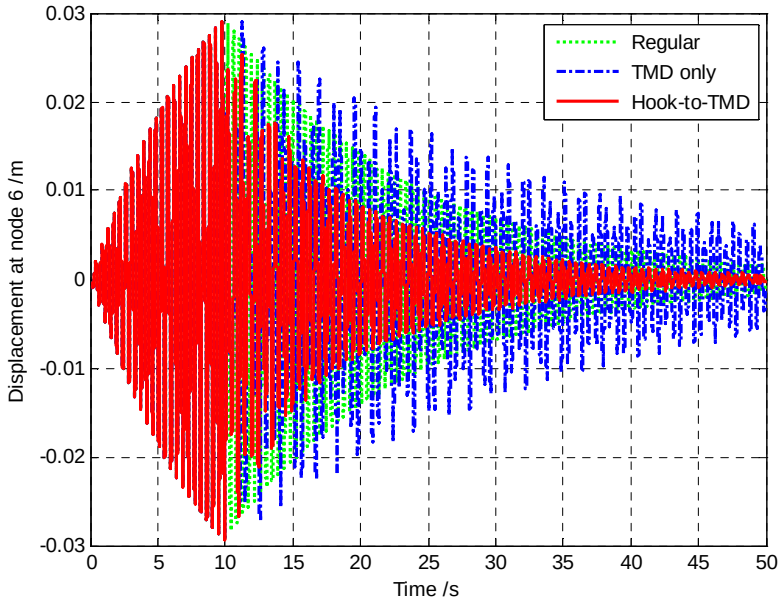


**Figure 7-21: Free vibration comparison of 6th node displacement for sensitivity study (regular vs. TMD only vs. hook-to-TMD)**

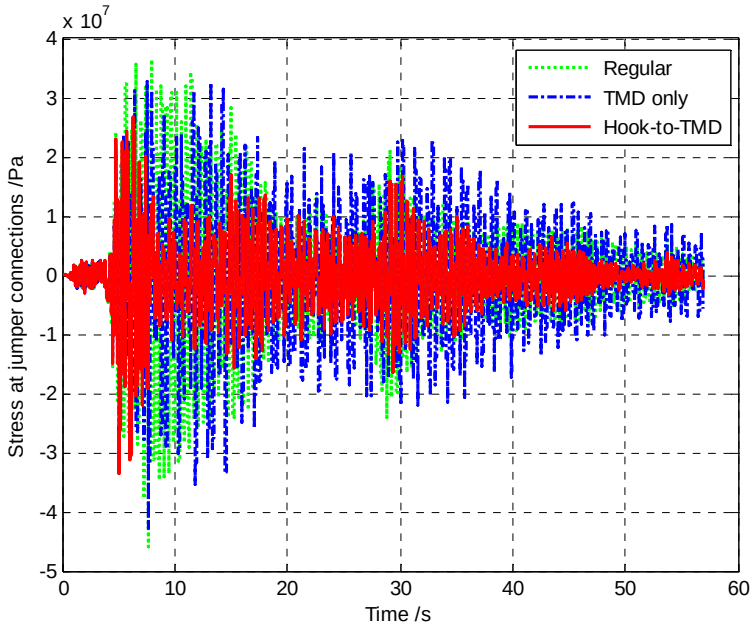


**Figure 7-22: Earthquake comparison of bending stress at jumper connections for sensitivity study (regular vs. TMD only vs. hook-to-TMD)**

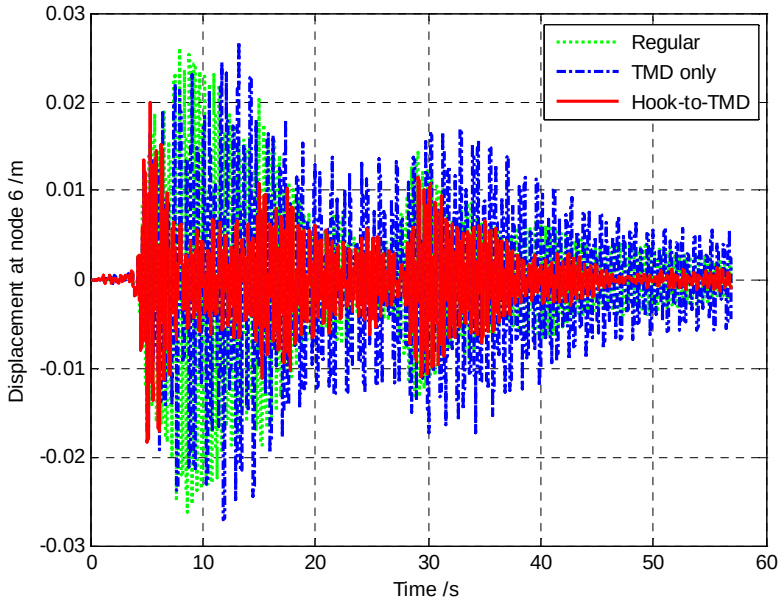


**Figure 7-23: Earthquake comparison of 6th node displacement for sensitivity study (regular vs. TMD only vs. hook-to-TMD)**

Obviously, the structural vibration performances of the subsea jumper system with TMD only have been significantly increased especially in the El Centro earthquake excitation. However, the hook-to-TMD system can adapt the change of the natural frequency, and dramatically reduce the structural vibration comparing to the regular subsea jumper system with reduced mass.

Table 7-3 shows the summary of the numerical simulation results for sensitivity study. For both free vibration and El Centro earthquake excitations, nevertheless the system matrices are observably changed, the hook-to-TMD subsea jumper system is still the best candidate for practical use due to the high cost of the hook-to-ground subsea jumper systems.

**Table 7-3: Summary of subsea jumper systems' performance for sensitivity study (Stress: bending stress at jumper connections; Dis: displacement at node 6)**

| System Type | Performance Factor | Free Vibration | | El Centro Earthquake | |
|---|---|---|---|---|---|
| | | Max | Mean | Max | Mean |
| Regular subsea jumper | Stress (Pa) | 3.68e07 | 9.07e06 | 4.60e07 | 6.87e06 |
| | Dis. (mm) | 28.8 | 6.1 | 26.2 | 5.1 |
| Hook-to-ground subsea jumper | Stress (Pa) | 3.68e07 | 4.92e06 | 3.46e07 | 4.05e06 |
| | Dis. (mm) | 28.8 | 3.7 | 17.3 | 2.8 |
| Subsea jumper with TMD only | Stress (Pa) | 3.68e07 | 8.40e06 | 4.29e07 | 7.60e06 |
| | Dis. (mm) | 28.8 | 7.2 | 27.2 | 6.2 |
| Hook-to-TMD subsea jumper | Stress (Pa) | 3.68e07 | 4.38e06 | 3.35e07 | 3.72e06 |
| | Dis. (mm) | 28.8 | 3.7 | 19.9 | 2.7 |

## 7.4 Summary

In this chapter, the regular subsea jumper system is modeled by using the FEM method with a numerical example. Combining the applications of the prototype EM damper and the superelastic SMA helical springs, a prototype hybrid EM damper is presented. To suppress the structural vibrations and stress at the jumper connections, a hook-to-ground and a hook-to-TMD subsea jumper system are proposed with the utilization of the hybrid EM damper. Numerical simulations show that although the hook-to-ground subsea jumper system has the relatively promising performance, as a concern of reducing cost in installations, the hook-to-TMD system should be chosen as the most practical damping system in offshore oil and gas industry.

# Chapter 8. Conclusions and Future Works

## 8.1 Conclusions

The research presented in this dissertation has developed several new types of advanced modeling approach for smart materials and structures. The motivation of this research is driven by the difficulty of modeling or controlling nonlinear behaviors such as hysteresis among smart materials and structures. With a successful model, a numerical simulation can be accurately achieved before applying any new smart materials or structures into an unknown application, which is also a major objective of this research. Spanning various modeling methods and their utilizations, the dissertation began with an introduction and literature survey on the existing technology of smart materials and structures, and ended with several considerably successful applications in both numerical simulations and experiments.

The content of this dissertation can be divided into four major categories: 1) development of an innovative nonlinear autoregressive exogenous model (NARX) based on recurrent neural networks for forward estimation and inverse control purpose with an application on an ultra-thin shape memory alloy (SMA) wire, 2) introduction of an advanced phenomenological model for superelastic SMA helical springs, 3) design of a prototype electromagnetic (EM) damper and development of the corresponding mathematical model, 4) utilization of superelastic SMA helical springs and prototype EM dampers in base-isolated structure with experimental test, and 5) conceptual design of a hybrid EM damper with an application on subsea jumper systems. These contents are described and summarized in the following subsections.

### 8.1.1 NARX Recurrent Neural Network Model

In many smart materials and structures, hysteresis behaviors between outputs and inputs can be easily observed. The hysteretic behaviors are mostly nonlinear, which makes modeling and controlling smart materials and structures remarkably complicated. To solve this problem, an innovative nonlinear autoregressive exogenous model (NARX) based on recurrent neural network (RNN) structure was presented that can be used in forward models for behavioral estimations as well as inverse models for control purposes. The proposed network structure synthesized the advantage of the Jordan RNN structure and the Elman RNN structure, and with the specialized training procedure, could achieve a better performance than a regular NARX model (Jordan network) to estimate hysteretic behaviors.

Furthermore, this network structure was tested on an experimental ultra-thin SMA wire setup for both forward modeling and inverse modeling. The displacement of the SMA wire was driven by an applied electrical signal. The experimental results show that, under various frequencies, the proposed forward NARX RNN model estimated the hysteresis loops with considerably limited errors, and the inverse NARX RNN model functioned as a feedforward controller to track the displacement. The performance of the inverse model could be dramatically improved by adding a simple feedback control algorithm.

### 8.1.2 Phenomenological Model of Superelastic SMA Helical Springs

This part of research was motivated by potential utilizations of superelastic SMA helical springs as energy dissipation and position restore devices with numerical

simulations. By observing the force-displacement behaviors of multiple superelastic SMA springs, an innovative phenomenological model was proposed to estimate the forces based on the displacements. Both major loops and minor loops were thoroughly considered and validated by a self-trained superelastic SMA spring.

Then, the self-trained superelastic SMA springs were applied to an experimental base-isolated structure. Shown by the experimental results, the superelastic SMA springs dramatically reduced the structural vibrations of the base-isolated structure, and limited the base movement.

### 8.1.3 Mathematical Modeling of EM Damper

This part of research began with proposing and analyzing a prototype EM damper with a moving permanent magnet. Based on quasi-static electromagnetic theories, a mathematical model of the designed prototype EM damper was derived. The damping coefficient and circuit impedances are determined by the geometric, magnetic and electric property of the device. The force-velocity relationship of the EM damper demonstrated that it is similar to an ideal damper. The behavior of the EM damper was described by a first order transfer function with a time delay relating the velocity to the resistant force of the damper. In the end, the mathematical model was validated by experimental data provided by the manufacture.

Similar to the superelastic SMA springs, the prototype EM damper was utilized to base isolation systems. The EM damper was attached to a base isolation structural model to behave as both energy dissipation and vibration damping device. The numerical simulation demonstrated that the base-isolated structure with EM damper could significantly reduce the structural vibration under various earthquake excitations.

### 8.1.4 Hybrid EM Damper Design in Subsea Jumper System

Offshore oil and gas industry is a challenging area for mechanical devices due to the high cost and difficulty to install and maintenance. This part of research focused on suppressing the structural vibration and stress of subsea jumpers by introducing additional damping devices. The regular subsea jumper system was modeled by using the FEM method with a numerical example. Combining the applications of the prototype EM damper and the superelastic SMA helical springs, a prototype hybrid EM damper was presented. To suppress the structural vibrations and stress at the jumper connections, a hook-to-ground and a hook-to-TMD subsea jumper system were proposed with the utilization of the hybrid EM damper. Numerical simulations show that although the hook-to-ground subsea jumper system has the most promising performance, the hook-to-TMD system should be chosen as the most practical damping system in offshore oil and gas industry.

## 8.2 Future Research

This current research has broadened the area of advanced modeling for nonlinear systems such as smart materials and structures. In order to improve and implement the proposed modeling and utilizations into practical applications, future research is needed as follows:

- An actual implementation of electromagnetic damper depends significantly on the fabrication of the device itself. More experiments are required to bring the potential implementation into practical applications.
- One obvious advantage of the prototype electromagnetic damper is that not only it does not require external energy, but is also capable of providing extra power

by cutting electromagnetic field. With a proper utilization of this property, structures like base isolation system or subsea jumper system can generate and store energy from the structural vibration that can be used as an emergent energy source. This will be significantly helpful when vibration excitations could endanger the power grids.

- The proposed nonlinear autoregressive exogenous model (NARX) based on recurrent neural networks supposes to success on modeling various smart materials and structures. This advanced modeling approach can be applied to other applications, such as piezoceramics and magnetorheological fluids.
- Advanced feedback control algorithms, such as sliding mode controllers, fuzzy logic controllers, to name a few, can be developed to improve the performance of the inverse NARX model based on recurrent neural networks, if the real-time feedback signals are available.

# References

An, Xiaoran. "Novel neural network and its application in hysteresis modeling." *Modeling, Simulation and Visualization Methods, 2010 Second International Conference*. Sanya, Hainan, China: IEEE, 2010. 203-205.

Asua, E., Etxebarria, V. and Garcia-Arribas, A. "Neural network-based micropositioning control of smart shape memory alloy actuators." *Engineering Applications of Artificial Intelligence 21*, 2008: 796-804.

Attanasi, G. Auricchio and F. Urbano, M. "Theoretical and experimental investigation on SMA superelastic springs." *Journals of Materials Engineering and Performance, Vol. 20(4-5)*, 2011: 706-711.

Auge, L. J. *Structural magnetic induction dampers in buildings.* Master Thesis, MIT, 2003.

Bomarita, G. *A study on energy harvesting through the use of electromagnetic dampers in motion control schemes.* Master Thesis, Cambridge: MIT, 2009.

Carruth, A. L. and Cerkovnik, M. E. "Jumper VIV - new issues for new frontiers." *International Offshore and Polar Engineering Conference.* Lisbon, Portugal, 2007.

Chang, L.C. and Read, T.A. *Trans. AIME, Vol 191*, 1951: 47.

Chau, E.T., Friend, C.M., Allen, D.M., Hora, J. and Webster, J.R. "A technical and economic appraisal of shape memory alloys for aerospace applications." *Materials Science and Engineering: A, Volume 438-440*, 2006: 589-592.

Cheng, T. H., Li, Y., Ren, M. and Shen, Y. D. "Coil based electromagnetic damper using semi-passive switching method." *2010 International Conference on Intelligent Computation Technology and Automation.* Changsha, 2010. 966-969.

Choi, K., Jung, H., Lee, H. and Cho, S. "Seismic protection of base-isolated building with nonlinear isolation system using smart passive control strategy." *Structural Control and Health Monitoring, Vol. 15*, 2008: 785-796.

de Araujo, C.J., da Silva, N.J., da Silva, M.M. and Gonzalez, C.H. "A comparative study of Ni-Ti and Ni-Ti-Cu shape memory alloy processed by plasma melting and injection molding." *Materials & Design, Volume 32, Issue 10*, 2011: 4925-4930.

Ebrahimi, B. *Development of hybrid electromagnetic dampers for vehicle suspension systems.* PhD Thesis, Waterloo: University of Waterloo, 2009.

Elman, J. L. "Finding structure in time." Technical Report CRL 8801, San Diego, CA, 1988.

Fodor, M. G. and Redfield, R. C. "The variable linear transmission for regenerative damping in vehicle suspension control." *American Control Conference.* Chicago, IL, USA, 1992. 26-30.

Hornik, K., Stinchcombe, M. and White, H. "Multilayer feedforward networks are universal approximators." *Neural Networks, Volume 2, Issue 5*, 1989: 359-366.

Housner, G.W., Bergman, L.G., Caughey, T.k., Chassiakos, A.G., Claus, R.O., Masri, S.F., Skelton, R.E., Soong, T.T., Spencer, B.F. and Yao, J.T. "Structural control:

past, present and future." *Journal of Engineering Mechanics, Vol. 123,* 1997: 897-971.

Huang, B., Song, G. and Zhang, H. "Constitutive model for SMA helical springs." *To be published,* n.d.

Hughes, D. "Preisach modeling of piezoceramic and shape memory alloy hystersis." *Proceedings of the 4th IEEE Conference on Control Applications.* Albany, NY: IEEE, 1995. 1086-1091.

Jordan, M. I. "Attractor dynamics and parallelism in a connectionist sequential machine." In *Artificial Neural Networks,* by J. Diederich, 112-217. New York, USA: IEEE Press Piscataway, 1990.

Kareem, A. "Modelling of base-isolated buildings with passive dampers under wind." *Journal of Wind Engineering and Industrial Aerodynamics, Volume 72,* 1997: 323-333.

Karras, D.A. and Zorkadis, V. "On neural network techniques in the secure management of communication systems through improving and quality assessing pseudorandom stream generators." *Neural Networks, Volume 16, Issue 5-6,* 2003: 899-905.

Kelly, J. "Aseismic base isolation: review and bibliography." *Soil Dynamics and Earthquake Engineering, Vol.5, Issue 4,* 1986: 202-216.

Kilicarslan, A., Song, G. and Grigoriadis, K. "Modeling and hysteresis compensation in a thin SMA wire using ANFIS methods." *Journal of Intelligent Material Systems and Structures, Vol. 22,* 2011: 45-57.

Kim, Y., Langari, R. and Hurlebaus, S. "Semi-active nonlinear control of a building with a magnetorheological damper system." *Mechanical Systems and Signal Processing, Vol. 23*, 2009: 300-315.

Kori, J. G. and Jangid, R. S. "Semiactive control of seismically isolated bridges." *International Journal of Structural Stability and Dynamics, Vol. 8*, 2008: 547-568.

Kuribayashi, K., Tsuchiya, K., You, Z., Tomus, D., Umemoto, M., Ito, T. and Sasaki, M. "Self-deployable origami stent grafts as a biomedical application of Ni-rich TiNi shape memory alloy foil." *Materials Science and Engineering: A, Volume 419, Issue 1-2*, 2006: 131-137.

Lagoudas, D.C. *Shape memory alloys: modeling and engineering applications.* New York, USA: Springer, 2008.

Levenberg, K. "A method for the solution of certain nonlinear problems in least squares." *The Quarterly of Applied Mathematics, Volume 2*, 1944: 164-168.

Levine, D.S. *Introduction to neural and cognitive modeling.* London, UK: Lawrence Erlbaum Associates, 2000.

Li, Q., Yu, J., Mu, B. and Sun, X. "BP neural network prediction of the mechanical properties of porous NiTi shape memory alloy prepared by thermal explosion reaction." *Materials Science and Engineering: A, Volume 419, Issue 1-2*, 2006: 214-217.

Liang, C. and Rogers, C. A. "Design of shape memory alloy springs with applications in vibration control." *Journal of Vibration and Acoustics, Vol. 115*, 1993: 129-135.

Lien, J.P., York, A., Fang, T. and Buckner, G.D. "Modeling piezoelectric actuators with hysteretic recurrent neural networks." *Sensors and Actuators A; Physical, Volume 163, Issue 2*, 2010: 516-525.

Lisboa, P.J. and Taktak, A.F. "The use of artificial neural networks in decision support in cancer: A systematic review." *Neural Networks, Volume 19, Issue 4*, 2006: 408-415.

Luo, H. and Puthusserypady, S. "Spatia-temporal modeling and analysis of fMRI data using NARX neural network." *International Journal of Neural Systems, Volume 16, No. 2*, 2006: 139-149.

Majima, S., Kodama, K. and Hasegawa, T. "Modeling of shape memory alloy actuator and tracking control system with the model." *IEEE Transactions on Control Systems Technology, Vol. 954, No. 1*, 2001: 54-59.

Marquardt, D. "An algorithm for least-squares estimation of nonlinear parameters." *SIAM Journal on Applied Mathematics, Volume 11, Issue 2*, 1963: 431-441.

Martelli, A. "Seismic isolation and energy dissipation worldwide application and perspectives." *WIT Trans. on the Built Environment, Vol. 93*, 2007: 50-62.

Mayergoyz, I. "Mathematical models of hysteresis and their applications." *Elsevier*, 2003.

McCulloch, W.S. and Pitts, W. "A logical calculus of the ideas immanent in nervous activity." *Bulletin of Mathematical Biophysics, Vol. 5*, 1943: 115-133.

Meier, H., Oelschlaeger, L. "Numerical thermomechanical modelling of shape memory alloy wires." *Materials Science and Engineering A 378*, 2004: 484-489.

Minsky, M. and Papert, S. *Perceptrons.* Cambridge, MA: MIT Press, 1969.

Mirzaeifar, R., DesRoches, R. and Yavari, A. "A combined analytical, numerical, and experimental study of shape-memory-alloy helical springs." *International Jounral of Solids and Structures, Vol. 48,* 2011: 611-624.

Olunloyo, V. O. S., Oyediran, A. A., Adewale, A., Adelaja, A. O. and Osheko, C. A. "Concerning the transverse and longitudinal vibration of a fluid conveying beam and the pipe walking phenomenon." *The 26th International Conference on Offshore Mechanics and Artic Engineering.* San Diego, CA: OMAE, 2007. 285-298.

Owen, G. E. *Electromagnetic theory (Reprint of 1963 ed.).* Boston, MA: Allyn and Bacon, Inc., 2003.

Palomera, R. *Passive electromagnetic damping device for motion control of building structures.* PhD Thesis, Cambridge: MIT, 2005.

Patil, D. *Innovative applications of smart materials to vibration suppression and actuation for offshore engineering.* Master Thesis, Houston, TX: University of Houton, 2010.

Pineda, F. J. "Recurrent backpropagation and the dynamical approach to adaptive neural computation." *Neural Computation, Vol. 1*, 1989: 161-172.

Podrzaj, P., Regojevic, B. and Kariz, Z. "An enhanced mechanical sytem for studying the basics of control system dynamics." *IEEE Transactions on Education, Vol. 48, Issue 1*, 2005: 23-28.

Potapov, P.L., da Silva, E.P. "Actuator 2000." *7th International Conference on New Actuators.* Bremen: Germany, 2000. 156-162.

Puscasu, G., Codres, B., Stancu, A. and Murariu, G. "Nonlinear system identification based on internal recurrent neural networks." *International Journal of Neural Systems, Volume 19, No. 2,* 2009: 115-125.

Ramallo, J. C., Johnson, E. A., Spencer, B. F. and Sain, M. K. "Semiactive building base isolation." *American Control Conference.* San Diego, CA, USA, 1999. 515-519.

Rosenblatt, F. "The perceptron: a probabilistic model for information storage and organization in the brain." *Psychological Review, Vol. 65,* 1959: 386-408.

Rumelhart, D. E., Hinton, G. E. and Williams, R. J. "Learning internal representations by error propagation." In *Parallel Distribution Processing: Exploration in the Microstructure of Cognition, Vol. 1, Foundation,* by D. E., McClelland, J. L. and the PDP Research Groups (Eds.) Rumelhart. Cambridge: MIT Press/Bradford Books, 1986.

Schafer, A. M. and Zimmermann, H. G. "Recurrent neural networs are universal approximators." *International Journal of Neural Networks, Volume 17, No. 4,* 2007: 253-263.

Scruggs, J. "Active, regenerative control of civil structures." Master's Thesis, 1999.

Shariat, B. S., Liu, Y. and Rio, G. "Mathematical modelling of pseudoelastic behaviour of tapered NiTi bars." *Journal of Alloys and Compounds,* 2012: in pressed.

Shaw, J.A. "A thermomechanical model for a 1-D shape memory alloy wire with propagating instabilities." *International Journal of Solids and Structures 39,* 2002: 1275-1305.

Siegelmann, H.T., Horne, B.G. and Giles, C.L. "Computational capabilities of recurrent NARX neural networks." *IEEE Transactions On Systems, Man, and Cybernetics, B-27, Volume 2*, 1997: 208-215.

Siredey, N., Patoor, E., Berveiller, M., Eberhardt, A. "Constitutive equations for polycrystalline thermoelastic shape memory alloys, part I. intragranular interactions and behavior of the grain." *International Journal of Solids and Structures 36*, 1999: 4289-4315.

Skinner, R.I., Robinson, W.H. and McVerry, G.H. *An introduction to seismic isolation.* New York, USA: John Wiley & Sons, 1993.

Smith, R.C. "Smart material systems: model development." *SIAM Press.* Philadilphia, PA, 2005.

Song, G. "Intelligent Structure System." Lecture, Houston, 2008.

Soong, T.T. and Dargush, G.F. *Passive energy dissipation systems in structural engineering.* New York: John Wiley & Sons, 1997.

Tanaka, K., Kobayashi, S., Sato, Y. "Thermomechanics of transformation pseudoelasticity and shape memory effects in alloys." *International Journal of Plasticity 2*, 1986: 59-72.

Tedesco, J. W., McDougal, W. G. and Allen Ross, C. *Structural dynamics: theory and applications.* Menlo Park, CA: Addison-Wesley, 1999.

Thawornwong, S. and Enke, D. "The adaptive selection of financial and economic viariables for use with artificial neural networks." *Neurocomputing, Volume 56,* 2004: 205-232.

Thomson, P., Balas, G.J. and Leo, P.H. "Analysis of trigger line models for shape memory hysteresis based on dynamic testing." *Journal of Intelligent Material Systems and Structures, Vol. 8,* 1997: 193-201.

Tobushi, H. and Tanaka, K. "Deformation of a shape memory alloy helical spring (analysis based on stress-strain-temperature relation)." *Japan Society Mechanical Engineering International Journal, Series I, Vol. 34, No. 1,* 1991: 83-89.

Torra, V., Isalgue, A., Martorell, F., Terriault, P. and Lovey, F.C. "Built in dampers for family homes via SMA: an ANSYS computation scheme based on mesoscopic and microscopic experimental analyses." *Engineering Structures Volume 29, Issue 8,* 2007: 1889-1902.

Wang, H. and Song, G. "Fault detection and fault tolerant control of a smart base isolation system with magneto-rheological damper." *Smart Materials and Structures, Vol. 20,* 2011: 85015-85023.

Wang, H., Malki, H. A. and Song, G. "Fuzzy semi-active control of MR damper for structural base isolation." *IEEE International Conference on Fuzzy Systems.* Jeju Island, Korea: IEEE, 2009. 2035-2040.

Wilde, K., Gardoni, P. and Fujino, Y. "Base isolation system with shape memory alloy device for elevated highway bridges." *Engineering Structures, Vol. 22,* 2000: 222-229.

Williams, R. J., Zipser, D. "A learning algorithm for continually running fully recurrent neural networks." *Neural Computation, Vol. 1*, 1989: 270-280.

Woodson, H. H. and Melcher, J. R. *Electromachanical dynamics, part 1: discrete systems.* New York, NY: John Wiley & Sons, 1968.

Ye, H., Nicolai, R. and Reh, L. "A Bayesian-Gaussian neural network and its applications in process engineering." *Chemical Engineering and Processing: Process Intensification, Volume 37, Issue 5*, 1998: 439-449.

Yook, B. S. *VIV and fatigue life of (2) 8" 15 KSI well jumpers & (2) 10" 15 KSI flow line jumpers for BP-GOM project.* Finite Element Analysis - Final Report, Houston: Cameron, 2008.

Zhang, P., Song, G. and Li, H.N. "Pounding Tuned Mass Damper (PTMD): An Innovative Device to Control the Vibration of Subsea Jumpers." *ready to be published*, n.d.

Zhang, X., Tan, Y. and Su, M. "Modeling of hysteresis in piezoelectric actuators using neural networks." *Mechanical Systems and Signal Processing, Volume 23, Issue 8*, 2009: 2699-2711.

Zhu, S. and Zhang, Y. "A thermomechanical constitutive model for superelastic SMA wire with strain-rate dependence." *Smart Materials and Structures, Vol. 16,* 2007: 1696-1707.

# A. Appendix

## A.1State Space Model of Base-Isolated Structure

A_b =

1.0e+003 *

| | | | | | |
|---|---|---|---|---|---|
| 0 | 0 | 0 | 0.0010 | 0 | 0 |
| 0 | 0 | 0 | 0 | 0.0010 | 0 |
| 0 | 0 | 0 | 0 | 0 | 0.0010 |
| -1.2361 | 1.2361 | 0 | -0.0001 | 0.0001 | 0 |
| 1.1907 | -2.1596 | 0.9689 | 0.0001 | -0.0002 | 0.0001 |
| 0 | 0.6225 | -0.6225 | 0 | 0.0001 | -0.0001 |

B_b =

| | |
|---|---|
| 0 | 0 |
| 0 | 0 |
| 0 | 0 |
| -1.0000 | 0 |
| -1.0000 | 0 |
| -1.0000 | 0.5108 |

C_b =

1.0e+003 *

| | | | | | |
|---|---|---|---|---|---|
| 0.0010 | 0 | 0 | 0 | 0 | 0 |
| 0 | 0.0010 | 0 | 0 | 0 | 0 |
| 0 | 0 | 0.0010 | 0 | 0 | 0 |
| 0 | 0 | 0 | 0.0010 | 0 | 0 |
| 0 | 0 | 0 | 0 | 0.0010 | 0 |
| 0 | 0 | 0 | 0 | 0 | 0.0010 |
| -1.2361 | 1.2361 | 0 | -0.0001 | 0.0001 | 0 |
| 1.1907 | -2.1596 | 0.9689 | 0.0001 | -0.0002 | 0.0001 |
| 0 | 0.6225 | -0.6225 | 0 | 0.0001 | -0.0001 |

D_b =

| | |
|---|---|
| 0 | 0 |
| 0 | 0 |
| 0 | 0 |

0 0
0 0
0 0
0 0
0 0
0 0.5108

## A.2State Space Model of Subsea Jumper System

K =

1.0e+006 *

Columns 1 through 9

| | | | | | | | | |
|---|---|---|---|---|---|---|---|---|
| 6.3689 | -2.2680 | 0.3093 | -0.3098 | 0.0007 | -0.0008 | 0.0006 | 0.0058 | -0.0064 |
| -2.2680 | 1.4303 | -0.5837 | 0.1179 | 0.1495 | -0.0391 | 0.0098 | -0.0063 | 0.0042 |
| 0.3093 | -0.5837 | 0.5330 | -0.0670 | -0.1497 | 0.0394 | -0.0100 | 0.0348 | -0.0325 |
| -0.3098 | 0.1179 | -0.0670 | 0.3444 | -0.2885 | 0.1635 | -0.0417 | -0.0251 | 0.0348 |
| 0.0007 | 0.1495 | -0.1497 | -0.2885 | 0.6507 | -0.5440 | 0.2234 | -0.0417 | -0.0100 |
| -0.0008 | -0.0391 | 0.0394 | 0.1635 | -0.5440 | 0.7609 | -0.5440 | 0.1635 | 0.0394 |
| 0.0006 | 0.0098 | -0.0100 | -0.0417 | 0.2234 | -0.5440 | 0.6507 | -0.2885 | -0.1497 |
| 0.0058 | -0.0063 | 0.0348 | -0.0251 | -0.0417 | 0.1635 | -0.2885 | 0.3444 | -0.0670 |
| -0.0064 | 0.0042 | -0.0325 | 0.0348 | -0.0100 | 0.0394 | -0.1497 | -0.0670 | 0.5330 |
| 0.0028 | -0.0010 | 0.0042 | -0.0063 | 0.0098 | -0.0391 | 0.1495 | 0.1179 | -0.5837 |
| -0.0054 | 0.0028 | -0.0064 | 0.0058 | 0.0006 | -0.0008 | 0.0007 | -0.3098 | 0.3093 |

Columns 10 through 11

| | |
|---|---|
| 0.0028 | -0.0054 |
| -0.0010 | 0.0028 |
| 0.0042 | -0.0064 |
| -0.0063 | 0.0058 |
| 0.0098 | 0.0006 |
| -0.0391 | -0.0008 |
| 0.1495 | 0.0007 |
| 0.1179 | -0.3098 |
| -0.5837 | 0.3093 |
| 1.4303 | -2.2680 |
| -2.2680 | 6.3689 |

M =

Columns 1 through 9

| | | | | | | | | |
|---|---|---|---|---|---|---|---|---|
| 74.192 | 0 | 0 | 0 | 0 | 0 | 0 | 0 | 0 |
| 0 | 5.548 | 0 | 0 | 0 | 0 | 0 | 0 | 0 |
| 0 | 0 | 44.343 | 0 | 0 | 0 | 0 | 0 | 0 |
| 0 | 0 | 0 | 54.965 | 0 | 0 | 0 | 0 | 0 |
| 0 | 0 | 0 | 0 | 72.783 | 0 | 0 | 0 | 0 |
| 0 | 0 | 0 | 0 | 0 | 68.569 | 0 | 0 | 0 |

| | | | | | | | | |
|---|---|---|---|---|---|---|---|---|
| 0 | 0 | 0 | 0 | 0 | 0 | 72.782 | 0 | 0 |
| 0 | 0 | 0 | 0 | 0 | 0 | 0 | 54.965 | 0 |
| 0 | 0 | 0 | 0 | 0 | 0 | 0 | 0 | 44.343 |
| 0 | 0 | 0 | 0 | 0 | 0 | 0 | 0 | 0 |
| 0 | 0 | 0 | 0 | 0 | 0 | 0 | 0 | 0 |

Columns 10 through 11

| | |
|---|---|
| 0 | 0 |
| 0 | 0 |
| 0 | 0 |
| 0 | 0 |
| 0 | 0 |
| 0 | 0 |
| 0 | 0 |
| 0 | 0 |
| 0 | 0 |
| 5.548 | 0 |
| 0 | 74.192 |

Cd =

1.0e+003 *

Columns 1 through 9

| | | | | | | | | |
|---|---|---|---|---|---|---|---|---|
| 1.3140 | -0.4652 | 0.0635 | -0.0636 | 0.0001 | -0.0002 | 0.0001 | 0.0012 | -0.0013 |
| -0.4652 | 0.2940 | -0.1197 | 0.0242 | 0.0307 | -0.0080 | 0.0020 | -0.0013 | 0.0009 |
| 0.0635 | -0.1197 | 0.1138 | -0.0137 | -0.0307 | 0.0081 | -0.0021 | 0.0071 | -0.0067 |
| -0.0636 | 0.0242 | -0.0137 | 0.0762 | -0.0592 | 0.0335 | -0.0086 | -0.0052 | 0.0071 |
| 0.0001 | 0.0307 | -0.0307 | -0.0592 | 0.1408 | -0.1116 | 0.0458 | -0.0086 | -0.0021 |
| -0.0002 | -0.0080 | 0.0081 | 0.0335 | -0.1116 | 0.1630 | -0.1116 | 0.0335 | 0.0081 |
| 0.0001 | 0.0020 | -0.0021 | -0.0086 | 0.0458 | -0.1116 | 0.1408 | -0.0592 | -0.0307 |
| 0.0012 | -0.0013 | 0.0071 | -0.0052 | -0.0086 | 0.0335 | -0.0592 | 0.0762 | -0.0137 |
| -0.0013 | 0.0009 | -0.0067 | 0.0071 | -0.0021 | 0.0081 | -0.0307 | -0.0137 | 0.1138 |
| 0.0006 | -0.0002 | 0.0009 | -0.0013 | 0.0020 | -0.0080 | 0.0307 | 0.0242 | -0.1197 |
| -0.0011 | 0.0006 | -0.0013 | 0.0012 | 0.0001 | -0.0002 | 0.0001 | -0.0636 | 0.0635 |

Columns 10 through 11

| | |
|---|---|
| 0.0006 | -0.0011 |
| -0.0002 | 0.0006 |
| 0.0009 | -0.0013 |
| -0.0013 | 0.0012 |
| 0.0020 | 0.0001 |
| -0.0080 | -0.0002 |
| 0.0307 | 0.0001 |
| 0.0242 | -0.0636 |
| -0.1197 | 0.0635 |
| 0.2940 | -0.4652 |

-0.4652 1.3140

K_tmd =

1.0e+006 *

Columns 1 through 9

| | | | | | | | | |
|---|---|---|---|---|---|---|---|---|
| 6.3689 | -2.2680 | 0.3093 | -0.3098 | 0.0007 | -0.0008 | 0.0006 | 0.0058 | -0.0064 |
| -2.2680 | 1.4303 | -0.5837 | 0.1179 | 0.1495 | -0.0391 | 0.0098 | -0.0063 | 0.0042 |
| 0.3093 | -0.5837 | 0.5330 | -0.0670 | -0.1497 | 0.0394 | -0.0100 | 0.0348 | -0.0325 |
| -0.3098 | 0.1179 | -0.0670 | 0.3444 | -0.2885 | 0.1635 | -0.0417 | -0.0251 | 0.0348 |
| 0.0007 | 0.1495 | -0.1497 | -0.2885 | 0.6507 | -0.5440 | 0.2234 | -0.0417 | -0.0100 |
| -0.0008 | -0.0391 | 0.0394 | 0.1635 | -0.5440 | 0.7609 | -0.5440 | 0.1635 | 0.0394 |
| 0.0006 | 0.0098 | -0.0100 | -0.0417 | 0.2234 | -0.5440 | 0.6507 | -0.2885 | -0.1497 |
| 0.0058 | -0.0063 | 0.0348 | -0.0251 | -0.0417 | 0.1635 | -0.2885 | 0.3444 | -0.0670 |
| -0.0064 | 0.0042 | -0.0325 | 0.0348 | -0.0100 | 0.0394 | -0.1497 | -0.0670 | 0.5330 |
| 0.0028 | -0.0010 | 0.0042 | -0.0063 | 0.0098 | -0.0391 | 0.1495 | 0.1179 | -0.5837 |
| -0.0054 | 0.0028 | -0.0064 | 0.0058 | 0.0006 | -0.0008 | 0.0007 | -0.3098 | 0.3093 |
| 0 | 0 | 0 | 0 | 0 | 0 | 0 | 0 | 0 |

Columns 10 through 12

| | | |
|---|---|---|
| 0.0028 | -0.0054 | 0 |
| -0.0010 | 0.0028 | 0 |
| 0.0042 | -0.0064 | 0 |
| -0.0063 | 0.0058 | 0 |
| 0.0098 | 0.0006 | 0 |
| -0.0391 | -0.0008 | 0 |
| 0.1495 | 0.0007 | 0 |
| 0.1179 | -0.3098 | 0 |
| -0.5837 | 0.3093 | 0 |
| 1.4303 | -2.2680 | 0 |
| -2.2680 | 6.3689 | 0 |
| 0 | 0 | 0 |

M_tmd =

Columns 1 through 9

| | | | | | | | | |
|---|---|---|---|---|---|---|---|---|
| 74.192 | 0 | 0 | 0 | 0 | 0 | 0 | 0 | 0 |
| 0 | 5.548 | 0 | 0 | 0 | 0 | 0 | 0 | 0 |
| 0 | 0 | 44.343 | 0 | 0 | 0 | 0 | 0 | 0 |
| 0 | 0 | 0 | 54.965 | 0 | 0 | 0 | 0 | 0 |
| 0 | 0 | 0 | 0 | 72.783 | 0 | 0 | 0 | 0 |
| 0 | 0 | 0 | 0 | 0 | 68.569 | 0 | 0 | 0 |
| 0 | 0 | 0 | 0 | 0 | 0 | 72.782 | 0 | 0 |
| 0 | 0 | 0 | 0 | 0 | 0 | 0 | 54.965 | 0 |
| 0 | 0 | 0 | 0 | 0 | 0 | 0 | 0 | 44.343 |

```
0     0     0     0     0     0     0     0     0
0     0     0     0     0     0     0     0     0
0     0     0     0     0     0     0     0     0
```

```
  Columns 10 through 12
0     0     0
0     0     0
0     0     0
0     0     0
0     0     0
0     0     0
0     0     0
0     0     0
0     0     0
5.548 0     0
0     74.192 0
0     0     18.144
```

```
Cd_tmd =

  1.0e+003 *
  Columns 1 through 9
   1.3140  -0.4652   0.0635  -0.0636   0.0001  -0.0002   0.0001   0.0012  -0.0013
  -0.4652   0.2940  -0.1197   0.0242   0.0307  -0.0080   0.0020  -0.0013   0.0009
   0.0635  -0.1197   0.1138  -0.0137  -0.0307   0.0081  -0.0021   0.0071  -0.0067
  -0.0636   0.0242  -0.0137   0.0762  -0.0592   0.0335  -0.0086  -0.0052   0.0071
   0.0001   0.0307  -0.0307  -0.0592   0.1408  -0.1116   0.0458  -0.0086  -0.0021
  -0.0002  -0.0080   0.0081   0.0335  -0.1116   0.1630  -0.1116   0.0335   0.0081
   0.0001   0.0020  -0.0021  -0.0086   0.0458  -0.1116   0.1408  -0.0592  -0.0307
   0.0012  -0.0013   0.0071  -0.0052  -0.0086   0.0335  -0.0592   0.0762  -0.0137
  -0.0013   0.0009  -0.0067   0.0071  -0.0021   0.0081  -0.0307  -0.0137   0.1138
   0.0006  -0.0002   0.0009  -0.0013   0.0020  -0.0080   0.0307   0.0242  -0.1197
  -0.0011   0.0006  -0.0013   0.0012   0.0001  -0.0002   0.0001  -0.0636   0.0635
   0         0         0         0         0         0         0         0         0

  Columns 10 through 12
   0.0006  -0.0011         0
  -0.0002   0.0006         0
   0.0009  -0.0013         0
  -0.0013   0.0012         0
   0.0020   0.0001         0
  -0.0080  -0.0002         0
   0.0307   0.0001         0
   0.0242  -0.0636         0
  -0.1197   0.0635         0
```

```
 0.2940   -0.4652         0
-0.4652    1.3140         0
 0         0              0.0005
```

```
A = [zeros(n,n),eye(n);-inv(M_tmd)*K_tmd,-inv(M_tmd)*Cd_tmd];
B = [zeros(n,2);-1 0;-1 0;-1 0;-1 0;-1 0;-1 -0.0146;-1 0;-1 0;-1 0;-1 0;-1 0;-1 0.0551;];
C=[eye(2*n);-inv(M_tmd)*K_tmd,-inv(M_tmd)*Cd_tmd;K_tmd zeros(n,n)];
D=[zeros(4*n,2)];
```